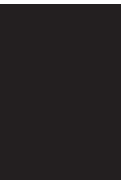


Mathematics in Biomedical Imaging

Guest Editors: Ming Jiang, Alfred K. Louis, Didier Wolf,
Hongkai Zhao, Christian Daul, Zhaotian Zhang, and Tie Zhou





Mathematics in Biomedical Imaging

International Journal of Biomedical Imaging

Mathematics in Biomedical Imaging

Guest Editors: Ming Jiang, Alfred K. Louis,
Didier Wolf, Hongkai Zhao, Christian Daul,
Zhaotian Zhang, and Tie Zhou



Copyright © 2007 Hindawi Publishing Corporation. All rights reserved.

This is a special issue published in volume 2007 of "International Journal of Biomedical Imaging." All articles are open access articles distributed under the Creative Commons Attribution License, which permits unrestricted use, distribution, and reproduction in any medium, provided the original work is properly cited.

Editor-in-Chief

Ge Wang, Virginia Polytechnic Institute and State University, USA

Associate Editors

Haim Azhari, Israel
Kyongtae Bae, USA
Richard Bayford, UK
F. Beekman, The Netherlands
Subhasis Chaudhuri, India
Jyh-Cheng Chen, Taiwan
Anne Clough, USA
Carl Crawford, USA
Min Gu, Australia
Eric Hoffman, USA
Jiang Hsieh, USA

Ming Jiang, China
Marc Kachelrie, Germany
Seung Wook Lee, South Korea
Alfred Karl Louis, Germany
E. Meijering, The Netherlands
Vasilis Ntziachristos, USA
Scott Pohlman, USA
Erik Ritman, USA
Jay Rubinstein, USA
Pete Santago, USA
Lizhi Sun, USA

Jie Tian, China
Michael Vannier, USA
Yue Wang, USA
Guowei Wei, USA
David L. Wilson, USA
Sun Guk Yu, South Korea
Habib Zaidi, Switzerland
Yantian Zhang, USA
Yibin Zheng, USA
Tiange Zhuang, China

Contents

Mathematics in Biomedical Imaging, Ming Jiang, Alfred K. Louis, Didier Wolf, Hongkai Zhao, Christian Daul, Zhaotian Zhang, and Tie Zhou
Volume 2007, Article ID 64954, 2 pages

The Formula of Grangeat for Tensor Fields of Arbitrary Order in n Dimensions, T. Schuster
Volume 2007, Article ID 12839, 4 pages

The Mathematical Foundations of 3D Compton Scatter Emission Imaging, T. T. Truong, M. K. Nguyen, and H. Zaidi
Volume 2007, Article ID 92780, 11 pages

Level Set Method for Positron Emission Tomography, Tony F. Chan, Hongwei Li, Marius Lysaker, and Xue-Cheng Tai
Volume 2007, Article ID 26950, 15 pages

Magnetic Field Distribution and Signal Decay in Functional MRI in Very High Fields (up to 9.4 T) Using Monte Carlo Diffusion Modeling, Bernd Michael Mueller-Bierl, Kamil Uludag, Philippe L. Pereira, and Fritz Schick
Volume 2007, Article ID 70309, 7 pages

Total Variation Regularization of Matrix-Valued Images, Oddvar Christiansen, Tin-Man Lee, Johan Lie, Usha Sinha, and Tony F. Chan
Volume 2007, Article ID 27432, 11 pages

Thalamus Segmentation from Diffusion Tensor Magnetic Resonance Imaging, Ye Duan, Xiaoling Li, and Yongjian Xi
Volume 2007, Article ID 90216, 5 pages

The Factorization Method for Electrical Impedance Tomography Data from a New Planar Device, Mustapha Azzouz, Martin Hanke, Chantal Oesterlein, and Karl Schilcher
Volume 2007, Article ID 83016, 7 pages

Model-Based Reconstructive Elasticity Imaging Using Ultrasound, Salavat R. Aglyamov, Andrei R. Skovoroda, Hua Xie, Kang Kim, Jonathan M. Rubin, Matthew O'Donnell, Thomas W. Wakefield, Daniel Myers, and Stanislav Y. Emelianov
Volume 2007, Article ID 35830, 11 pages

Editorial

Mathematics in Biomedical Imaging

**Ming Jiang,¹ Alfred K. Louis,² Didier Wolf,³ Hongkai Zhao,⁴ Christian Daul,³
Zhaotian Zhang,⁵ and Tie Zhou¹**

¹ School of Mathematical Sciences, Peking University, Beijing 100871, China

² Institute for Applied Mathematics, Saarland University, Postfach 151150, 66041 Saarbrücken, Germany

³ Institut National Polytechnique de Lorraine, Centre de Recherche en Automatique de Nancy, 54516 Vandoeuvre-Les-Nancy, France

⁴ Department of Mathematics, University of California Irvine, Irvine, CA 92697, USA

⁵ Division of Electronics & Information System, Department of Information Science, National Natural Science Foundation of China, Beijing 100085, China

Received 18 September 2007; Accepted 18 September 2007

Copyright © 2007 Ming Jiang et al. This is an open access article distributed under the Creative Commons Attribution License, which permits unrestricted use, distribution, and reproduction in any medium, provided the original work is properly cited.

Biomedical imaging is critically important for life science and health care. In this rapidly developing field, mathematics is one of the most powerful tools for developing image reconstruction as well as image processing theory and methods. Many of the innovations in biomedical imaging are fundamentally related to the mathematical sciences. With improvements of traditional imaging systems and emergence of novel imaging modalities such as molecular imaging towards molecular medicine, imaging equations that link measurements to original images become increasingly more complex to reflect the reality upto an ever-improving accuracy. Mathematics becomes increasingly useful and leads to a new array of interdisciplinary and challenging research opportunities. The future biomedical imaging will include advanced mathematical methods as major features.

It is a current trend that more mathematicians become engaged in biomedical imaging at all levels, from image reconstruction to image processing, and upto image understanding and various high-level applications. This special issue addresses the role of mathematics in biomedical imaging. The themes include theoretical analysis, algorithm design, system modeling and assessment, as well as various biomedical imaging applications. From 10 submissions, 7 papers are published in this special issue. Each paper was reviewed by at least two reviewers and revised according to review comments. The papers cover the following imaging modalities: X-ray computed tomography (CT), positron emission tomography (PET), magnetic resonance imaging (MRI), diffusion tensor imaging (DTI), electrical impedance tomography (EIT), and elasticity imaging using ultrasound.

The field of X-ray imaging has been expanding rapidly since Röntgen's historical discovery in 1895. X-ray CT, as

the first noninvasive tomographic method, has revolutionized imaging technologies in general, which was also the first successful application of mathematics in biomedical imaging. The mathematics is the theory of Radon transform invented by Radon in 1917. Further research may rejuvenate this classic topic to meet modern imaging challenges such as scattering effects. In Truong et al.'s paper, the authors presented two further generalizations of the Radon transform, namely, two classes of conical Radon transforms which originate from imaging processes using Compton scattered radiation. The first class, called C1-conical Radon transform, is related to an imaging principle with a collimated gamma camera whereas the second class, called C2-conical Radon transform, contains a special subclass which models the Compton camera imaging process. They demonstrated that the inversion of C2-conical Radon transform can be achieved under a special condition.

PET is currently a major imaging modality for clinical diagnostics and pharmacological research. The expectation maximization (EM) algorithm has been used in PET for years. In Chan et al.'s paper, the authors propose to combine the level set method with the EM algorithm for PET. The level set method, which was originally developed for capturing moving interfaces in multiphase physics, is used here to capture geometric information, for example, the anatomical structure. If another type of information is available, for example, CT or MRI images, it can be used as prior knowledge and can be incorporated into the formulation. The idea of combining geometric information with statistic methods is quite interesting and promising.

In Mueller-Bierl et al.'s paper, the authors investigated the magnetic field distribution and signal decay of high field

strength functional MRI imaging. The static dipole model has been extended to a dynamic model to describe the sampling of phases of the individual protons moving in the inhomogeneous magnetic field. The dynamic Brownian motion process is implemented using a Monte Carlo method with different step parameters. Various factors for signal decay and artifacts formation are investigated. Results from different methods were compared.

Earlier work on total variation (TV) regularization for color (vector valued) images is naturally extended to DTI, which is composed of a symmetric positive definite (SPD) matrix at each pixel. In the last decade, a new magnetic resonance modality, DTI, has caught a lot of interest. DTI can reveal anatomical structure information. In this special issue, there are two papers on this imaging technique. In Christiansen et al.'s paper, this type of tensor-valued images is denoised using TV regularization. Recently, partial differential equation- (PDE-) based image processing methods have been very successful in many applications due to its intrinsic geometric nature. TV regularization, which can effectively remove noise while keeping sharp features, is one of the most important techniques for PDE-based image processing methods. Although TV regularization is very natural for scalar (gray) images, there is no easy and natural way to extend to vector values (color) images. This paper proposes to use TV regularization to denoise DTI based on previous work on generalizing TV to vector value images. To maintain the SPD structure of the tensor, the authors propose to work on the LU factorization of the tensor rather than on the tensor itself. The results demonstrated the expected strength of TV regularization. Another paper on DTI is by Duan. The author proposes a semi-automatic thalamus and thalamus nuclei segmentation algorithm based on the mean-shift algorithm. The main advantages of the proposed method over methods based on K-means are its flexibility and adaptivity, since assumptions of Gaussian or a fixed number of clusters are not needed.

The EIT and elasticity imaging in the following two contributions are inverse problems of partial differential equations. In EIT, electric currents are applied to the boundary of an object and the induced surface voltages are measured. The measured voltage data are then used to reconstruct the internal conductivity distribution of the object. In Azzouz et al.'s paper, the authors establish two reconstruction methods for a new planar electrical impedance tomography device. This prototype allows noninvasive medical imaging techniques if only one side of a patient is accessible for electric measurements. The two reconstruction methods have different properties: one is a linearization-type method that allows quantitative reconstructions; and the other one, that is, the factorization method, is a qualitative one, and it is designed to detect anomalies within the body. Numerical results are also presented. In elasticity imaging, tissue motion in response to mechanical excitation is measured using modern imaging systems, and the estimated displacements are then used to reconstruct the spatial distribution of Young's modulus. In Aglyamov et al.'s paper, the authors propose a novel reconstruction technique for elastic properties of biological tissues from compressional ultrasound elastography. The

technique assumes spherical or cylindrical symmetry so that strain equations can be simplified. The reconstruction is conducted with inverse problem computations for partial differential equations. The proposed method is applied to image liver hemangioma (spherical symmetry) and rat DVT (cylindrical symmetry). The reconstruction results are compared with traditional elastography images. This paper offers some interesting thoughts especially for some special clinical cases where elasticity properties are spherical symmetric.

These papers represent an exciting, insightful observation into the state of the art, as well as emerging future topics in this important interdisciplinary field. We hope that this special issue would attract a major attention of the peers.

ACKNOWLEDGMENTS

We would like to express our appreciation to all the authors, reviewers, and the Editor-in-Chief Dr. Ge Wang for great support that to make this special issue possible.

*Ming Jiang
Alfred K. Louis
Didier Wolf
Hongkai Zhao
Christian Daul
Zhaotian Zhang
Tie Zhou*

Research Article

The Formula of Grangeat for Tensor Fields of Arbitrary Order in n Dimensions

T. Schuster

Department of Mechanical Engineering, Helmut Schmidt University, P.O. Box 700822, 22008 Hamburg, Germany

Received 18 October 2006; Revised 7 February 2007; Accepted 7 February 2007

Recommended by Alfred Karl Louis

The cone beam transform of a tensor field of order m in $n \geq 2$ dimensions is considered. We prove that the image of a tensor field under this transform is related to a derivative of the n -dimensional Radon transform applied to a projection of the tensor field. Actually the relation we show reduces for $m = 0$ and $n = 3$ to the well-known formula of Grangeat. In that sense, the paper contains a generalization of Grangeat's formula to arbitrary tensor fields in any dimension. We further briefly explain the importance of that formula for the problem of tensor field tomography. Unfortunately, for $m > 0$, an inversion method cannot be derived immediately. Thus, we point out the possibility to calculate reconstruction kernels for the cone beam transform using Grangeat's formula.

Copyright © 2007 T. Schuster. This is an open access article distributed under the Creative Commons Attribution License, which permits unrestricted use, distribution, and reproduction in any medium, provided the original work is properly cited.

1. INTRODUCTION

The cone beam transform for a symmetric covariant tensor field \mathbf{f} of order m reads as

$$\mathbf{Df}(a, \omega) = \int_0^\infty \langle \mathbf{f}(a + t\omega), \omega^m \rangle dt, \quad (1)$$

where a is the source of an X-ray, $\omega \in S^{n-1}$ is a direction, and ω^m denotes the m -fold tensor product $\omega^m = \omega \otimes \dots \otimes \omega$. If $m = 0$, this is the classical X-ray transform of functions which represents the mathematical model for the cone beam geometry in computerized tomography. For $m = 1$, the operator \mathbf{D} is the longitudinal X-ray transform of vector fields. A lot of numerical algorithms have been developed in recent years to solve the inverse problem $\mathbf{Df} = g$ in case $m = 0$ and $m = 1$; see, for example, Louis [1], Katsevich [2], Schuster [3], Derevtsov and Kashina [4], Sparr et al. [5] among others. But also for tensor fields of order $m > 1$, this transform is of interest in various applications such as photoelasticity and plasma physics. Solution approaches for the tensor tomography problem are found in Derevtsov [6], and Kazantsev and Bukhgeim [7]. A further important transform in computer-

ized tomography is given by the Radon transform

$$\mathbf{Rf}(s, \omega) = \int_{\omega^\perp} f(s\omega + y) dy, \quad s \in \mathbb{R}, \quad (2)$$

which maps a scalar function to its integrals over hyperplanes.

An important connection between \mathbf{D} and \mathbf{R} is given by the formula of Grangeat:

$$\frac{\partial}{\partial s} \mathbf{Rf}(\omega, s = \langle a, \omega \rangle) = - \int_{S^2} \mathbf{Df}(a, \theta) \delta'(\langle \theta, \omega \rangle) d\theta, \quad (3)$$

which is valid for differentiable scalar fields f with compact support; see Grangeat [8]. In this paper, we prove a generalization of Grangeat's formula to arbitrary tensor fields. More explicitly, we show that

$$\begin{aligned} \frac{\partial^{(n-2)}}{\partial s^{(n-2)}} \mathbf{Rf}_a(\omega, s = \langle a, \omega \rangle) \\ = (-1)^{(n-2)} \int_{S^{n-1}} \mathbf{Df}(a, \theta) \delta^{(n-2)}(\langle \theta, \omega \rangle) d\theta, \end{aligned} \quad (4)$$

where δ is Dirac's delta distribution and f_a are projections of the tensor field \mathbf{f} .

In Section 2, we prove that \mathbf{D} is a bounded linear mapping between suitable L^2 -spaces and give a representation for

its adjoint \mathbf{D}^* . In Section 3, we prove formula (4) using a duality argument for \mathbf{D} and \mathbf{R} . We finish this paper by pointing out the importance of this result for research in the area of tensor field tomography.

2. THE CONE BEAM TRANSFORM OF TENSOR FIELDS

We consider the Euclidean space \mathbb{R}^n . A covariant tensor of order m in \mathbb{R}^n is given by

$$\mathbf{f} = f_{i_1 \dots i_m} dx^{i_1} \otimes \dots \otimes dx^{i_m}, \quad x \in \mathbb{R}^n, \quad (5)$$

where $f_{i_1 \dots i_m} \in \mathbb{R}$, $1 \leq i_j \leq n$ for $j = 1, \dots, m$ and dx^i , $i = 1, \dots, n$, is the basis of covectors in $(\mathbb{R}^n)^*$,

$$dx^i(v) = v_i, \quad i = 1, \dots, n, \quad v \in \mathbb{R}^n. \quad (6)$$

As in (5), we use Einstein's summation convention throughout the paper, that means we sum up over equal indices. A tensor (5) of order m is symmetric if

$$f_{i_{\sigma(1)} \dots i_{\sigma(m)}} = f_{i_1 \dots i_m}, \quad (7)$$

where σ runs over all $m!$ permutations of $\{1, \dots, m\}$. The set of all symmetric tensors of order m is denoted by \mathcal{S}^m . A scalar product on \mathcal{S}^m is given by

$$\langle \mathbf{f}, \mathbf{g} \rangle = f_{i_1 \dots i_m} g^{i_1 \dots i_m}, \quad \mathbf{f}, \mathbf{g} \in \mathcal{S}^m, \quad (8)$$

where $g^{i_1 \dots i_m}$ are the contravariant components of the tensor \mathbf{g} . We write $\|\mathbf{f}\| = \sqrt{\langle \mathbf{f}, \mathbf{f} \rangle}$ for the norm on \mathcal{S}^m . If $m = 1$, this is the Euclidean norm. A symmetric covariant tensor field of order m in \mathbb{R}^n maps a point $x \in \mathbb{R}^n$ to an element of \mathcal{S}^m ,

$$x \mapsto \mathbf{f}(x) = f_{i_1 \dots i_m}(x) dx^{i_1} \otimes \dots \otimes dx^{i_m}, \quad x \in \mathbb{R}^n, \quad (9)$$

where $f_{i_1 \dots i_m}(x) \in \mathcal{S}^m$ for fixed x .

Let further $\Omega^n = \{x \in \mathbb{R}^n : |x| < 1\}$ be the open unit ball in \mathbb{R}^n . We introduce an inner product for tensor fields defined on Ω^n by

$$\langle \mathbf{f}, \mathbf{g} \rangle_{L^2} = \int_{\Omega^n} \langle \mathbf{f}(x), \mathbf{g}(x) \rangle dx = \int_{\Omega^n} f_{i_1 \dots i_m}(x) g^{i_1 \dots i_m}(x) dx, \quad (10)$$

which turns $L^2(\Omega^n, \mathcal{S}^m) := \{\mathbf{f} \in \mathcal{S}^m : \|\mathbf{f}\|_{L^2} = \langle \mathbf{f}, \mathbf{f} \rangle_{L^2}^{1/2} < \infty\}$ to a Hilbert space. Assume that $\Gamma \subset (\mathbb{R}^n \setminus \overline{\Omega^n})$ is the path representing the curve of sources of the X-ray beams. Examples for Γ which are used in practice are a circle, two perpendicular circles, or a helix. The cone beam transform of a symmetric tensor field \mathbf{f} of order m is then defined by

$$\begin{aligned} \mathbf{D}\mathbf{f}(a, \omega) &= \int_0^\infty \langle \mathbf{f}(a + t\omega), \omega^m \rangle dt \\ &= \int_0^\infty f_{i_1 \dots i_m}(a + t\omega) \omega^{i_1} \dots \omega^{i_m} dt, \end{aligned} \quad (11)$$

where $\omega \in S^{n-1} = \partial\Omega^n$ is the direction and $a \in \Gamma$ the source of the beam and $\omega^m = \omega \otimes \dots \otimes \omega$ means the m -fold tensor product of ω . As an arrangement, we extend $\mathbf{f}(x) = 0$ in $\mathbb{R}^n \setminus \overline{\Omega^n}$. Hence, integrals like (11) are well defined. Finally, we denote $\mathbf{D}_a \mathbf{f}(\omega) := \mathbf{D}\mathbf{f}(a, \omega)$. We note that \mathbf{D} coincides with the *longitudinal ray transform* in the book of Sharafutdinov [9]. The operators \mathbf{D} and \mathbf{D}_a are linear and bounded between L^2 -spaces.

Theorem 1. *Let $a \in \Gamma$. The mappings $\mathbf{D}_a : L^2(\Omega^n, \mathcal{S}^m) \rightarrow L^2(S^{n-1})$ and $\mathbf{D} : L^2(\Omega^n, \mathcal{S}^m) \rightarrow L^2(\Gamma \times S^{n-1})$ are linear and bounded if*

$$\int_\Gamma (|a| - 1)^{1-n} da < \infty. \quad (12)$$

Proof. For $\mathbf{f} \in L^2(\Omega^n, \mathcal{S}^m)$ and $a \in \Gamma$, we have

$$\begin{aligned} \int_{S^{n-1}} |\mathbf{D}_a \mathbf{f}(\omega)|^2 d\omega &= \int_{S^{n-1}} \left| \int_0^\infty \langle \mathbf{f}(a + t\omega), \omega^m \rangle dt \right|^2 d\omega \\ &\leq 2 \int_{S^{n-1}} \int_0^\infty \|\mathbf{f}(a + t\omega)\|^2 dt d\omega \\ &= 2 \int_{\Omega^n} \|\mathbf{f}(x)\|^2 |x - a|^{1-n} dx \\ &\leq 2(|a| - 1)^{1-n} \|\mathbf{f}\|_{L^2}^2, \end{aligned} \quad (13)$$

where we used the substitution $x = a + t\omega$ and the fact that $\mathbf{f}(x) = 0$ in $\mathbb{R}^n \setminus \overline{\Omega^n}$. This shows the continuity of \mathbf{D}_a . The continuity of \mathbf{D} follows then by using $\mathbf{D}\mathbf{f}(a, \omega) = \mathbf{D}_a \mathbf{f}(\omega)$ and

$$\int_\Gamma \int_{S^{n-1}} |\mathbf{D}\mathbf{f}(a, \omega)|^2 d\omega da \leq 2 \|\mathbf{f}\|_{L^2}^2 \int_\Gamma (|a| - 1)^{1-n} da. \quad (14)$$

Theorem 1 implies that \mathbf{D}_a and \mathbf{D} have bounded adjoints \mathbf{D}_a^* and \mathbf{D}^* .

Lemma 1. *The adjoints $\mathbf{D}_a^* : L^2(S^{n-1}) \rightarrow L^2(\Omega^n, \mathcal{S}^m)$ and $\mathbf{D}^* : L^2(\Gamma \times S^{n-1}) \rightarrow L^2(\Omega^n, \mathcal{S}^m)$ have the following representations:*

$$\mathbf{D}_a^* g(x) = |x - a|^{1-n-m} g\left(\frac{x - a}{|x - a|}\right) (x - a)^m, \quad (15)$$

$$\mathbf{D}^* g(x) = \int_\Gamma \left\{ |x - a|^{1-n-m} g\left(\frac{x - a}{|x - a|}\right) (x - a)^m \right\} da. \quad (16)$$

In (15), (16), the power m again is to be understood as the m -fold tensor product

$$(x - a)^m = (x - a) \otimes \dots \otimes (x - a). \quad (17)$$

Proof. Let $\mathbf{f} \in L^2(\Omega^n, \mathcal{S}^m)$, $g \in L^2(S^{n-1})$. Then

$$\begin{aligned} &\int_{S^{n-1}} \mathbf{D}_a \mathbf{f}(\omega) g(\omega) d\omega \\ &= \int_{S^{n-1}} \int_0^\infty f_{i_1 \dots i_m}(a + t\omega) \omega^{i_1} \dots \omega^{i_m} g(\omega) dt d\omega \\ &= \int_{\Omega^n} |x - a|^{1-n} f_{i_1 \dots i_m}(x) \frac{(x - a)^{i_1} \dots (x - a)^{i_m}}{|x - a|^m} \\ &\quad \times g\left(\frac{x - a}{|x - a|}\right) dx \\ &= \langle \mathbf{f}, \mathbf{D}_a^* g \rangle_{L^2}. \end{aligned} \quad (18)$$

Here, again we substituted $x = a + t\omega$. This shows the representation of \mathbf{D}_a^* . Equation (16) follows easily from (15) by an integration over Γ . \square

For $m = 0$, $n = 3$, \mathbf{D}^* is the backprojection operator in classical 3D cone beam tomography. If $m = 1$, $n = 3$, we obtain the adjoint of the cone beam transform in vector field tomography

$$\mathbf{D}^*g(x) = \int_{\Gamma} |x - a|^{-3} g\left(a, \frac{x - a}{|x - a|}\right) (x - a) da. \quad (19)$$

Remark 1. Note that the integrals (12) and (16) are well defined since Γ has a positive distance from $\overline{\Omega^n}$.

To prove formula (4), we will also need the adjoint of the Radon transform. The following lemma summarizes basic results of the Radon transform (2) which can be found, for example, in the book of Natterer [10].

Lemma 2. *The transforms $\mathbf{R} : L^2(\Omega^n) \rightarrow L^2([-1, 1] \times S^{n-1})$ and $\mathbf{R}_\omega : L^2(\Omega^n) \rightarrow L^2([-1, 1])$ where $\mathbf{R}_\omega f(s) = \mathbf{R}f(s, \omega)$ are linear and continuous with bounded adjoints $\mathbf{R}^* : L^2([-1, 1] \times S^{n-1}) \rightarrow L^2(\Omega^n)$ and $\mathbf{R}_\omega^* : L^2([-1, 1]) \rightarrow L^2(\Omega^n)$ represented by*

$$\begin{aligned} \mathbf{R}_\omega^*g(x) &= g(\langle x, \omega \rangle), \\ \mathbf{R}^*g(x) &= \int_{S^{n-1}} g(\langle x, \omega \rangle, \omega) d\omega. \end{aligned} \quad (20)$$

3. A CONNECTION BETWEEN RADON AND CONE BEAM TRANSFORM

The proof of (4) essentially relies on the duality of the pairs $(\mathbf{R}_\omega, \mathbf{R}_\omega^*)$, $(\mathbf{D}_a, \mathbf{D}_a^*)$ on the one side and the fact that $\delta^{(k)}$, where δ denotes Dirac's delta distribution, is homogeneous of degree $-k - 1$ on the other side. To see the latter property, we take $\phi \in \mathcal{C}_0^\infty(\mathbb{R})$, $\lambda > 0$ and compute

$$\begin{aligned} &\int_{\mathbb{R}} \phi(s) \delta^{(k)}(\lambda s) ds \\ &= \lambda^{-1} \int_{\mathbb{R}} \phi(\lambda^{-1}s) \delta^{(k)}(s) ds \\ &= \lambda^{-1} (-1)^k \frac{\partial^k}{\partial s^k} \{\phi(\lambda^{-1}s)\}_{|s=0} = \lambda^{-k-1} (-1)^k \phi^{(k)}(0) \\ &= \int_{\mathbb{R}} \phi(s) \lambda^{-k-1} \delta^{(k)}(s) ds. \end{aligned} \quad (21)$$

For a tensor field $\mathbf{f} \in L^2(\Omega^n, \mathcal{F}^m)$ and $a \in \Gamma$, we furthermore define

$$\begin{aligned} f_a(x) &= \langle \mathbf{f}(x), |x - a|^{-m} (x - a)^m \rangle \\ &= f_{i_1 \dots i_m}(x) |x - a|^{-m} (x - a)^{i_1} \dots (x - a)^{i_m}, \end{aligned} \quad (22)$$

$1 \leq i_j \leq n, j = 1, \dots, m.$

Using the Cauchy-Schwartz inequality, we easily get

$$\int_{\Omega^n} |f_a(x)|^2 dx \leq \int_{\Omega^n} \|\mathbf{f}(x)\|^2 dx. \quad (23)$$

Thus, $f_a \in L^2(\Omega^n)$, when $\mathbf{f} \in L^2(\Omega^n, \mathcal{F}^m)$.

We are now able to state the main result of this paper.

Theorem 2. *Let $n \geq 2$ and $\mathbf{f} \in \mathcal{C}_0^{(n-2)}(\Omega^n, \mathcal{F}^m)$. Then*

$$\begin{aligned} &\frac{\partial^{(n-2)}}{\partial s^{(n-2)}} \mathbf{R}f_a(\omega, s = \langle a, \omega \rangle) \\ &= (-1)^{(n-2)} \int_{S^{n-1}} \mathbf{D}\mathbf{f}(a, \theta) \delta^{(n-2)}(\langle \omega, \theta \rangle) d\theta, \end{aligned} \quad (24)$$

where $a \in \Gamma$, $\omega \in S^{n-1}$.

Proof. We follow the proof of Grangeat's classical formula as outlined in Natterer and Wübbeling [11, Section 2.3]. For $\psi \in L^2([-1, +1])$, we have from lemma 2 that

$$\begin{aligned} &\int_{-1}^{+1} \mathbf{R}_\omega f_a(s) \psi(s) ds \\ &= \int_{\Omega^n} f_a(x) \psi(\langle x, \omega \rangle) dx \\ &= \int_{\Omega^n} \langle \mathbf{f}(x), |x - a|^{-m} (x - a)^m \rangle \psi(\langle x, \omega \rangle) dx. \end{aligned} \quad (25)$$

Using (15), we obtain in the same way for $h \in L^2(S^{n-1})$,

$$\begin{aligned} &\int_{S^{n-1}} \mathbf{D}_a \mathbf{f}(\theta) h(\theta) d\theta \\ &= \int_{\Omega^n} \langle \mathbf{f}(x), |x - a|^{1-n-m} (x - a)^m \rangle h\left(\frac{x - a}{|x - a|}\right) dx. \end{aligned} \quad (26)$$

Assertion (24) is then proved when setting $h(\theta) = \delta^{(n-2)}(\langle \theta, \omega \rangle)$, $\psi(s) = \delta^{(n-2)}(s - \langle a, \omega \rangle)$ and taking into account that $\delta^{(n-2)}$ is homogeneous of degree $1 - n$. \square

Remark 2. Obviously, $\delta^{(n-2)}$ is not in $L^2([-1, +1])$. But since $\delta^{(n-2)} \in (\mathcal{C}^{(n-2)}([-1, +1]))'$ and the cone beam transform $\mathbf{D}\mathbf{f}(a, y)$ can be extended homogeneously to \mathbb{R}^n with respect to the second variable for any m according to $m = 1$ (see [11, Section 2.3]), the integrals in the proof of Theorem 2 are well defined by the smoothness requirement for \mathbf{f} . The expression on the right-hand side of (24) is to be understood as

$$\begin{aligned} &(-1)^{(n-2)} \int_{S^{n-1}} \mathbf{D}\mathbf{f}(a, \theta) \delta^{(n-2)}(\langle \omega, \theta \rangle) d\theta \\ &= \int_{S^{n-1} \cap \omega^\perp} \langle d^{(n-2)} \mathbf{D}\mathbf{f}(a, y = \theta), \omega^{(n-2)} \rangle d\theta, \end{aligned} \quad (27)$$

where $d^m = d \otimes \dots \otimes d$ means the m -fold inner derivative with respect to the second variable in $\mathbf{D}\mathbf{f}(a, y)$. We have that $d^1 = \nabla$ is the gradient, d^2 is the Hessian.

If $n = 3$, $m = 0$, (24) is just the classical formula of Grangeat (3). For $m = 1$, we get an extension of Grangeat's formula to vector fields, where

$$f_a(x) = \langle \mathbf{f}(x), |x - a|^{-1} (x - a) \rangle. \quad (28)$$

The benefits of formula (24) can barely be anticipated. Let us consider the scalar case, that is, $m = 0$. If there exists to each $s \in [-1, 1]$ a source point $a \in \Gamma$ such that $\langle a, \omega \rangle = s$, then the derivative $\frac{\partial^{(n-2)}}{\partial s^{(n-2)}} \mathbf{R}f(\omega, s)$ can be obtained for arbitrary $\omega \in S^{n-1}$, $s \in [-1, 1]$ by integrating a corresponding

derivative of the data $\mathbf{Df}(a, \theta)$ over the manifold $S^{n-1} \cap \omega^\perp$. This condition is well known as *Tuy's condition* (see, e.g., [10, Section VI.5]) and means that every hyperplane passing through Ω^n has to intersect the source curve Γ in at least one point. The situation changes decisively for $m > 0$ since the projections f_a depend on the source point a . Even if we found to every s a source a satisfying $\langle a, \omega \rangle = s$, this would not help since the object function f_a of \mathbf{R} changes with a . Thus applying formula (24) would give us $\mathbf{R}f_a(\omega, s)$ for a *single* s , namely, $s = \langle a, \omega \rangle$. Tuy's condition is not sufficient for $m > 0$. Moreover, we have to take into account that there is a nontrivial null space for $m > 0$ anyway. To see this, we note that $\mathbf{Df} = 0$ if \mathbf{f} is a *potential field*, that means $\mathbf{f} = d\mathbf{p}$ for $\mathbf{p} \in H_0^1(\Omega^n, \mathcal{G}^{m-1})$. We refer to the book of Sharafutdinov [9] for a characterization of the null space of \mathbf{D} . Denisjuk [12] suggested a generalization of Tuy's condition for higher order tensor fields. He obtained similar formulas as (24) and showed that every plane through Ω^n has to intersect Γ at least $m - 1$ times.

If it is possible to compute f_a with the help of formula (24), the curve Γ additionally has to satisfy the requirement that $\mathbf{f}(x)$ can be computed from the projections

$$\langle \mathbf{f}(x), |x - a|^{-m}(x - a)^m \rangle. \quad (29)$$

This is possible, if the curve Γ fulfills the condition, that for each $x \in \Omega^n$ there exist $\dim(\mathcal{G}^m) = n^m$ source points a_1, \dots, a_{n^m} such that the tensors $|x - a_i|^{-m}(x - a_i)^m$ are linearly independent for fixed x and $1 \leq i \leq n^m$. The tensor field $\mathbf{f}(x)$ can then be recovered from the projections (29). In case of three-dimensional vector fields ($n = 3, m = 1$), we need three linearly independent vectors $x - a_i$ to each x . Hence, this condition is not fulfilled when, for example, $\Gamma = \{a \in \mathbb{R}^3 : |a - a_0| = r, a_3 = 0\}$ is a single circle since we find no such vectors for x in $\{|x - a_0| < 1, x_3 = 0\}$.

Formula (24) could be used to calculate reconstruction kernels for \mathbf{D} , that is we could try to solve

$$\mathbf{D}^* \gamma_{i_1 \dots i_m}^\gamma(x) = \mathbf{E}_{i_1 \dots i_m}^\gamma(x, \cdot) \quad (30)$$

using that relation to the Radon transform, where $\mathbf{E}_{i_1 \dots i_m}^\gamma(x, y) \approx \delta(x - y) dx^{i_1} \otimes \dots \otimes dx^{i_m}$ for small $\gamma > 0$ is an approximation to the delta distribution. Reconstruction kernels are necessary to cope the problem of tensor tomography with the *method of approximate inverse*; see, for example, Louis [13], Schuster [3], Rieder and Schuster [14]. It is clear that

$$\begin{aligned} \mathbf{Df}(a, \omega) \omega + \alpha_1(a, \omega, \omega_1) \omega_1 + \alpha_2(a, \omega, \omega_2) \omega_2 \\ = \int_0^\infty \mathbf{f}(a + t\omega) dt \end{aligned} \quad (31)$$

for certain coefficients α_1, α_2 , where $\{\omega, \omega_1, \omega_2\}$ forms an orthonormal basis of \mathbb{R}^3 . Unfortunately, α_1, α_2 , are unknown. An idea to apply the method of approximate inverse to \mathbf{D} might be to approximate

$$\mathbf{Df}(a, \omega) \omega \approx \int_0^\infty \mathbf{f}(a + t\omega) dt, \quad (32)$$

and to use methods for 3D cone beam CT to solve the problem. If $\nu^\gamma(x)$ denotes a reconstruction kernel for \mathbf{D} in case

$m = 0$, then $\nu_i^\gamma(x) := \nu^\gamma(x) \cdot e_i$ represents a reconstruction kernel for the right-hand side of (32). This approach is subject of current research. Hence, relation (24) might be of large interest in the area of tensor tomography problems.

ACKNOWLEDGMENT

The author is supported by the Deutsche Forschungsgemeinschaft (DFG) under Schu 1978/1-5.

REFERENCES

- [1] A. K. Louis, "Filter design in three-dimensional cone beam tomography: circular scanning geometry," *Inverse Problems*, vol. 19, no. 6, pp. S31–S40, 2003.
- [2] A. Katsevich, "Theoretically exact filtered backprojection-type inversion algorithm for spiral CT," *SIAM Journal on Applied Mathematics*, vol. 62, no. 6, pp. 2012–2026, 2002.
- [3] T. Schuster, "An efficient mollifier method for three-dimensional vector tomography: convergence analysis and implementation," *Inverse Problems*, vol. 17, no. 4, pp. 739–766, 2001.
- [4] E. Yu. Derevtsov and I. G. Kashina, "Numerical solution to the vector tomography problem by tools of a polynomial basis," *Siberian Journal of Numerical Mathematics*, vol. 5, no. 3, pp. 233–254, 2002 (Russian).
- [5] G. Sparr, K. Stråhlén, K. Lindström, and H. W. Persson, "Doppler tomography for vector fields," *Inverse Problems*, vol. 11, no. 5, pp. 1051–1061, 1995.
- [6] E. Yu. Derevtsov, "An approach to direct reconstruction of a solenoidal part in vector and tensor tomography problems," *Journal of Inverse and Ill-Posed Problems*, vol. 13, no. 3, pp. 213–246, 2005.
- [7] S. G. Kazantsev and A. A. Bukhgeim, "Singular value decomposition for the 2D fan-beam Radon transform of tensor fields," *Journal of Inverse and Ill-Posed Problems*, vol. 12, no. 3, pp. 245–278, 2004.
- [8] P. Grangeat, "Mathematical framework of cone beam 3D reconstruction via the first derivative of the Radon transform," in *Mathematical Methods in Tomography*, G. T. Herman, A. K. Louis, and F. Natterer, Eds., vol. 1497 of *Lecture Notes in Math.*, pp. 66–97, Springer, Berlin, Germany, 1991.
- [9] V. A. Sharafutdinov, *Integral Geometry of Tensor Fields*, VSP, Utrecht, The Netherlands, 1994.
- [10] F. Natterer, *The Mathematics of Computerized Tomography*, John Wiley & Sons, Chichester, NH, USA, 1986.
- [11] F. Natterer and F. Wübbeling, *Mathematical Methods in Image Reconstruction*, SIAM, Philadelphia, Pa, USA, 2001.
- [12] A. Denisjuk, "Inversion of the X-ray transform for 3D symmetric tensor fields with sources on a curve," *Inverse Problems*, vol. 22, no. 2, pp. 399–411, 2006.
- [13] A. K. Louis, "Approximate inverse for linear and some non-linear problems," *Inverse Problems*, vol. 12, no. 2, pp. 175–190, 1996.
- [14] A. Rieder and T. Schuster, "The approximate inverse in action III: 3D-Doppler tomography," *Numerische Mathematik*, vol. 97, no. 2, pp. 353–378, 2004.

Research Article

The Mathematical Foundations of 3D Compton Scatter Emission Imaging

T. T. Truong,¹ M. K. Nguyen,² and H. Zaidi³

¹Laboratoire de Physique Théorique et Modélisation, CNRS UMR 8089, Université de Cergy-Pontoise,
2 Avenue Adolphe Chauvin, 95302 Cergy-Pontoise, France

²Laboratoire Equipes de Traitement des Images et du Signal, CNRS UMR 8051, Ecole Nationale Supérieure de l' Electronique
et de ses Applications, Université de Cergy-Pontoise, 6 Avenue du Ponceau, 95014 Cergy-Pontoise, France

³Division of Nuclear Medicine, Geneva University Hospital, 1211 Geneva 4, Switzerland

Received 27 September 2006; Accepted 20 February 2007

Recommended by Zhaotian Zhang

The mathematical principles of tomographic imaging using detected (unscattered) X- or gamma-rays are based on the two-dimensional Radon transform and many of its variants. In this paper, we show that two new generalizations, called conical Radon transforms, are related to three-dimensional imaging processes based on detected Compton scattered radiation. The first class of conical Radon transform has been introduced recently to support imaging principles of collimated detector systems. The second class is new and is closely related to the Compton camera imaging principles and invertible under special conditions. As they are poised to play a major role in future designs of biomedical imaging systems, we present an account of their most important properties which may be relevant for active researchers in the field.

Copyright © 2007 T. T. Truong et al. This is an open access article distributed under the Creative Commons Attribution License, which permits unrestricted use, distribution, and reproduction in any medium, provided the original work is properly cited.

1. INTRODUCTION

During the last fifty years, progress in imaging systems using penetrating radiation for biomedical purposes has brought about new topics in mathematics and fueled intense research activities with far reaching results. The mathematics of imaging science has evolved to a full fledged discipline [1]. Transmission computer assisted tomography (CAT-scanning) is based on an integral transform in two dimensions discovered in the sixties by Cormack [2–4], who did not realize that J. Radon had already introduced and studied it in his seminal paper [5] in 1917. Subsequently, in an effort to reconstruct directly in three dimensions an object without having to assemble its two-dimensional sections, one is led to consider the so-called X-ray transform or cone beam transform. This transform is an off-spring of the Radon transform and maps a function in \mathbb{R}^3 to its (straight) line integrals in \mathbb{R}^3 . One way to reconstruct an object is to convert the line data into planar data in \mathbb{R}^3 using the Grangeat technique [6]. Then application of the inversion formula of the three-dimensional Radon transform [7] yields the answer. A further generalization of the Radon transform in emission imaging, called the attenuated X-ray transform, accounts for the radiation loss in the

traversed medium. The problem of its inversion has been a mathematical challenge for decades and has been solved only in 2001 [8], thanks to complex analysis methods applied to the stationary photon transport problem [9]. The success of this branch of mathematics, coined by Gelfand as integral geometry, goes far beyond the imaging science scope as it has brought significant progress in group representation theory, partial differential equations, boundary value problems, and so forth [7].

The standard Radon transform and its variants are related to a process of data collection in an interaction free propagation of radiation through matter, possibly affected by attenuation. Thus, radiation energy is not altered from emission to detection. However, a sizable part of traveling radiation does suffer an interaction with matter through Compton scattering [10]. Generally as the data quality is lowered, Compton scattering effects have been treated as noise and must be eliminated. So far, in most image processing methods, the aim is to deal away with it, for example, by filtering or by geometric rejection using an antiscatter grid of miniature lead septa. In conventional projection imaging, most of the radiation have been scattered in the patient body, the scatter-to-primary ratio can be as high as 10 [10].

But throwing out all the scattered radiation may not be a smart move since this also means a loss of sensitivity and certainly a loss of valuable information.

This is why we have recently advocated the use of scattered radiation to improve quality in image processing [11] as well as to construct new imaging principles [12]. This proposal generalizes the concept of a Compton camera, proposed by several workers some thirty years ago [13–15], in which the idea of electronic collimation is implemented. When radiation is detected at a lower energy than the originally emitted energy, there must be at least one Compton scattering occurring along its propagation path. But the vast majority of scattered radiation is due to mainly single scattering events [16]. To an emerging ray detected at a definite energy there corresponds an ensemble of incoming rays distributed on a circular cone of definite opening angle. The measured data consisting of collected emerging radiation at some detection point is viewed as the integral contribution of a source function on specific circular cones; it may be also called a conical projection of the source. The name of conical Radon transform is attributed to such integral transform and is added to the list of already known Radon transforms on geometric manifolds in \mathbb{R}^3 : paraboloids [17], spheres [18], special surfaces [19], second-order surfaces [20], and so forth. Other proposals for use of scattered radiation in X-ray imaging which do not rely on conical projections have been made independently by [21].

Thus, the main topic addressed here is the mathematical framework defining the working principles of a new imaging technique. To keep the discussion transparent, we have adopted an ideal working assumption whereby attenuation is not taken into account. A well-known difficulty is that the nonuniform attenuation along the radiation path leads to tremendous mathematical complication. For a given projection, attenuation correction factors in SPECT rarely exceed 10 in virtually all clinical imaging situations [22]. An exact solution is beyond the scope of the present study. It should be pointed out that, in the case of the attenuated X-ray transform in emission imaging, a comprehensive analytic solution has been attained only recently [9]. Therefore, in practical situations standard corrections for photon attenuation should be envisaged.

In conventional emission imaging, the data collected for object reconstruction is formed by linear projections (cone beam projections) of unscattered radiation filtered by an energy acquisition window which has already discarded from 70% to 80% of the incident photon flux. Moreover, among the retained some have suffered scattering in the collimator and hence must be discarded. It has been reported that collimator scatter increases as the energy of the photopeak of interest increases from a low of 1.9% for Tc-99m (141 keV) to a high of 29.4% for I-131 (364 keV) with the usual high-energy collimator. The penetration percentage also goes up with energy. Therefore, correction for photons that penetrate through, or scatter in, collimator septa is hardly important at all for Tc-99m tracers [23].

In the proposed imaging technique, data for reconstruction are provided by the so-called conical projections, which

gather radiation from point sources lying on large surfaces inside the emitting object. Although contamination of the scatter component by multiple scatter events may be as high as 30% of the total scatter according to Monte Carlo investigations [16, 24], we believe that the signal of single scattered radiation is largely sufficient to make the new imaging principles work, in particular when advanced semiconductor-based detectors with better energy and spatial resolution and sensitivity will become available. These interesting issues will be explored in future work.

In this paper, we present a unified treatment of conical Radon transforms relevant in emission imaging by scattered radiation. In fact, we will be concerned with two classes of conical Radon transforms originating from image formation by Compton scattered radiation on a gamma camera with and without collimator. The first class of conical Radon transform uses circular cone sheets with fixed axis direction (\mathcal{C}_1 -cones) whereas the second class deals with circular cone sheets with axis swinging around a point (\mathcal{C}_2 -cones). Note that if this point goes to infinity in a given spatial direction, then the \mathcal{C}_2 -cone goes over the \mathcal{C}_1 -cone. In each case, we will start by showing how the image formation process leads to an integral transform and how this transform is related to the conical Radon transforms. Each conical transform will be introduced and its relevant properties for imaging purposes, in particular their invertibility, discussed. Conclusions and perspectives are given in the last section.

2. NOTATIONS

Let f be a real nonnegative integrable, smooth, with compact support function on \mathbb{R}^3 . The same function in cylindrical (spherical) coordinates is noted $f(f)$.

The definitions of various transforms of $f(x, y, z)$ are as follows:

- (i) \hat{f}_i : Conical \mathcal{C}_i -Radon transform of f , $i = 1, 2$;
- (ii) F_j : j -dimensional Fourier transform of f , $j = 1, 2, 3$.

Special functions [25] are as follows:

- (i) $Y(x)$: Heaviside unit step function;
- (ii) $j_l(kr)$: spherical Bessel function of order l and variable (kr) ;
- (iii) $P_l(\cos \theta)$: Legendre polynomial of order l and of variable $\cos \theta$;
- (iv) $Y_{l,m}(\Omega_k)$: spherical harmonic (l, m) with argument Ω_k , solid angle in the direction of the unit vector \mathbf{k} .

3. WORK SETTING

In this article, we consider the emission imaging problem, that is, the problem of reconstructing in \mathbb{R}^3 a gamma-ray radiating object from its Compton scattered radiation data. This object is described by its activity volume density function f . Detection of scattered radiation is performed by a gamma camera in two instances: with or without collimator. The recorded data consists of the coordinates of the detection site, the surface flux density of photons at this site (pixel), and the value of their energy (list mode). Between the radiating

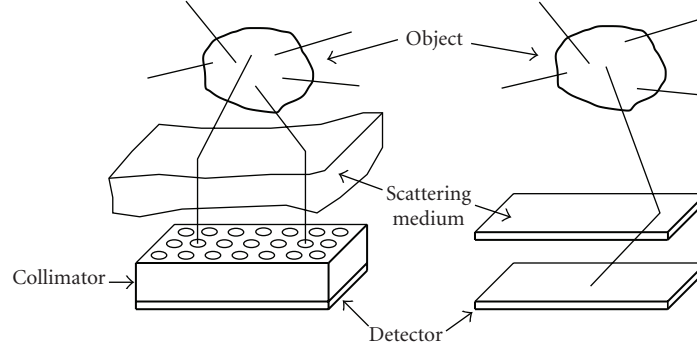


FIGURE 1: Two imaging modalities using scattered radiation with and without collimation.

object and the detector stands a scattering medium: it may be a volume or a layer as illustrated by Figure 1. Note that the object itself may also be a scattering medium, and for photon energies above 25 keV, over 50% of the interactions in biological tissues are scatterings [26]. Higher-order scattering events (of much lower probability of occurrence) will be the object in future studies.

3.1. Compton scattering

As Compton scattering plays a key role, we will recall some of its properties. The Compton effect discovered in 1923 [27] had served to confirm the particle (photon) nature of radiation, as proposed by A Einstein. Thus, energetic radiation under the form of X- or gamma-rays behave like particles and scatter with electrically charged particles in matter. In biomedical domains, X- or gamma-photons scatter electrons in the biological media they traverse. This scattering process has cylindrical symmetry around the direction of the incoming photon and the energy of the outgoing photon is given by the Compton formula [28]

$$E = E_0 \frac{1}{1 + \varepsilon(1 - \cos \omega)}, \quad (1)$$

where ω is the scattering angle as measured from the incident photon direction, E_0 , the photon initial energy, $\varepsilon = E_0/mc^2$, and mc^2 the rest energy of the electron. Equation (1) shows that single-scattered photons have a continuous energy spectrum in the range $E_0/(1 + 2\varepsilon) \leq E \leq E_0$.

Thus an emerging photon with an energy E in a direction of unit vector \mathbf{n} may originate from an incoming photon of energy E_0 emitted from a site on a sheet of a circular cone of axis direction \mathbf{n} and an opening angle ω .

3.2. Compton differential cross-section

At a scattering site \mathbf{M} , the number of particles d^2N_{sc} scattered in a solid angle $d\Omega_{sc}$ along a direction making an angle ω with the incident direction follows from the definition of the

differential scattering cross-section (see Figure 2)

$$\frac{d\sigma_C}{d\Omega}, \quad (2)$$

when the following quantities are given:

- (a) ϕ_{in} , the incident photon flux density,
- (b) $n_e(\mathbf{M})d\mathbf{M}$, the number of scatterers (electrons) around the scattering site \mathbf{M} with volume $d\mathbf{M}$.

We have

$$d^2N_{sc} = \phi_{in} n_e(\mathbf{M}) d\mathbf{M} \left(\frac{d\sigma_C}{d\Omega} \right) d\Omega_{sc}. \quad (3)$$

The Compton differential cross-section has been computed in 1929 by Klein and Nishina [29]. It appears as the product of the area of a disk of radius r_e , the classical radius of the electron, and a probability factor $P(\omega)$, that is,

$$\left(\frac{d\sigma_C}{d\Omega} \right) = (\pi r_e^2) P(\omega), \quad (4)$$

where $r_e = 2.82 \times 10^{-15}$ m and

$$P(\omega) = \frac{1}{2\pi} \frac{1}{[1 + \varepsilon(1 - \cos \omega)]^2} \left(1 + \cos^2 \omega + \frac{(1 - \cos^2 \omega)}{1 + \varepsilon(1 - \cos \omega)} \right). \quad (5)$$

Thus, we see that, for a given incident energy, the angular distribution of scattered photons is no longer isotropic [28].

Hence, the final form of this number of scattered photons in the direction given by the angle ω is

$$d^2N_{sc} = \phi_{in} n_e(\mathbf{M}) d\mathbf{M} r_e^2 P(\omega) d\Omega_{sc}, \quad (6)$$

this number is basic to the image formation by scattered radiation.

3.3. Conical projections

In standard computer assisted tomography (CAT), the data is gathered under the form of line projections or integrals of a function (attenuation or activity) along straight lines.

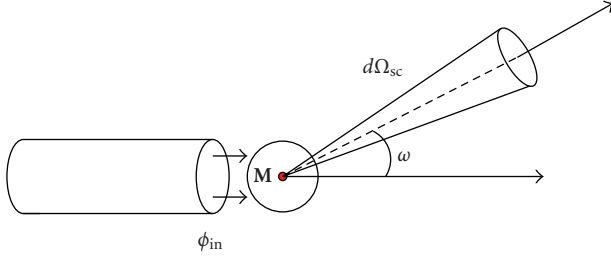


FIGURE 2: Compton scattering differential cross-section.

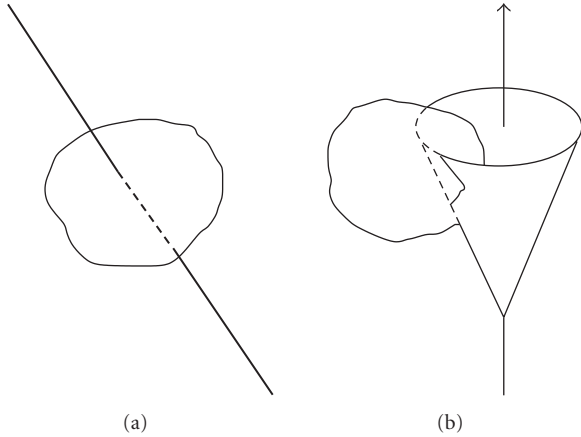


FIGURE 3: Illustration of linear and conical projections.

Here following the scattering mechanism, the data would appear as conical projections or integrals of a function f on a circular cone sheets. The integration is carried out with the Lebesgue measure of the cone in a chosen coordinate system. The result is a function of

- (i) the coordinates of the cone vertex,
- (ii) the parameters of the unit vector of the cone axis,
- (iii) the opening angle of the cone, that is, ω the scattering angle.

Figure 3 displays the representations of line projection and conical projection. In the text we will have two types of conical projections corresponding to the two cases of image formation mentioned earlier. The question is now how to use the conical projections to reconstruct the source function f . We will treat the two cases separately in the coming sections.

4. THE \mathcal{C}_1 -CONICAL RADON TRANSFORM

In this section, we consider the possibility of imaging a three-dimensional object by collecting data on its scattered radiation on a gamma camera equipped with a collimator and show how the \mathcal{C}_1 -conical Radon transform arises. Figure 1 shows the experimental arrangement with the location of the radiating object, the scattering medium, and the collimated gamma camera.

4.1. Image formation in gamma imaging by scattered radiation

To concentrate on the scattered imaging principle, we make some simplifying assumptions [12, 30]:

- (1) absence of attenuation for the propagating radiation,
- (2) constant density of the electrons n_e in the scattering medium,
- (3) isotropic emission from original radioisotopes in object.

To compute the photon flux density at a detection site (pixel) \mathbf{D} on the collimated camera we start from (6). Radiation is emitted at point source \mathbf{S} , will propagate to scattering site \mathbf{M} and reach detection site \mathbf{D} .

The incoming photon flux density ϕ_{in} on scattering site \mathbf{M} is now computed from the emission data from point source. Let $f(\mathbf{S})d\mathbf{S}$ be the number of gamma photons emitted per unit time by a volume $d\mathbf{S}$ in the object around site \mathbf{S} . The emission being isotropic, the number of photons emitted in the direction \overrightarrow{SM} in a solid angle $d\Omega_S$ is

$$\frac{f(\mathbf{S})d\mathbf{S}}{4\pi}d\Omega_S. \quad (7)$$

Therefore, the incoming photon flux density at scattering site \mathbf{M} is

$$\frac{f(\mathbf{S})d\mathbf{S}}{4\pi} \frac{1}{SM^2} = \phi_{in}, \quad (8)$$

where $SM = |\overrightarrow{SM}|$.

Next, the number of scatterers around site \mathbf{M} in a volume $d\mathbf{M}$ is $n_e d\mathbf{M}$. The net number of photons emerging from the scattering is

$$\frac{f(\mathbf{S})d\mathbf{S}}{4\pi} \frac{1}{SM^2} n_e d\mathbf{M} \pi r_c^2 P(\omega) d\Omega_M, \quad (9)$$

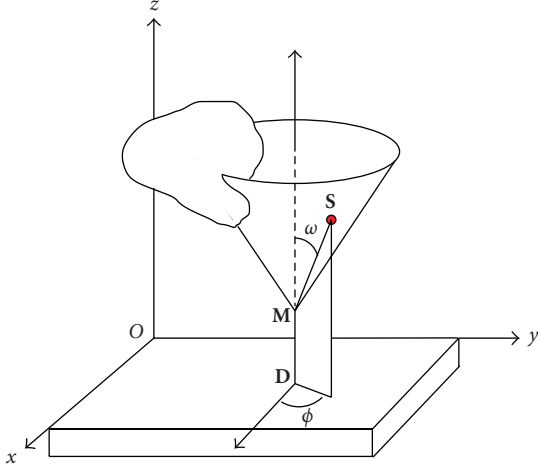
this means that the detected photon flux density at site \mathbf{D} is

$$\frac{f(\mathbf{S})d\mathbf{S}}{4\pi} \frac{1}{SM^2} n_e d\mathbf{M} \pi r_c^2 P(\omega) \frac{1}{MD^2}. \quad (10)$$

Now, all the contributing point sources \mathbf{S} , for given scattering center \mathbf{M} , lie on a circular cone sheet of axis identified with \overrightarrow{MD} and opening angle ω , thus we must integrate with the measure $\delta(\text{cone})d\mathbf{S}$ first. Next, we must take into account all the scattering sites in the scattering medium situated on the line parallel to the collimator axis at site \mathbf{D} . Hence, we must perform a second integration with the measure $\delta(\text{line})d\mathbf{M}$. To sum up the detected photon flux density at \mathbf{D} is

$$g(\mathbf{D}, \omega) = \iint \delta(\text{cone}) \frac{f(\mathbf{S})d\mathbf{S}}{4\pi} \frac{1}{SM^2} n_e d\mathbf{M} \pi r_c^2 P(\omega) \times \delta(\text{line}) \frac{1}{MD^2}. \quad (11)$$

In the cylindrical coordinate system of Figure 4, the integration measure on the cone is $r \sin \omega dr d\phi$ and the measure

FIGURE 4: \mathcal{C}_1 -cone and \mathcal{C}_1 -conical Radon transform definition.

along the line is simply dz_M , (11) becomes

$$g(\mathbf{D}, \omega) = \pi r_e^2 P(\omega) \frac{n_e}{4\pi} \iint r \sin \omega \, dr \, d\phi \times f(x_D + r \sin \omega \cos \phi, y_D + r \sin \omega \sin \phi, z_M + r \cos \omega) \frac{dz_M}{z_M^2}. \quad (12)$$

Remark 1. In practice as f and n_e are volume densities, to keep the physical dimensions right, we should think of the cone sheet as having a small thickness e and the line on which \mathbf{M} moves as having a tiny section s . These are constants and do not affect the mathematical reasoning, they will be dropped for the sake of expression simplicity, but should always be kept in mind.

Clearly this imaging equation is a compounded integral transform. Assuming that integration interchange is valid, if we define the first integral transform as

$$h(x_D + r \sin \omega \cos \phi, y_D + r \sin \omega \sin \phi, r \cos \omega) = \int \frac{dz_M}{z_M^2} f(x_D + r \sin \omega \cos \phi, y_D + r \sin \omega \sin \phi, z_M + r \cos \omega), \quad (13)$$

we see that the imaging equation (12) is just a conical projection of the function h on the \mathcal{C}_1 -cones with vertex on the plane xOy .

Let us define an interaction factor which also includes e and s :

$$K(\omega) = \pi r_e^2 P(\omega) \frac{n_e}{4\pi} es, \quad (14)$$

then (12) reads

$$\frac{g(\mathbf{D}, \omega)}{K(\omega)} = \iint r \sin \omega \, dr \, d\phi h(x_D + r \sin \omega \cos \phi, y_D + r \sin \omega \sin \phi, r \cos \omega), \quad (15)$$

or in terms of our notations (see Section 2)

$$\frac{g(\mathbf{D}, \omega)}{K(\omega)} = \hat{h}_1(x_D, y_D, \omega). \quad (16)$$

4.2. Properties of the \mathcal{C}_1 -conical transform

The \mathcal{C}_1 -conical Radon transform has been discussed in [31], where some of its properties have been studied. However, the problem of inversion will be handled here with a new approach. We will not go through the method of decomposition of functions in circular components but will show that there exists a variant of the *central slice theorem* [28] which provides the grounds to invert the transform as it is done in the standard Radon transform [28].

First, we observe that by definition in the chosen cylindrical coordinate system the \mathcal{C}_1 -conical Radon transform of f , the cones having vertex on the xOy plane, is

$$\hat{f}_1(x_D, y_D, \omega) = \iint r \sin \omega \, dr \, d\phi f(x_D + r \sin \omega \cos \phi, y_D + r \sin \omega \sin \phi, r \cos \omega). \quad (17)$$

This can be rewritten under the form of a Fredholm integral equation of the first kind with a delta function kernel concentrated on the sheet of a circular cone [31]

$$\hat{f}_1(x_D, y_D, \omega) = \iiint dx \, dy \, dz \mathcal{K}_1(x_D, y_D, \omega \mid x, y, z) f(x, y, z), \quad (18)$$

with

$$\mathcal{K}_1(x_D, y_D, \omega \mid x, y, z) = \delta\left(\cos \omega \sqrt{(x - x_D)^2 + (y - y_D)^2} - z \sin \omega\right). \quad (19)$$

We use now the Fourier representation of the delta function

$$\delta\left(\cos \omega \sqrt{(x - x_D)^2 + (y - y_D)^2} - z \sin \omega\right) = \int_{-\infty}^{\infty} d\nu \exp 2i\pi\nu \left(\cos \omega \sqrt{(x - x_D)^2 + (y - y_D)^2} - z \sin \omega\right), \quad (20)$$

and the two-dimensional Fourier transform of $f(x, y, z)$,

$$f(x, y, z) = \int dp \, dq e^{2i\pi(px+qy)} F_2(p, q, z). \quad (21)$$

We can perform the integration over z , which restores a three-dimensional Fourier transform $F_3(p, q, r)$ of f and

yields a new form of $\hat{f}(x_S, y_S, \omega)$,

$$\begin{aligned} & \hat{f}(x_S, y_S, \omega) \\ &= \int dx dy \int_{-\infty}^{\infty} d\nu \exp 2i\pi\nu \left(\cos \omega \sqrt{(x-x_S)^2 + (y-y_S)^2} \right) \\ & \quad \times \int dp dq e^{2i\pi(px+qy)} F_3(p, q, \nu \sin \omega). \end{aligned} \quad (22)$$

Let $\hat{F}_2(p, q, \omega)$ be Fourier component with respect to the coordinates x_S and y_S of $\hat{f}(x_S, y_S, \omega)$, then

$$\begin{aligned} \hat{F}_2(p, q, \omega) &= \int_{-\infty}^{\infty} d\nu F_3(p, q, \nu \sin \omega) \iint dx dy \exp 2i\pi \\ & \quad \times \left[\nu \cos \omega \sqrt{(x-x_S)^2 + (y-y_S)^2} \right. \\ & \quad \left. + (p(x-x_S) + q(y-y_S)) \right]. \end{aligned} \quad (23)$$

The last integral of (23) can be computed using polar coordinates in (x, y) and (p, q) spaces, that is, $(x-x_S) = \rho \cos \beta$, $(y-y_S) = \rho \sin \beta$, $dx dy = \rho d\rho d\beta$, and $p = k \cos \alpha$, $q = k \sin \alpha$, $k dk d\alpha$. Therefore,

$$\begin{aligned} & \iint dx dy \exp 2i\pi \left[\nu \cos \omega \sqrt{(x-x_S)^2 + (y-y_S)^2} \right. \\ & \quad \left. + (p(x-x_S) + q(y-y_S)) \right] \\ &= \iint \rho d\rho d\beta e^{2i\pi[\nu \rho \cos \omega + k\rho \cos(\beta-\alpha)]}. \end{aligned} \quad (24)$$

Integration on β yields a Bessel function of order zero in the last integral of (24):

$$\begin{aligned} & \iint \rho d\rho d\beta e^{2i\pi[\nu \rho \cos \omega + k\rho \cos(\beta-\alpha)]} \\ &= \int_0^{\infty} \rho d\rho e^{2i\pi\nu\rho \cos \omega} 2\pi J_0(2\pi k\rho). \end{aligned} \quad (25)$$

Thus, in two-dimensional Fourier space, the \mathcal{C}_1 -conical Radon transform appears as

$$\begin{aligned} \hat{F}_2(p, q, \omega) &= \int_{-\infty}^{\infty} d\nu \int_0^{\infty} \rho d\rho 2\pi J_0(2\pi\rho\sqrt{p^2+q^2}) \\ & \quad \times F_3(p, q, \nu \sin \omega) e^{2i\pi\nu\rho \cos \omega}. \end{aligned} \quad (26)$$

Now, we perform the integration on ν which brings back the three-dimensional Fourier transform of f ,

$$\int_{-\infty}^{\infty} d\nu F_3(p, q, \nu \sin \omega) e^{2i\pi\nu\rho \cos \omega} = \frac{1}{\sin \omega} F_2(p, q, \rho \cot \omega). \quad (27)$$

This step reduces the \mathcal{C}_1 -conical Radon transform to a Hankel of order zero:

$$\begin{aligned} & \sin \omega \hat{F}_2(p, q, \omega) \\ &= \int_0^{\infty} \rho d\rho 2\pi J_0(2\pi\rho\sqrt{p^2+q^2}) F_2(p, q, \rho \cot \omega). \end{aligned} \quad (28)$$

To perform the inversion of this Hankel transform, we should switch to an appropriate variable, that is, $\zeta = \rho \cot \omega$. But care must be exercised as far as the range of ω is concerned. We will distinguish two cases.

(a) $0 < \omega < \pi/2$, then $\zeta > 0$ as well as $\tan \omega > 0$ and (28) can be rewritten as

$$\begin{aligned} & \sin \omega \cot^2 \omega \hat{F}_2(p, q, \omega < \frac{\pi}{2}) \\ &= \int_0^{\infty} \zeta d\zeta 2\pi J_0(2\pi\zeta \tan \omega \sqrt{p^2+q^2}) F_2(p, q, \zeta). \end{aligned} \quad (29)$$

(b) $\pi/2 < \omega < \pi$, then $\zeta < 0$ as well as $\tan \omega < 0$ and (28) can be rewritten as

$$\begin{aligned} & \sin \omega \cot^2 \omega \hat{F}_2(p, q, \omega > \frac{\pi}{2}) \\ &= \int_0^{\infty} \zeta d\zeta 2\pi J_0(2\pi\zeta \tan \omega \sqrt{p^2+q^2}) F_2(p, q, -\zeta). \end{aligned} \quad (30)$$

Application of the Hankel identity [25]

$$\frac{1}{k} \delta(k-k') = \int_0^{\infty} r dr 2\pi J_1(2\pi kr) 2\pi J_1(2\pi k' r) \quad (31)$$

leads to the inversion of the Hankel transforms and yields the three-dimensional Fourier components of the object f . As the dual variable to ζ is $\tau\sqrt{p^2+q^2}$, with $\tau = \tan \omega$, we get

$$\begin{aligned} F_2(p, q, \zeta) &= (p^2+q^2) \int_0^{\infty} \tau d\tau 2\pi J_0(2\pi\zeta \tan \omega \sqrt{p^2+q^2}) \\ & \quad \times \frac{1}{|\tau|\sqrt{1+\tau^2}} \left(Y\left(\frac{\pi}{2}-\omega\right) \hat{F}_2(p, q, \omega < \frac{\pi}{2}) \right. \\ & \quad \left. + Y\left(\omega-\frac{\pi}{2}\right) \hat{F}_2(p, q, \omega > \frac{\pi}{2}) \right). \end{aligned} \quad (32)$$

Hence, f can be recovered by inverse three-dimensional Fourier transform.

Remark 2. In order to reconstruct the object by inverting the compound integral transform given by (12), we need to invert (13). This is quite easy since it can be viewed as a convolution in the variable z_D between the two functions $1/z_D^2$ and $f(\dots, z_D + r \cos \omega)$. As this operation is not important to the topic of this paper, we refer the reader to [12, 30].

5. THE \mathcal{C}_2 -CONICAL RADON TRANSFORM

5.1. Compton camera

That Compton effect which has been proposed as mechanism for imaging is known ever since the fifties. However, there are many ways to do the experimental setups. Most proposals are systems with collimated point source and point-like detector, see, for example, [21]. In fact the Compton effect is used to probe the electron density of matter and applied often to nondestructive material control. Here we are

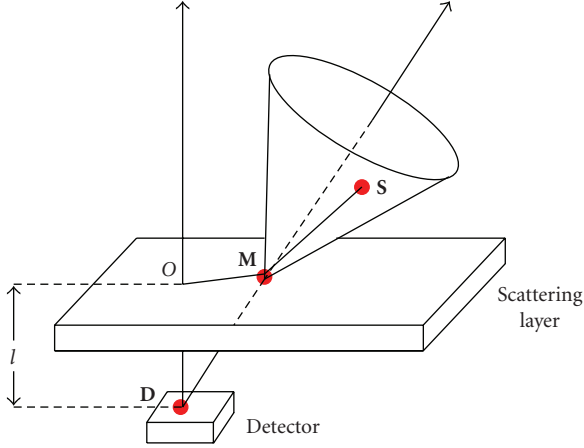


FIGURE 5: Principle of a Compton camera.

interested in data collected by a gamma camera. In the previous section we have examined the case of a gamma camera with a lead collimator which has the disadvantage of rejecting many of the scattered photons. So to improve drastically detection sensitivity, the idea of a Compton camera has been proposed as early as 1974 by many workers [13–15, 32].

The concept of a Compton camera is analogous to the scheme of Section 4 except that the scattering medium is now a thin scattering layer parallel to the face of a gamma camera without collimator. The data consists of \mathcal{C}_2 -conical projections, the cone sheet axis converging to the detection site \mathbf{D} ; see Figure 5. Note that when $\mathbf{D} \rightarrow \infty$ in a given direction we recover the \mathcal{C}_1 cones.

Following the image formation process in a Compton camera, we will show how a new conical Radon transform, the \mathcal{C}_2 -Radon transform, comes up and sketch a proof of its invertibility under specific conditions. The true conical Radon transform of a Compton camera is not yet an analytical inversion formula.

5.2. Image formation by scattered radiation in Compton camera

The radiating object stands above the first scattering layer. Its primary rays hit the scattering layer and will be absorbed by the planar camera (see Figure 5). If only photons of energy E below the energy E_0 of the primary photons are recorded, then each detection site collects all possible conical projections coming from all directions in half space, delimited by the photon absorbing detector. This is the principle of electronic collimation which has been designed to improve sensitivity of gamma cameras.

To reconstruct an object described by a source function $f(x, y, z)$, we need a set of data consisting of conical projections depending also on three variables. Ideally one could select one detection site \mathbf{D} , and consider all the projections along circular cones of opening angle ω and axis swinging around \mathbf{D} but with cone vertex constrained to be on a plane. With these conditions a conical projection will depend on

three parameters: the scattering angle ω and the two coordinates of the cone vertex on the scattering plane. Thus, we obtain a mapping of f onto a function of three variables. The inverse mapping, when explicitly worked out, would yield a correct imaging procedure by a Compton camera.

Following the assumptions of Section 4.1, the photon flux density at detection site \mathbf{D} is evaluated in the same manner as for the case with collimator:

$$g(\mathbf{D}, \omega) = \iint e\delta(\text{cone}) \frac{f(\mathbf{S})d\mathbf{S}}{4\pi} \frac{1}{SM^2} \times n_e d\mathbf{M}\pi r_e^2 P(\omega) s\delta(\text{line}) \frac{1}{MD^2}. \quad (33)$$

Now in the chosen coordinate system (see Figure 5), it has the expression

$$g(\mathbf{D}, \omega) = K(\omega) \iint \delta(\text{cone}) f(\mathbf{S}) d\mathbf{S} \frac{1}{SM^2} \times dx_M dy_M \frac{1}{l^2 + x_M^2 + y_M^2}, \quad (34)$$

l being the distance OD , the explicit integration on the cone sheet $\delta(\text{cone})d\mathbf{S}$ will be given later in Section 5.3 since it is related to the \mathcal{C}_2 -conical Radon transform we will be examining.

Up to now there exists only a few attempts to exactly solve this inversion problem. Cree and Bones [33] were the first to consider conical projections on a Compton camera which still has a collimator. Later on Basko et al. [34] as well as Parra [35] have designed inversion techniques based on properties of spherical harmonics as they consider conical projections as made up of cone beam projections, but have not touch really upon the problem of converting cone beam data into conical projection data, a problem similar to the one solved by Grangeat [6] for planar projections in \mathbb{R}^3 . There are numerous approximate reconstruction methods, most of them using some back projection techniques (or numerical algorithms) and search for point sources as intersections of cone sheets reconstructed from coincidence measurements on the Compton camera. Lastly let us also cite some other original approaches based on statistical physics [36] as well as algebraic methods [37–39].

In this situation, it is of interest to find an analytic inversion of the *special* \mathcal{C}_2 -conical Radon transform responsible for the imaging process in Compton camera. Before tackling this problem, we discuss here a more general problem in which the vertex of the scattering cone is not constraint to lie on a plane (or a surface) as in the Compton camera case. This would give us some freedom to find an inversion formula for another class of \mathcal{C}_2 -conical Radon transform. We will come back to the Compton camera in another work. Thus, the mathematics of the Compton camera imaging process have led to a new class of conical Radon transform.

5.3. Properties of the \mathcal{C}_2 -conical Radon transform

The \mathcal{C}_2 -cone is generated by the rotation of a straight line making an angle ω around an axis direction \mathbf{n} and meeting

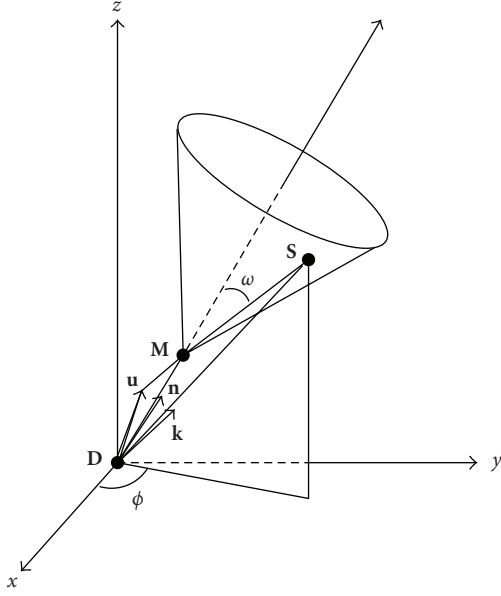


FIGURE 6: \mathcal{C}_2 -cone and \mathcal{C}_2 -conical Radon transform definition.

this axis at vertex \mathbf{M} ; see Figure 6. Thus, \mathbf{D} being the detection point, we have $\overrightarrow{DM} = \mathbf{M} = p\mathbf{n}$. Let \mathbf{S} be a running point of the cone sheet and denote this point by $\overrightarrow{DS} = \mathbf{S} = r\mathbf{k}$. Let the angle γ be defined by $(\mathbf{k} \cdot \mathbf{n}) = \cos \gamma$. Thus, by considering trigonometric relations in the triangle DMS , one can write down the relation

$$r = p \frac{\sin \omega}{\sin(\omega - \gamma)} = p \frac{\sin \omega}{\sin(\omega - \cos^{-1}(\mathbf{k} \cdot \mathbf{n}))}, \quad (35)$$

which may be regarded as the cone equation in a meridian section within polar coordinates (r, γ) and polar axis \mathbf{n} . At $\omega = \pi/2$ we recover the equation of a plane as a degenerate cone [28].

When evaluating a \mathcal{C}_2 -conical projection, we integrate a nonnegative function f on one sheet of the cone. This is equivalent to saying that, giving a ‘‘mass’’ density, we compute the ‘‘mass’’ of a piece of cone surface limited by the intersection curve of the support of f with the cone. This ‘‘mass’’ may be calculated in any convenient coordinate system.

We will use the coordinate system which is expressed in (35). The area element of the cone is the product of the arc element of the line by the element of circle in a plane perpendicular to the cone axis.

The arc element is

$$ds = \sqrt{(dr)^2 + (r d\gamma)^2} = \frac{p \sin \omega}{\sin(\omega - \gamma)} \frac{d\gamma}{\sin(\omega - \gamma)}. \quad (36)$$

Now the element of circle is $r \sin \gamma d\psi$. Hence, the cone area element is

$$\begin{aligned} da &= r \sin \gamma d\psi \times \frac{p \sin \omega}{\sin(\omega - \gamma)} \frac{d\gamma}{\sin(\omega - \gamma)} \\ &= \sin \gamma d\psi \times \left(\frac{p \sin \omega}{\sin(\omega - \gamma)} \right)^2 \frac{d\gamma}{\sin(\omega - \gamma)}. \end{aligned} \quad (37)$$

In the same coordinate system, a \mathcal{C}_2 -conical projection of f is expressed as the integral of f on the cone sheet with the integration measure da . f has then the expression $f(r, \Omega_k)$, with $\Omega_k = (\gamma, \psi)$, $r = p \sin \omega / \sin(\omega - \gamma)$ and angular ranges $0 < \gamma < \omega$ and $0 < \psi < 2\pi$. Thus,

$$\begin{aligned} \hat{f}_2(p\mathbf{n}, \omega) &= \int f \left(p \frac{\sin \omega}{\sin(\omega - \gamma)}, \Omega_k \right) \sin \gamma d\psi \\ &\quad \times \left(\frac{p \sin \omega}{\sin(\omega - \gamma)} \right)^2 \frac{d\gamma}{\sin(\omega - \gamma)}, \end{aligned} \quad (38)$$

or alternatively

$$\begin{aligned} \hat{f}_2(p\mathbf{n}, \omega) &= \int (f(r, \Omega_k) r^2)_{r=p(\sin \omega / \sin(\omega - \gamma))} \\ &\quad \times \sin \gamma d\psi \frac{d\gamma}{\sin(\omega - \gamma)}. \end{aligned} \quad (39)$$

One may use the integration over a one-dimensional delta function to express the substitution of r by the cone equation (35):

$$\int_{-\infty}^{\infty} dr \delta \left(r - p \frac{\sin \omega}{\sin(\omega - \gamma)} \right). \quad (40)$$

Since

$$\delta \left(r - p \frac{\sin \omega}{\sin(\omega - \gamma)} \right) \frac{1}{\sin(\omega - \gamma)} = \delta(p \sin \omega - r \sin(\omega - \gamma)), \quad (41)$$

and $r^2 dr \sin \gamma d\psi d\gamma = r^2 dr d\Omega_k = d\mathbf{S}$, we can replace the original integration range:

$$\{r \in \mathbb{R}, 0 < \gamma < \omega, 0 < \psi < 2\pi\}, \quad (42)$$

by

$$\begin{aligned} \{r \in \mathbb{R}_+, \Gamma = [0 < \gamma < \omega \cup \pi < \gamma < \omega + \pi], \\ \mathbb{S}^1 = [0 < \psi < 2\pi]\}, \end{aligned} \quad (43)$$

which fits in the chosen spherical coordinate system with \mathbf{n} as polar axis.

The \mathcal{C}_2 -conical projection of f has now the Fredholm form of the first kind with a delta function kernel. In intrinsic vector notations, it reads

$$\hat{f}_2(p\mathbf{n}, \omega) = \int d\mathbf{S} f(\mathbf{S}) \mathcal{K}_2(p\mathbf{n}, \omega | \mathbf{S}), \quad (44)$$

where

$$\mathcal{K}_2(p\mathbf{n}, \omega | \mathbf{S}) = \delta(p \sin \omega - r \sin(\omega - \cos^{-1}(\mathbf{k} \cdot \mathbf{n}))). \quad (45)$$

(Compare with the previous case, see (18), (19)).

Finally, at $\omega = \pi/2$ we recover precisely the planar Radon projection in \mathbb{R}^3 :

$$\hat{f}_2 \left(p\mathbf{n}, \frac{\pi}{2} \right) = \int d\mathbf{S} f(\mathbf{S}) \delta(p - r(\mathbf{k} \cdot \mathbf{n})). \quad (46)$$

5.4. A central slice-like theorem

Again as in Section 4, we may use the Fourier decomposition of the delta function¹

$$\begin{aligned} & \delta(p \sin \omega - r \sin(\omega - \gamma)) \\ &= \int_{-\infty}^{\infty} d\nu \exp -2i\pi\nu(p \sin \omega - r \sin(\omega - \gamma)), \end{aligned} \quad (47)$$

together with the decomposition of f into spherical components

$$f(x, y, z) = f(r, \Omega_k) = \sum_{l,m} f_{lm}(r) Y_{lm}(\Omega_k), \quad (48)$$

where, in the chosen spherical coordinate system, Ω_k denotes the direction parameters of the unit vector \mathbf{k} . Hence, inserting (47) and (48) in (44) we obtain

$$\begin{aligned} \widehat{f(p\mathbf{n}, \omega)} &= \sum_{l,m} \int_{-\infty}^{\infty} d\nu e^{-2i\pi\nu(p \sin \omega)} \\ &\times \int_0^{\infty} r^2 dr f_{lm}(r) \int_{\Gamma \cup \mathbb{S}^1} d\Omega_k Y_{lm}(\Omega_k) e^{2i\pi\nu r \sin(\omega - \gamma)}. \end{aligned} \quad (49)$$

Recall $\cos \gamma = (\mathbf{k} \cdot \mathbf{n})$. As $\sin(\omega - \gamma) = \cos(\pi/2 - \omega + \gamma)$, we introduce the decomposition of a plane wave in space in spherical components (see [40, page 471]):

$$\begin{aligned} & e^{2i\pi\nu r \cos(\pi/2 - \omega + \gamma)} \\ &= \sum_n i^n (2n+1) j_n(2\pi\nu r) P_n\left(\cos\left(\frac{\pi}{2} - \omega + \gamma\right)\right), \end{aligned} \quad (50)$$

where $j_n(x)$ is the spherical Bessel function of order n .²

Let \mathbf{u} be a fixed unit vector, defined by Ω_u , such that $\cos(\pi/2 - \omega + \gamma) = (\mathbf{k} \cdot \mathbf{u})$. Then the Legendre polynomial $P_n(\cos(\pi/2 - \omega + \gamma))$ can be further expanded in terms of spherical harmonics [25]:

$$\begin{aligned} & P_n \cos\left(\cos\left(\frac{\pi}{2} - \omega + \gamma\right)\right) \\ &= \frac{4\pi}{2n+1} \sum_{m'=-n}^{m'=n} Y_{nm'}^*(\Omega_k) Y_{nm'}(\Omega_u). \end{aligned} \quad (51)$$

Putting relation (51) in (50) and integrating on $d\Omega_k$, since the range of ϕ is \mathbb{S}^1 , we can write

$$\int_{\Gamma \cup \mathbb{S}^1} d\Omega_k Y_{lm}(\Omega_k) Y_{nm'}^*(\Omega_k) = \delta_{mm'} K_{ln}^m(\omega), \quad (52)$$

with $|m| < \inf(l, n)$. Thus, the result follows:

$$\begin{aligned} \widehat{f(p\mathbf{n}, \omega)} &= \sum_{n,m} Y_{nm}(\Omega_u) \int_{-\infty}^{\infty} d\nu e^{-2i\pi\nu(p \sin \omega)} 4\pi i^l \int_0^{\infty} r^2 dr \\ &\times \sum_l j_l(2\pi\nu r) K_{ln}^m(\omega) f_{lm}(r). \end{aligned} \quad (53)$$

Right-hand side of (53) expresses $\widehat{f(p\mathbf{n}, \omega)}$ as a spherical component expansion of the \mathcal{C}_2 -conical Radon transform in terms of the variable $p \sin \omega \mathbf{u}$, instead of $p\mathbf{n}$. So if the \mathcal{C}_2 -conical data can be rewritten under the form of a function of $p \sin \omega \mathbf{u}$ and of ω , with a spherical component decomposition, that is,

$$\widehat{f(p\mathbf{n}, \omega)} = g(p \sin \omega \mathbf{u}, \omega) = \sum_{lm} g_{lm}(p \sin \omega, \omega) Y_{lm}(\Omega_u), \quad (54)$$

then we can extract the new data spherical component as

$$\begin{aligned} g_{lm}(p \sin \omega, \omega) &= \int_{-\infty}^{\infty} d\nu e^{2i\pi\nu(p \sin \omega)} 4\pi i^l \int_0^{\infty} r^2 dr \\ &\times \sum_l j_l(2\pi\nu r) K_{ln}^m(\omega) f_{lm}(r). \end{aligned} \quad (55)$$

Now by Fourier inverting with respect to $q = p \sin \omega$ the two sides of (55), (since $\sin \omega > 0$ for $0 < \omega < \pi$), we find that

$$\begin{aligned} \sin \omega \int_{-\infty}^{\infty} dq g_{lm}(q, \omega) e^{2i\pi\nu q} \\ = 4\pi i^l \int_0^{\infty} r^2 dr \sum_l j_l(2\pi\nu r) K_{ln}^m(\omega) f_{lm}(r). \end{aligned} \quad (56)$$

Next, by appropriately choosing \mathbf{u} , a generalized Hankel identity may be derived. Recall that for spherical Bessel functions (see, e.g., [25]) this identity is of the form

$$\frac{1}{k^2} \delta(k - k') = \int_0^{\infty} \rho^2 d\rho 4\pi j_l(2\pi k \rho) 4\pi j_l(2\pi k' \rho). \quad (57)$$

This new identity allows to extract the spherical component $f_{lm}(r)$ of f and thereby achieve inversion (details will be presented elsewhere). Equation (54) relates implicitly p and ω and may suggest a new type of gamma camera realization, which should be investigated. Finally for $\omega = \pi/2$, (44) shows that this \mathcal{C}_2 -conical Radon transform is just the Radon transform in \mathbb{R}^3 . The whole procedure goes through with drastic simplifications since the natural choice for \mathbf{u} is \mathbf{n} , thus $\widehat{f(p\mathbf{n}, \omega)} = g(p\mathbf{u}, \omega)$.

6. CONCLUSIONS AND PERSPECTIVES

The Radon transform has enjoyed tremendous popularity in imaging science as it has been extended, generalized in pure mathematics (see, e.g., [19, 41, 42]) as well as exploited in many fields of applications [17, 43, 44]. In this paper we have presented two further generalizations of the Radon transform, namely, two classes of conical Radon transforms which

¹ As the delta function is an even function, the sign of the exponential under the integration sign may be chosen at will.

² This is valid for $\nu > 0$, otherwise we take the Fourier representation of the delta function with a different sign in (47) as indicated in the previous footnote.

originate from imaging processes using Compton scattered radiation. The first class, called \mathcal{C}_1 -conical Radon transform, is related to an imaging principle with a collimated gamma camera whereas the second class, called \mathcal{C}_2 -conical Radon transform, contains a special subclass which models the Compton camera imaging process. We have also shown that inversion of \mathcal{C}_2 -conical Radon transform can be achieved under a special condition which is not yet, for the moment, implemented in gamma-ray emission imaging science. Exploiting scattered radiation to reinforce sensitivity as well as enlarging field of view and cutting down operating time may lead to employing large scattering medium but without collimator for gamma cameras. The mathematics behind this perspective will be based on a yet little known Radon transform: the torus Radon transform, which may bring even more exciting mathematical topics to be explored in the years to come.

ACKNOWLEDGMENTS

This work was supported in part by the French Ministry of Research through Grant ACI/NIM/TRC-2004 (for T. T. Truong and M. K. Nguyen) and by the Swiss National Science Foundation under Grant SNSF 3100AD-116547 (for H. Zaidi)

REFERENCES

- [1] F. Natterer, *The Mathematics of Computerized Tomography*, Classics in Applied Mathematics, SIAM, Philadelphia, Pa, USA, 2001.
- [2] A. M. Cormack, "My connection with the Radon transform," in *75 Years of Radon Transform*, S. Gindikin and P. Michor, Eds., vol. 4 of *Conference Proceedings and Lecture Notes in Mathematical Physics*, pp. 32–35, International Press, Boston, Mass, USA, 1994.
- [3] A. M. Cormack, "Representation of a function by its line integrals, with some radiological applications," *Journal of Applied Physics*, vol. 34, no. 9, pp. 2722–2727, 1963.
- [4] A. M. Cormack, "Representation of a Function by Its Line Integrals, with Some Radiological Applications. II," *Journal of Applied Physics*, vol. 35, no. 10, pp. 2908–2913, 1964.
- [5] J. Radon, "Über die Bestimmung von Funktionen durch ihre Integralwerte längs gewisser Mannigfaltigkeiten," *Berichte über die Verhandlungen der Sächsischen Akademie der Wissenschaften zu Leipzig, Mathematisch-Naturwissenschaftliche Klasse*, vol. 69, pp. 262–277, 1917.
- [6] P. Grangeat, "Mathematical framework of cone beam 3D reconstruction via the first derivative of the Radon transform," in *Mathematical Methods in Tomography*, G. T. Herman, A. K. Louis, and F. Natterer, Eds., vol. 1497 of *Lecture Notes in Mathematics*, pp. 66–97, Springer, New York, NY, USA, 1991.
- [7] I. M. Gelfand, M. I. Graev, and N. Y. Vilenkin, *Generalized Functions V*, Academic Press, New York, NY, USA, 1965.
- [8] F. Natterer, "Inversion of the attenuated Radon transform," *Inverse Problems*, vol. 17, no. 1, pp. 113–119, 2001.
- [9] R. G. Novikov, "Une formule d'inversion pour la transformation d'un rayonnement X atténué," *Comptes Rendus l'Académie des Sciences*, vol. 332, pp. 1059–1063, 2001.
- [10] R. H. Morgan, "An analysis of the physical factors controlling the diagnostic," *American Journal of Roentgenology*, vol. 55, pp. 67–89, 1946.
- [11] M. K. Nguyen, C. Faye, L. Eglin, and T. T. Truong, "Apparent image formation by Compton-scattered photons in gamma-ray imaging," *IEEE Signal Processing Letters*, vol. 8, no. 9, pp. 248–251, 2001.
- [12] M. K. Nguyen and T. T. Truong, "On an integral transform and its inverse in nuclear imaging," *Inverse Problems*, vol. 18, no. 1, pp. 265–277, 2002.
- [13] R. W. Todd, J. M. Nightingale, and D. B. Everett, "A proposed γ camera," *Nature*, vol. 251, no. 5471, pp. 132–134, 1974.
- [14] D. B. Everett, J. S. Fleming, R. W. Todd, and J. M. Nightingale, "Gamma-radiation imaging system based on the Compton effect," *Proceedings of the Institution of Electrical Engineers*, vol. 124, no. 11, pp. 995–1000, 1977.
- [15] M. Singh, "An electronically collimated gamma camera for single photon emission computed tomography—part 1: theoretical considerations and design criteria," *Medical Physics*, vol. 10, no. 4, pp. 421–427, 1983.
- [16] H. Zaidi, "Relevance of accurate Monte Carlo modeling in nuclear medical imaging," *Medical Physics*, vol. 26, no. 4, pp. 574–608, 1999.
- [17] A. M. Cormack, "A paraboloidal Radon transform," in *75 Years of Radon Transform*, S. Gindikin and P. Michor, Eds., vol. 4 of *Conference Proceedings and Lecture Notes in Mathematical Physics*, pp. 105–109, International Press, Boston, Mass, USA, 1994.
- [18] A. M. Cormack and E. T. Quinto, "A Radon transform on spheres through the origin in R^n and applications to the Darboux equation," *Transactions of the American Mathematical Society*, vol. 260, no. 2, pp. 575–581, 1980.
- [19] A. M. Cormack, "Radon's problem for some surfaces in R^n ," *Proceedings of the American Mathematical Society*, vol. 99, no. 2, pp. 305–312, 1987.
- [20] K. Denecker, J. Van Overloop, and F. Sommen, "The general quadratic Radon transform," *Inverse Problems*, vol. 14, no. 3, pp. 615–633, 1998.
- [21] P. C. Johns, R. J. Leclair, and M. P. Wismayer, "Medical X-ray imaging with scattered photons," in *Opto-Canada: SPIE Regional Meeting on Optoelectronics, Photonics, and Imaging SPIE TD01*, pp. 355–357, Ottawa, Canada, May 2002.
- [22] H. Zaidi and B. H. Hasegawa, "Determination of the attenuation map in emission tomography," *Journal of Nuclear Medicine*, vol. 44, no. 2, pp. 291–315, 2003.
- [23] H. Zaidi and K. F. Koral, "Scatter modelling and compensation in emission tomography," *European Journal of Nuclear Medicine and Molecular Imaging*, vol. 31, no. 5, pp. 761–782, 2004.
- [24] C. E. Floyd, R. J. Jaszczak, C. C. Harris, and R. E. Coleman, "Energy and spatial distribution of multiple order Compton scatter in SPECT: a Monte Carlo investigation," *Physics in Medicine and Biology*, vol. 29, no. 10, pp. 1217–1230, 1984.
- [25] A. Erdélyi, W. Magnus, F. Oberhettinger, and F. G. Tricomi, *Higher Transcendental Functions II*, R. E. Krieger, Malabar, Fla, USA, 1981.
- [26] M. J. Yaffe and P. C. Johns, "Scattered radiation in diagnostic radiology: magnitudes, effects, and methods of reduction," *Journal of Applied Photographic Engineering*, vol. 9, no. 6, pp. 184–195, 1983.
- [27] A. H. Compton, "A quantum theory of the scattering of X-rays by light elements," *Physical Review*, vol. 21, no. 5, pp. 483–502, 1923.
- [28] H. H. Barrett, "The Radon transform and its applications," in *Progress in Optics*, E. Wolf, Ed., vol. 21, pp. 219–286, North Holland, Amsterdam, The Netherlands, 1984.

- [29] O. Klein and T. Nishina, "Über die Streuung von Strahlung durch freie Elektronen nach der neuen relativistischen Quantendynamik von Dirac," *Zeitschrift für Physik*, vol. 52, no. 11-12, pp. 853–868, 1929.
- [30] M. K. Nguyen, T. T. Truong, H. D. Bui, and J. L. Delarbre, "A novel inverse problem in γ -rays emission imaging," *Inverse Problems in Science and Engineering*, vol. 12, no. 2, pp. 225–246, 2004.
- [31] M. K. Nguyen, T. T. Truong, and P. Grangeat, "Radon transforms on a class of cones with fixed axis direction," *Journal of Physics A: Mathematical and General*, vol. 38, no. 37, pp. 8003–8015, 2005.
- [32] M. Singh and D. Doria, "An electronically collimated gamma camera for single photon emission computed tomography—part 2: image reconstruction and preliminary experimental measurements," *Medical Physics*, vol. 10, no. 4, pp. 428–435, 1983.
- [33] M. J. Cree and P. J. Bones, "Towards direct reconstruction from a gamma camera based on Compton scattering," *IEEE Transactions on Medical Imaging*, vol. 13, no. 2, pp. 398–407, 1994.
- [34] R. Basko, G. L. Zeng, and G. T. Gullberg, "Application of spherical harmonics to image reconstruction for the Compton camera," *Physics in Medicine and Biology*, vol. 43, no. 4, pp. 887–894, 1998.
- [35] L. C. Parra, "Reconstruction of cone-beam projections from Compton scattered data," *IEEE Transactions on Nuclear Science*, vol. 47, no. 4, part 2, pp. 1543–1550, 2000.
- [36] J. Pauli, E.-M. Pauli, and G. Anton, "ITEM—QM solutions for EM problems in image reconstruction exemplary for the Compton camera," *Nuclear Instruments and Methods in Physics Research A: Accelerators, Spectrometers, Detectors and Associated Equipment*, vol. 488, no. 1-2, pp. 323–331, 2002.
- [37] M. Hirasawa, T. Tomitani, and S. Shibata, "New analytical method for three dimensional image reconstruction in multitracer gamma-ray emission imaging; Compton camera for multitracer," *RIKEN Review*, no. 35, pp. 118–119, 2001.
- [38] T. Tomitani and M. Hirasawa, "Image reconstruction from limited angle Compton camera data," *Physics in Medicine and Biology*, vol. 47, no. 12, pp. 2129–2145, 2002.
- [39] M. Hirasawa and T. Tomitani, "An analytical image reconstruction algorithm to compensate for scattering angle broadening in Compton cameras," *Physics in Medicine and Biology*, vol. 48, no. 8, pp. 1009–1026, 2003.
- [40] J. D. Jackson, *Classical Electrodynamics*, John Wiley & Sons, New York, NY, USA, 3rd edition, 1999.
- [41] S. R. Deans, "A unified Radon inversion formula," *Journal of Mathematical Physics*, vol. 19, no. 11, pp. 2346–2349, 1978.
- [42] S. Helgason, *The Radon Transform*, Birkhäuser, Boston, Mass, USA, 1999.
- [43] G. Beylkin, "The inversion problem and applications of the generalized Radon transform," *Communications on Pure and Applied Mathematics*, vol. 37, no. 5, pp. 579–599, 1984.
- [44] G. Beylkin, "Inversion and applications of the generalized Radon transform," in *75 Years of Radon Transform*, S. Gindikin and P. Michor, Eds., vol. 4 of *Conference Proceedings and Lecture Notes in Mathematical Physics*, pp. 71–79, International Press, Boston, Mass, USA, 1994.

Research Article

Level Set Method for Positron Emission Tomography

Tony F. Chan,¹ Hongwei Li,² Marius Lysaker,³ and Xue-Cheng Tai^{4,5}

¹Department of Mathematics, University of California, Los Angeles, 405 Hilgard Avenue, Los Angeles, CA 90095-1555, USA

²Center for Integrated Petroleum Research, University of Bergen, CIPR room 4103, Allégaten 41, 5007 Bergen, Norway

³Department of Scientific Computing, Simula Research Laboratory AS, 1325 Lysaker, Norway

⁴Department of Mathematics and System Sciences, Henan University, Kaifeng 475001, China

⁵Department of Mathematics, University of Bergen, Johannes Brunsgate 12, 5009 Bergen, Norway

Received 26 December 2006; Accepted 6 May 2007

Recommended by Hongkai Zhao

In positron emission tomography (PET), a radioactive compound is injected into the body to promote a tissue-dependent emission rate. Expectation maximization (EM) reconstruction algorithms are iterative techniques which estimate the concentration coefficients that provide the best fitted solution, for example, a maximum likelihood estimate. In this paper, we combine the EM algorithm with a level set approach. The level set method is used to capture the coarse scale information and the discontinuities of the concentration coefficients. An intrinsic advantage of the level set formulation is that anatomical information can be efficiently incorporated and used in an easy and natural way. We utilize a multiple level set formulation to represent the geometry of the objects in the scene. The proposed algorithm can be applied to any PET configuration, without major modifications.

Copyright © 2007 Tony F. Chan et al. This is an open access article distributed under the Creative Commons Attribution License, which permits unrestricted use, distribution, and reproduction in any medium, provided the original work is properly cited.

1. INTRODUCTION

One of the most important quality of PET is its abilities to model biological and physiological functions in vivo to enhance our understanding of the biochemical basis of normal and abnormal functions within the body. PET is also useful for the detection of cancer, coronary artery disease, and brain disease. During a PET acquisition, a compound containing a radiative isotope is injected into the body to form an (unknown) emission density $\lambda(x, y) \geq 0$. The positron emitted finds a nearby electron and they annihilate into two photons of 511 keV according to the equation $E = mc^2$. This energy is strong enough to escape the body. Since the two photons travel at almost opposite directions, a detector ring surrounds the patient and tries to collect the emissions. For an emission event to be counted, both photons must be registered nearly simultaneously at two opposite detectors. In Figure 1, emission paths from two different regions are shown, that is, along the tube covered by detector pair AD, and along the tube covered by detector pair BC. Regions with higher concentration of radioactivity cause a higher emission rate. Given the total number of measured counts for each detector pair, the challenge is to locate all the emission sources inside the detector ring. Emissions measured between two detectors could have taken place

anywhere along the tube between these two detectors, but with a systematic inspection of all detector pairs, it is possible to reveal variance in the emission rate along the same tube.

Detection of the radioactive concentration in different tissues gives useful information both for research and clinical purposes. This information is often analyzed and visualized as an image. Unfortunately, the measured events also include noise such as accidental coincidences that complicate the image reconstruction. The Fourier-based filtered back-projection [1] algorithm is a well-established construction technique. This algorithm is computationally efficient, but the drawbacks are constructions with low signal-to-noise ratio and low resolution. Iterative methods to construct PET images have been an attractive approach during the last two decades. Most of these methods are based on maximum likelihood estimates. Due to the inherent ill-posedness of this inverse problem, the reconstruction process suffers from noise and edge artifacts, see [2, 3] for related problems. It is well known that the standard EM algorithm [4–6] converges toward a noisy image and it is necessary to terminate the iteration before the noise becomes too dominant [7]. If the iteration stops too early, important information could be lost. A general approach to address these problems is to utilize a regularization term according to certain a priori assumptions

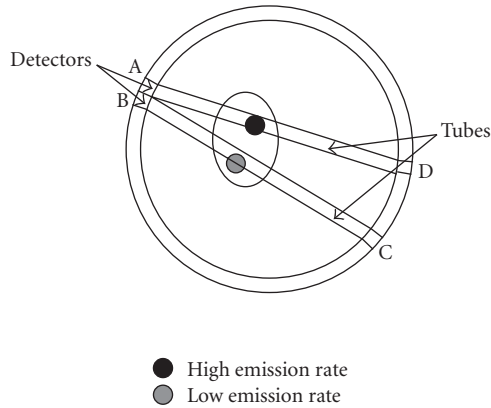


FIGURE 1: Gamma rays escape the body and are observed by the detectors.

of the desired image [8–10]. Results with deviation from these assumptions will be penalized. For example, information from surrounding pixels can reveal irregularities and remove outsiders. The total variation (TV) minimization has been successfully used in many image processing applications [11–17]. In [18], the standard EM algorithm for PET was modified to incorporate the TV regularization. The blurring effect was subdued by using this approach, but improvements are still needed.

Common for the iterative methods mentioned above is that they estimate the concentration coefficients that provide the best fitted solution based on a maximum likelihood estimate. In PET, different tissues should have different active levels, while the active values should change smoothly and slowly in the same tissue [19]. So, the PET image is actually a piecewise smooth function [20]. Recently, PET has been combined with CT and MRI devices [21–24]. CT and MRI can provide high-resolution structural information, which can be incorporated into the reconstruction process to improve the properties of the constructed PET image. Usually the anatomical information obtained from CT or MRI image is used as a Bayesian prior. A penalty technique is utilized to build in the Bayesian prior, while a parameter β to control the strength of the penalty. However, this approach is very sensitive to the penalty parameter, and finding a proper β can be challenging. In this paper, we use a level set method to serve this purpose. We reduce the set of possible solutions by estimating the emission rate as a piecewise constant function. This can be thought of as an approximation to the piecewise smooth image. By this way, the anatomical information based on CT or MRI can be used as the initial guess for the level set curves, without the need to estimate the penalty parameter β . We can see in the numerical experiment section that the quality of the reconstruction improves with the quality of the anatomical data.

Level set method is a versatile tool which has been applied to many areas of computational mathematics [25–29]. As in many other applications, the level set method is used here to capture the coarse scale information and the discontinuities of the function to be recovered. By incorporating

the level set method into the image reconstruction, sharp boundaries between different tissues are directly obtained for PET images. This variant of the EM algorithm (called LSEM hereafter) can be applied to any PET configuration, without major modifications. We will first show that even without anatomical information available, LSEM can produce better images than EM algorithm in some sense. Moreover, LSEM can easily and naturally incorporate anatomical information (interior boundaries for different tissues, which can be obtained from CT or MRI images), and improve the quality of the reconstructed images further. It is well known that one drawback of the EM algorithm is its lack of stopping criterion. In this paper, TV regularization will be used to deal with the ill-posedness of the reconstruction process. The parameter used to weight the influence of the TV regularization more explicitly controls the tradeoff between regularity and fitting the data. There is a number of well-known techniques for choosing this parameter more systematically [18, page 6].

Geometric curve-evolution techniques for tomographic reconstruction problems have been proposed previously, see [19, 30–37] and the references therein. Similar to [31], we assume the object intensity values to be piecewise constant, but we allow for multiple object regions as in [19]. Due to the piecewise constant intensity value restriction, our cost functional is simpler than the one proposed in [19]. In [36, 37], a strategy for joint estimation of the unknown region boundaries and the unknown activity levels was developed. However, the movement of the parameterized boundaries involved only translation, rotation, and scaling. We propose a more flexible framework here, and allow multiple object regions. In addition, level set method is more flexible and efficient in dealing with complicated geometries, thanks to its great ability to handle topological changes during the curve evolution. In [38], the authors proposed a piecewise smooth model for emission tomography reconstruction, which also utilized the level set framework. Compared to that model, our piecewise constant model is simpler, and can simplify the computations. We would like to emphasize that in most cases, our method could still work well even if the intensity function is not piecewise constant. In fact, our method just needs that the object in the scene can be well segmented into several phases. We will show some results in the numerical experiment section to verify it.

The remainder of this paper is organized in the following way. In Section 2, we summarize the theory behind the EM approach and introduce some specific notations used throughout this paper. Partial differential equation techniques have been successfully used in many image processing applications, and a predecessor for our approach is given in Section 3. In Section 4, we explain the main idea behind the level set method and demonstrate that level set functions can be used to represent general piecewise constant functions [29, 39, 40]. Motivated by this, we utilize a level set formulation to represent PET images with piecewise constant emission densities in Section 5. In this section, we also give implementation details. Finally, we report some numerical results in Section 6.

TABLE 1: Notations used throughout this paper.

b	Pixel index $(1, 2, \dots, B)$
λ_b	Unknown source intensity at a pixel b , $\lambda_b \geq 0$ for all b
t	Detector pair index $(1, 2, \dots, T)$
n_t	Total number of coincidences counted by detector pair t , $n_t \geq 0$ for all t
P_{tb}	Probability for an emission from b to be detected in t

2. MAXIMUM LIKELIHOOD EXPECTATION MAXIMIZATION

From the measured emission an image can be constructed by the EM algorithm [5, 6]. This algorithm provides an iterative formula to construct an image which makes the measured data most likely to occur. Given an image, the aim is to maximize the conditional probability of the data by using a likelihood function (and later we will also use a log-likelihood function):

$$l(\lambda) = f(\text{data} | \lambda) \quad \text{or} \quad l_{\log}(\lambda) = \log(l(\lambda)). \quad (1)$$

Here, data are the measured counts in the detector ring, $\lambda : \Omega \rightarrow \mathbb{R}$ is the unknown emission rate causing these counts, and Ω is the image domain. The region to be reconstructed is usually covered by a uniform mesh, where each square in the mesh corresponds to one pixel in the PET image. The discrete representation of λ and other essential notations for describing the EM image reconstruction model are listed in Table 1. To simplify the notations, we still use λ to denote its discretized version, for example, $\lambda = (\lambda_1, \lambda_2, \dots, \lambda_B)^T$.

Each element P_{tb} in matrix P describes the probability for an annihilation event that occurred in the area of the source covered by pixel b to be detected by detector pair t . Several physical factors such as attenuation, scatter and accidental coincidence corrections, time-of-flight, positron range and angulation information, and so forth, can be incorporated in the probability matrix P . To compute P_{tb} , the angle-of-view method was chosen in this paper, but other methods can also be used [41, 42]. By the angle-of-view method, each element P_{tb} in the probability matrix P is approximated by the largest angle (in fraction of π) completely contained within tube t as seen from the center of b . For details about the angle-of-view, see the paper of Shepp and Vardi [6]. The intensity value λ_b is the information we are seeking since it is related to the tracer concentration. During the acquisition process, a random number of emissions is generated from a Poisson distribution. A nonnegative, integer-valued, and random variable Z follows a Poisson distribution if

$$\text{Poisson}(Z = k) = e^{-\sigma} \frac{\sigma^k}{k!}, \quad (2)$$

where $\sigma > 0$ and Z has mean $E(Z) = \sigma$. The Poisson distribution is applicable to many problems involving random events, such as particles leaving a fixed point at a random angle. For the moment, we focus on one of the tubes in Figure 1 and assume that this tube corresponds to the region covered

by detector pair $t = 1$. Given the mean $(P\lambda)_1$, we want to maximize the probability for $(P\lambda)_1$ to fit the measured data n_1 :

$$\text{Poisson}(Z = n_1) = e^{-(P\lambda)_1} \frac{(P\lambda)_1^{n_1}}{n_1!}, \quad (3)$$

where a maximum is obtained for $n_1 = (P\lambda)_1$, and similarly the maximum is achieved for $n_2 = (P\lambda)_2$ if we focus on region covered by detector pair $t = 2$. The measured coincidence events also include scattered and accidental coincidences. Some events produced inside the source pass are undetected because of tissue attenuation or photon travelling path that does not intersect the detector ring. This complicates the image construction. However, each n_t is distributed according to a Poisson distribution and since all measurements are independent of each other, the likelihood over all projections reduces to the product of the separate projections likelihood [5]. Therefore we want to maximize

$$l(\lambda) = \prod_{t=1}^T e^{-(P\lambda)_t} \frac{(P\lambda)_t^{n_t}}{n_t!}. \quad (4)$$

To simplify the calculation, the log-likelihood function is employed to convert (4) to the form

$$\begin{aligned} l_{\log}(\lambda) &= \sum_{t=1}^T [\log e^{-(P\lambda)_t} + \log (P\lambda)_t^{n_t} - \log (n_t!)] \\ &= - \sum_{b=1}^B \lambda_b + \sum_{t=1}^T n_t \log (P\lambda)_t + K. \end{aligned} \quad (5)$$

In (5), we assume

$$\sum_{t=1}^T P_{tb} = 1 \quad (6)$$

for any pixel b , and then exploit the conversions

$$\sum_{t=1}^T (P\lambda)_t = \sum_{b=1}^B \lambda_b, \quad - \sum_{t=1}^T \log (n_t!) \stackrel{\text{def.}}{=} K. \quad (7)$$

Since K is independent of λ , this constant will be ignored. Maximizing $l_{\log}(\lambda)$ with respect to λ will provide us with the best estimate of λ in a statistical sense. The optimization problem can be rewritten by $\max l_{\log}(\lambda) = \min(-l_{\log}(\lambda))$, and thereupon a mathematical formulation of PET becomes

$$\min_{\lambda} F(\lambda) = \min_{\lambda} \left(\sum_{b=1}^B \lambda_b - \sum_{t=1}^T n_t \log (P\lambda)_t + V(\lambda) \right), \quad (8)$$

where $V(\lambda)$ is a regularization term introduced to improve image quality [7–10, 18, 43]. Several regularization methods tend to blur edges because both noise and edges contribute to inhomogeneous behavior. To subdue the blurring effect, the total variation norm of λ was introduced as a regularization term in [18]. In the next section, we give a short overview of the TV-based EM algorithm.

3. A TOTAL VARIATION-BASED EM ALGORITHM

In [18], an algorithm was designed to find the pointwise values of λ . The authors covered the domain Ω with a uniform mesh, where each square in the mesh corresponds to one pixel in the PET image. The emission density function λ is represented by a piecewise linear function or piecewise constant function where λ takes value λ_b at pixel b , $b = 1, 2, \dots, B$. In order to regularize the problem, they find a minimizer for the following functional:

$$L(\lambda) = \mu \int_{\Omega} |\nabla \lambda| dx + \left(\sum_{b=1}^B \lambda_b - \sum_{t=1}^T n_t \log(P\lambda)_t \right). \quad (9)$$

From (9), it is easy to see that

$$\frac{\partial L}{\partial \lambda} = \mu C(\lambda)\lambda + \vec{e} - P^t(\vec{n}/P\lambda). \quad (10)$$

In the above, $C(\lambda)$ is a matrix depending on λ , \vec{e} is the vector with unit entries, P^t is the transpose of the matrix P , and $\vec{n}/P\lambda$ is the elementwise division of vector \vec{n} by vector $P\lambda$. In [18], the following fixed point iteration was used for finding the minimizer of (9):

$$\lambda^{k+1} = [\mu C(\lambda^k) + \text{diag}(1./\lambda^k)]^{-1} P^t(\vec{n}/P\lambda^k). \quad (11)$$

In (11), $\text{diag}(1./\lambda^k)$ is the matrix with $1./\lambda^k$ on its diagonal and $C(\lambda^k)$ is a finite difference approximation for $-\nabla \cdot (\nabla \lambda^k / |\nabla \lambda^k|)$. This scheme is obtained from (10), by replacing \vec{e} by λ^{k+1}/λ^k . In (11), if let $\mu = 0$, we get the classical EM algorithm. This algorithm finds all the pixel values λ_b . In practice, we know that λ should be a piecewise smooth (piecewise constant) function in PET images. However, this information is not fully utilized in the above algorithm. Below we demonstrate that such information can be incorporated and handled in an efficient way by using the level set framework, which can help to produce images with sharper edges. See also [19, 29, 30, 32–35, 40, 44] for other applications where level set based ideas are used to identify piecewise constant functions.

4. AN INTRODUCTION TO THE LEVEL SET METHOD

The level set method was proposed by Osher and Sethian [25] for tracing interfaces between different phases of fluid flows. Later, it has been used in many applications involving movement of interfaces for different kinds of physical problems [26–28]. In the following, we will present a “unified” framework, first presented in [29, 39, 40, 45], of using multiple level sets to represent piecewise constant functions.

Let Γ be a closed curve in $\Omega \subset \mathbb{R}^2$. Associated with Γ , we define a ϕ as the signed distance function:

$$\phi(x) = \begin{cases} \text{distance}(\mathbf{x}, \Gamma), & \mathbf{x} \in \text{interior of } \Gamma, \\ -\text{distance}(\mathbf{x}, \Gamma), & \mathbf{x} \in \text{exterior of } \Gamma, \end{cases} \quad (12)$$

where \mathbf{x} denotes (x, y) . It is clear that Γ is the zero level set of the function ϕ . In the case that Γ is not closed, but divides the

domain into two parts, the level set function can be defined to be positive on one side of the curve and negative on the other side of the curve.

Once the level set function is defined, we can use it to represent general piecewise constant functions. For example, assuming that $\lambda(x, y)$ equals c_1 inside Γ and equals c_2 outside Γ , it is easy to see that λ can be represented as

$$\lambda = c_1 H(\phi) + c_2 (1 - H(\phi)), \quad (13)$$

where the Heaviside function $H(\phi)$ is defined by

$$H(\phi) = \begin{cases} 1, & \phi > 0, \\ 0, & \phi \leq 0. \end{cases} \quad (14)$$

In order to identify the piecewise constant function λ , we need to identify the level set function ϕ and the constants c_i , $i = 1, 2$.

If the function $\lambda(x, y)$ has many pieces, we need to use multiple level set functions. We follow the ideas of [29, 39, 40, 46]. Assume that we have two closed curves Γ_1 and Γ_2 , and we associate the two level set functions ϕ_j , $j = 1, 2$ with these curves. The domain Ω can now be divided into four parts:

$$\begin{aligned} \Omega_1 &= \{\mathbf{x} \in \Omega, \phi_1 > 0, \phi_2 > 0\}, \\ \Omega_2 &= \{\mathbf{x} \in \Omega, \phi_1 > 0, \phi_2 < 0\}, \\ \Omega_3 &= \{\mathbf{x} \in \Omega, \phi_1 < 0, \phi_2 > 0\}, \\ \Omega_4 &= \{\mathbf{x} \in \Omega, \phi_1 < 0, \phi_2 < 0\}. \end{aligned} \quad (15)$$

Using the Heaviside function again, the following formula can be used to express a piecewise constant λ with up to four constant values:

$$\begin{aligned} \lambda &= c_1 H(\phi_1) H(\phi_2) + c_2 H(\phi_1) (1 - H(\phi_2)) \\ &\quad + c_3 (1 - H(\phi_1)) H(\phi_2) + c_4 (1 - H(\phi_1)) (1 - H(\phi_2)). \end{aligned} \quad (16)$$

By generalizing, we see that n level set functions give the possibility of 2^n regions. For $i = 1, 2, \dots, 2^n$, let

$$\text{bin}(i-1) = (b_1^i, b_2^i, \dots, b_n^i) \quad (17)$$

be the binary representation of $i-1$, where $b_j^i = 0$ or 1. A piecewise constant function λ with constant coefficients c_i , $i = 1, 2, \dots, 2^n$, can be represented as (cf. [29, 40])

$$\lambda = \sum_{i=1}^{2^n} c_i \prod_{j=1}^n R_i(\phi_j), \quad (18)$$

where

$$R_i(\phi_j) = \begin{cases} H(\phi_j), & \text{if } b_j^i = 0, \\ 1 - H(\phi_j), & \text{if } b_j^i = 1. \end{cases} \quad (19)$$

Even if the true λ needs less than 2^n distinct regions, we can still use n level set functions since some subdomains are allowed to be empty. Using such a representation, we only need to determine the maximum number of level set functions that should be utilized.

5. A LEVEL SET EM ALGORITHM (LSEM)

In this section, we will use the level set idea to represent λ as a function that only takes a limited number of constant values. Assume that the domain Ω can be divided into a union of subregions such that all λ_b have the same constant intensity value in each of the subregions. For such a case, we can use level set functions to express $\lambda = \lambda(\phi)$ as in (18). Concerning the optimization problem, we utilize the fact that calculations from (10) can be carried forward by the chain rule for $\lambda(\phi)$. As the λ function is already discretized, we will also use discretized level set functions ϕ_j , $j = 1, 2, \dots, n$. From the chain rule, see [29], we get

$$\begin{aligned} \frac{\partial L}{\partial \phi_j} &= \frac{\partial L}{\partial \lambda} \frac{\partial \lambda}{\partial \phi_j}, \\ \frac{\partial L}{\partial c_j} &= \int_{\Omega} \frac{\partial L}{\partial \lambda} \frac{\partial \lambda}{\partial c_j}. \end{aligned} \quad (20)$$

The calculation of $\partial L / \partial \lambda$ is given in (10). We only need to have $\partial \lambda / \partial \phi_j$ in order to get $\partial L / \partial \phi_j$. If λ takes only two constant values c_1 and c_2 as in (13), it is easy to see that

$$\frac{\partial \lambda}{\partial \phi} = (c_1 - c_2) \delta(\phi), \quad (21)$$

where the delta function $\delta(\phi) = H'(\phi)$. In case that we need two level set functions ϕ_1 and ϕ_2 , it follows from (16) that

$$\begin{aligned} \frac{\partial \lambda}{\partial \phi_1} &= ((c_1 - c_2 - c_3 + c_4)H(\phi_2) + c_2 - c_4)\delta(\phi_1), \\ \frac{\partial \lambda}{\partial \phi_2} &= ((c_1 - c_2 - c_3 + c_4)H(\phi_1) + c_3 - c_4)\delta(\phi_2). \end{aligned} \quad (22)$$

The calculation of $\partial \lambda / \partial c_j$, $j = 1, 2, \dots, n$, is straightforward.

For level set methods, it is standard to use the length of the level set curves as the regularization term (cf. [39, 46]). So we replace the regularization term $\alpha \int_{\Omega} |\nabla \lambda| dx$ in (9) by the length term $\alpha \sum_{j=1}^n \int_{\Omega} |\nabla H(\phi_j)| dx$, and its derivative with respect to ϕ_j is the curvature $-\alpha \nabla \cdot (\nabla \phi_j / |\nabla \phi_j|) \delta(\phi_j)$, where α is a parameter to be used to control the influence of the regularization. Once the gradient $\partial L / \partial \phi_j$ is available, we can use the following gradient method (Algorithm 1 below) to find a minimizer for the optimization problem.

Algorithm 1 (level set EM algorithm).

- (i) Choose initial values for ϕ_j^0 and the time step Δt_j^0 .
- (ii) For all the level set functions ϕ_j , update the functions

$$\phi_j^{n+1} = \phi_j^n - \Delta t_j^n \frac{\partial L}{\partial \phi_j}(\phi_j^n). \quad (23)$$

- (iii) Update the constants c_j :

$$c_j^{n+1} = c_j^n - \theta_j \frac{\partial L}{\partial c_j}. \quad (24)$$

- (iv) Reinitialize the level set functions ϕ_j if a “sufficient” amount of pixel values of ϕ_j have changed sign. Otherwise, go to the next iteration.

Some remarks about the implementation of the algorithm are given as follows:

(i) We are restricting the class of solutions to piecewise constant functions represented by (16).

(ii) All the step length parameters can be determined by trial and error or by using a line search method to get the optimal ones.

(iii) The parameter α weights the influence of the regularization. An oscillatory curve may occur if α is too small, and α too large will deny a proper evolution of the curve. By trial and error $\alpha \in (10^{-3}, 10^{-4})$ was found to be a proper choice for the class of PET images used in our experiments.

(iv) For numerical purpose, we approximate the delta function and the Heaviside function by

$$\delta_{\epsilon_1}(\phi_j) = \frac{\epsilon_1}{\pi(\phi_j^2 + \epsilon_1^2)}, \quad H_{\epsilon_2}(\phi_j) = \frac{1}{\pi} \tan^{-1} \frac{\phi}{\epsilon_2} + \frac{1}{2}. \quad (25)$$

This is also standard for level set methods [39]. In our numerical examples, we found that $\epsilon_1 = 0.5h$ and $\epsilon_2 = 0.005h$ worked well, where h refers to the grid size.

(v) There are efficient numerical methods to reinitialize the level set functions, see [26, 28, 47] for details. The numerical method we have used for the reinitialization is as in [40, 47], and we reinitialize the level set functions for each 30 iterations.

(vi) We do not update the constants for every iteration, updating once for each 5–10 iterations is sufficient.

(vii) Our approach allows the use of prior knowledge about the constants (active levels) to improve the quality of the reconstruction. We found that a reasonable estimate for these constants could help to improve the convergence of the algorithm. In all numerical implementations, an interval $[a_j, b_j]$ is chosen for each of the constants c_j , $j = 1, 2, 3$. We assume that the minimizer for c_j is inside $[a_j, b_j]$. During the iterations, we project c_j into the interval by setting $c_j = \min(\max(a_j, c_j), b_j)$.

6. NUMERICAL RESULTS

In this section, we report some numerical results. The EM algorithm and TV-EM algorithm are implemented and will be compared with the results achieved by our LSEM algorithm. In all the examples, the observation vectors (sinogram data) were constructed by forward projection, then scaled up to total 2×10^6 counts by multiplying a constant, corrupted with Poisson noise, and finally scaled back. To quantify the quality of the reconstructed images, we calculated the root mean square error (RMSE) for the reconstruction. RMSE is defined as

$$\text{RMSE} = \sqrt{\frac{\|\lambda - \hat{\lambda}\|_{\ell_2}^2}{n}}, \quad (26)$$

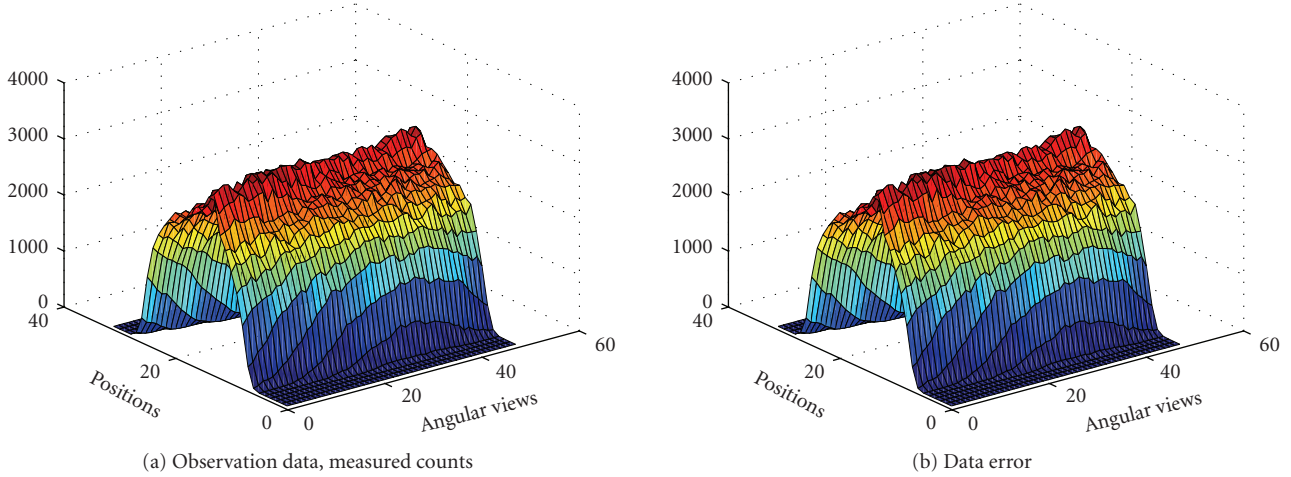


FIGURE 2: Sinogram data, obtained by forward projection: $n = P\lambda$ plus Poisson noise.

where λ and $\hat{\lambda}$ are two vectors that represent the computed image and the true image, respectively, and n is the number of pixels of the image.

6.1. Without prior information

In our first example we try to reconstruct a 32×32 image of two circles, one inside the other, as seen in Figure 3(e). Total 1536 (32 positions and 48 angular views) observations were given to us. The sinogram data as well as the data noise (after scaling up) are shown in Figure 2. The true intensity values are $\{0, 1, 2\}$. We first test the EM algorithm. After a few iterations, it is possible to see some inner structures in the PET image depicted in Figure 3.

The major drawback with the EM algorithm is its lack of termination criterion and the introduction of noise as the number of iterations increases. In Figure 3(b), the intensity values in the outer circle are almost constant (as it should be in this test), but it is difficult to decide the exact boundary for the inner circle. After 30 iterations, the edges are emphasized but so is the noise, as seen in Figure 3(c). After 100 iterations, the noise becomes dominant and degrades the quality of the recovered intensity function. The same sinogram data were thereafter used for the TV-EM and the LSEM algorithms. The results are shown in Figure 4. For the two level set functions of the LSEM algorithm, we started with random initial guesses (cf. Figures 4(a) and 4(e)).

In less than 200 iterations, both level set functions have converged to a constant shape and these level set functions together with (16) were used to get Figure 5(c). With two level set functions, we see from (15) that it is possible to identify up to 4 distinct regions. The true PET image depicted in Figure 5(d) consists of only 3 distinct regions: background, outer circle, and inner circle. To handle this, we put $c_1 = c_3$ such that 2 regions yield the same contribution to the constructed PET image. The intervals for the intensity values are $\{[0, 0.5], [0.5, 1.5], [1.5, 2.5]\}$. After 200 iterations, the intensity values are recovered as $\{0, 1.0005, 2.0192\}$, which match the true values very well.

Even though this is a simple test that involves a nonmedical image, it illustrates the potential in the LSEM algorithm. Sharp edges are recovered properly for the PET image and different regions do not suffer from inhomogeneities caused by noise. Notice the improvement of LSEM over EM and TV-EM in the recovery of the shape of the inner circle in Figure 5. The RMS error, as shown in Figure 5(e), also suggests that the LSEM algorithm produces the best reconstruction.

In the next example, the interior structure of the PET image is more complicated. We try to reconstruct a 32×32 image of the brain from 1536 observations (32 positions and 48 angular views, synthetic data). The sinogram data as well as the data noise (after scaling up) are shown in Figure 6. The true intensity values are $\{0, 1, 4\}$. The results obtained with the EM algorithm are displayed in Figure 7.

We also used the same sinogram data to test the TV-EM and the LSEM algorithms. For the LSEM algorithm, the evolutions of the two functions ϕ_1 and ϕ_2 are given in Figures 8 and 9, respectively.

In less than 600 iterations, the two level set functions have converged. Combining ϕ_1 from Figure 8(c) and ϕ_2 from Figure 9(c) together with (16), we get the PET image depicted in Figure 10(c). In this test, we used c_4 (background), c_2 (gray matter), and $c_1 = c_3$ (white matter). The intervals for the intensity values are: $\{[0, 0.5], [0.5, 1.5], [3.5, 4.5]\}$. After 600 iterations, the intensity values are recovered pretty well as $\{0, 0.9802, 4.0620\}$.

In Figures 10(a) and 10(b), the boundaries between the tissue classes are not sharp. In contrast, we see that LSEM algorithm is able to recover almost all the fine details in the PET image in this example.

Next, we challenge our algorithm with a 64×64 image obtained from a segmented MRI slice of the brain. This image was used to generate totally 6144 (64 positions and 96 angular views) observations. The sinogram data as well as the data noise (after scaling up) are shown in Figure 11. Notice that we are using the MRI image to generate the PET data,

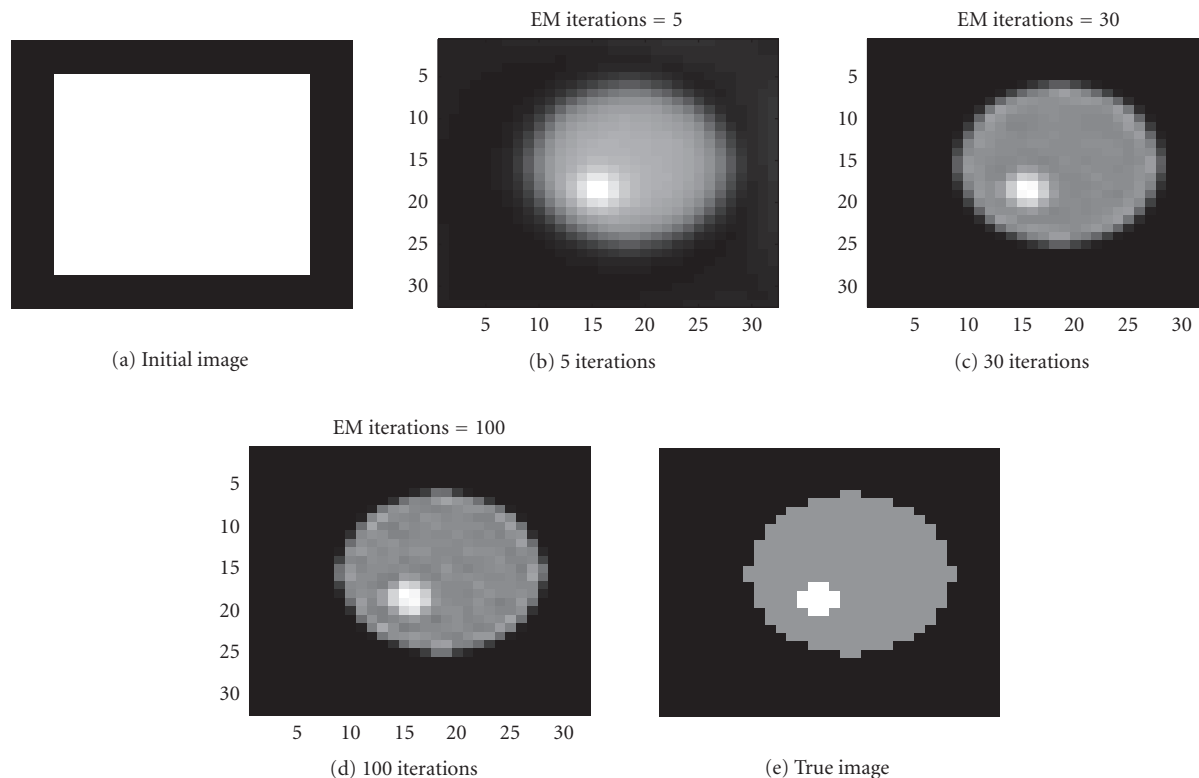


FIGURE 3: Evolution of a two circles using the EM algorithm.

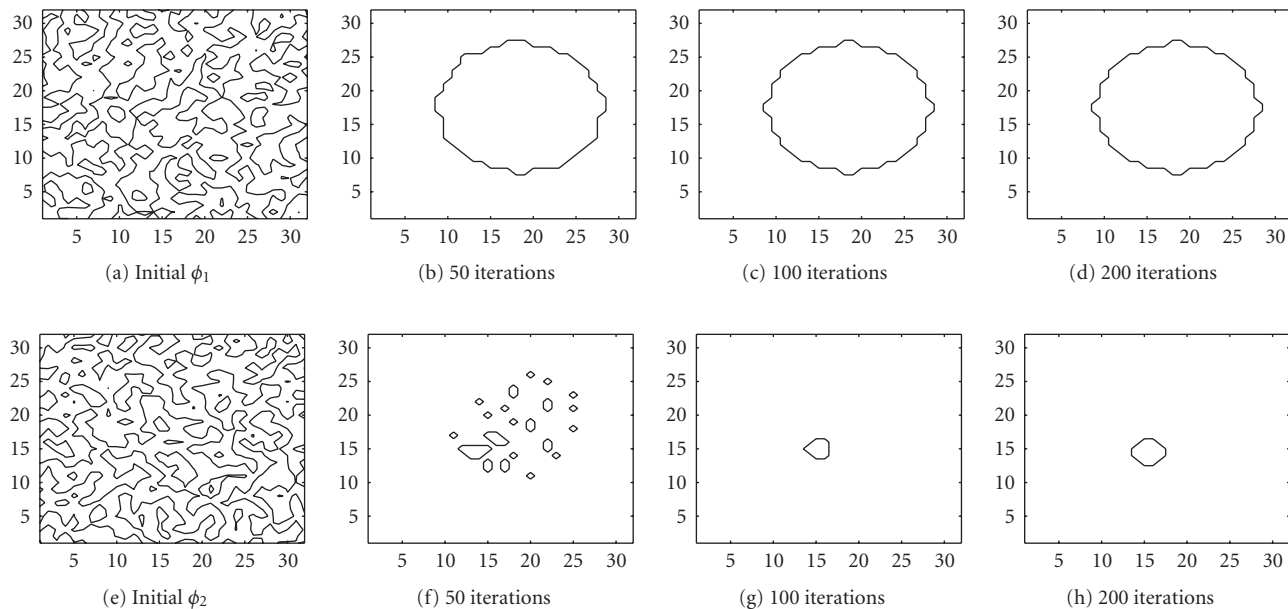


FIGURE 4: Interfaces given by the zero level set of the function ϕ_1 and ϕ_2 .

and we are not trying to solve the MRI tomography problem. The true intensity values are $\{0, 1, 4\}$, and the intervals $\{[0, 0.5], [0.5, 1.5], [3.5, 4.5]\}$ were used for our LSEM algorithm. Compared with Figures 5(c) and 10(c), the inner structure to be recovered here is more complicated, as seen

in Figure 14(c). The evolutions of the ϕ_1 and ϕ_2 functions are shown in Figures 12 and 13.

We see that the level set function ϕ_2 is recovered rather accurately, while the interior structure for ϕ_1 is not that nicely recovered. This will influence the appearance of the PET

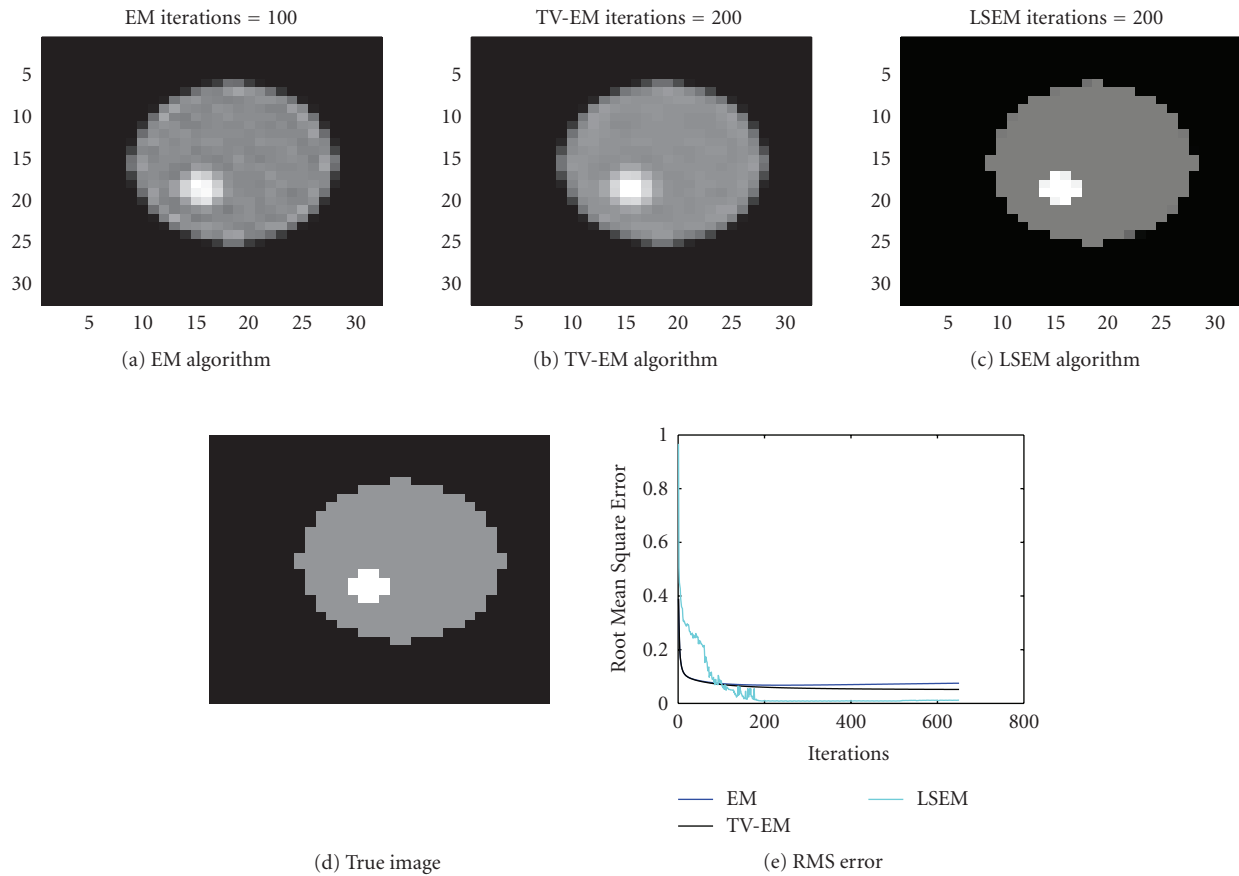


FIGURE 5: PET image of two circles constructed with different algorithms.

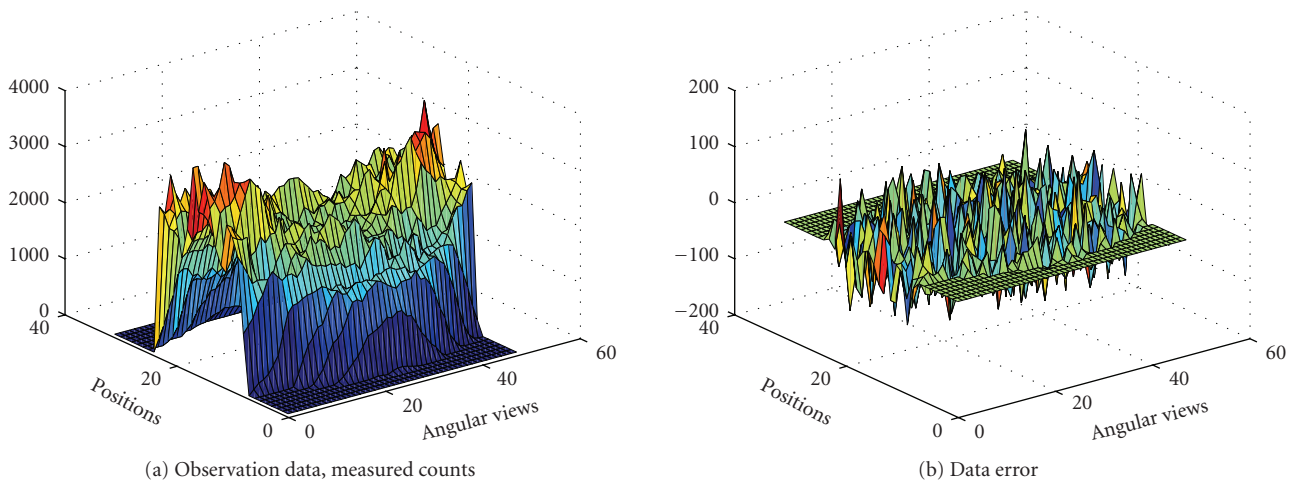


FIGURE 6: Sinogram data, obtained by forward projection: $n = P\lambda$ plus Poisson noise.

image, as seen in Figure 14(b). After 650 iterations, the intensity values are recovered as $\{0, 0.95549, 3.8629\}$. If we look at Figure 14(e), the RMS error does not reveal any advantages for the LSEM algorithm. Even so, due to the clearly iden-

tified dark region and the sharp edges in Figure 14(c), the LSEM algorithm still produces a better result than what was achieved with the EM algorithm in Figure 14(a) or TV-EM in Figure 14(b).

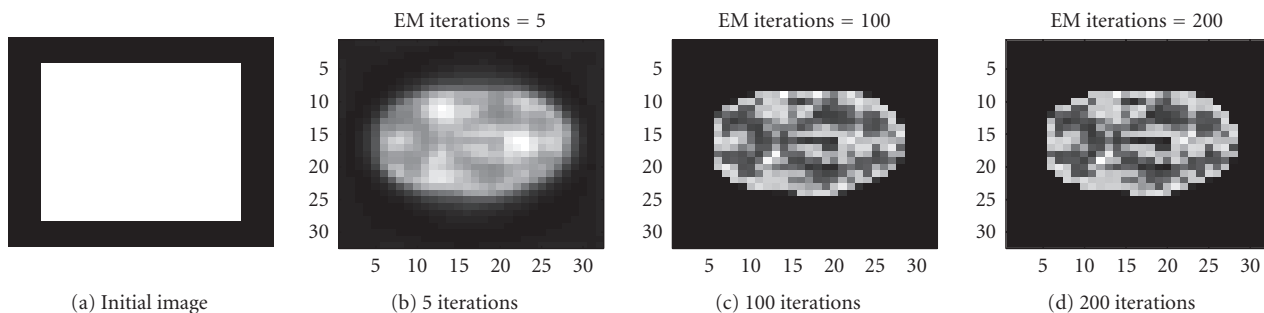


FIGURE 7: Evolution of a brain image with the EM algorithm.

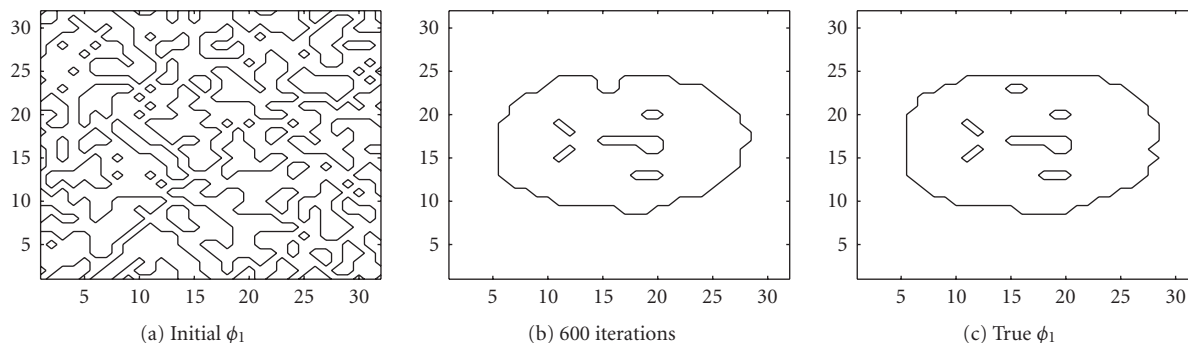


FIGURE 8: Interfaces given by the zero level set of the function ϕ_1 .

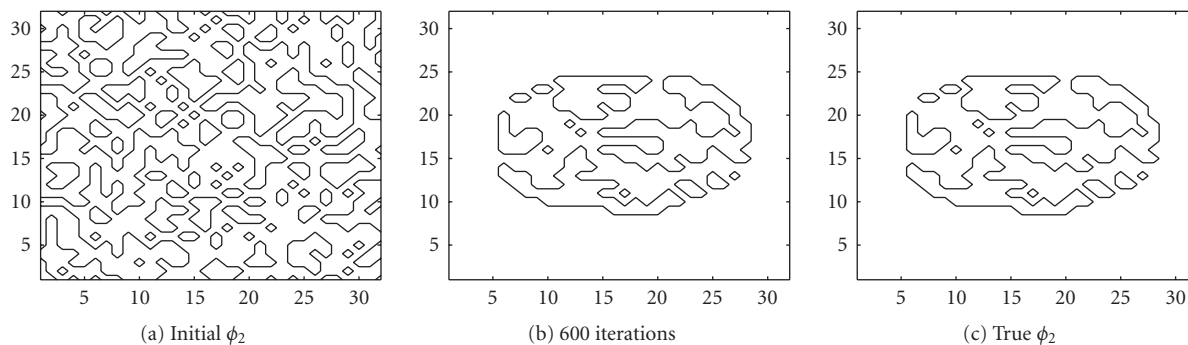


FIGURE 9: Interfaces given by the zero level set of the function ϕ_2 .

6.2. Incorporating prior information

To obtain improved reconstructions, one approach is to use priors that reflect the nature of the underlying radionuclide distribution. Recently, there has been a considerable interest in incorporating side information derived from highly correlated anatomical information (such as MRI and CT) in the form of Bayesian priors [22, 48]. The main attraction of this approach is that one can expect to obtain improved reconstructions to the extent that functions follow anatomy. Usually, the anatomical information is incorporated by some penalty technique, and a parameter β is used to control the influence of the priors, which should smooth the image un-

der reconstruction. There are also some papers dedicated to keeping sharp boundaries in the smoothing process. The key point there is to try to derive and represent the boundary information in the form of local smoother from the anatomical MRI or CT image. However, by level set formulation, the anatomical information can be incorporated into the EM algorithm in a natural and efficient way, and the sharp boundaries are preserved naturally and easily. We just need to know the location of the boundaries, the intensity values in the CT or MRI image are not necessary.

Assume that MRI or CT observations are used to generate information of the PET phantom, partly or in the entire domain Ω —see [49, 50]. Below we will demonstrate that such

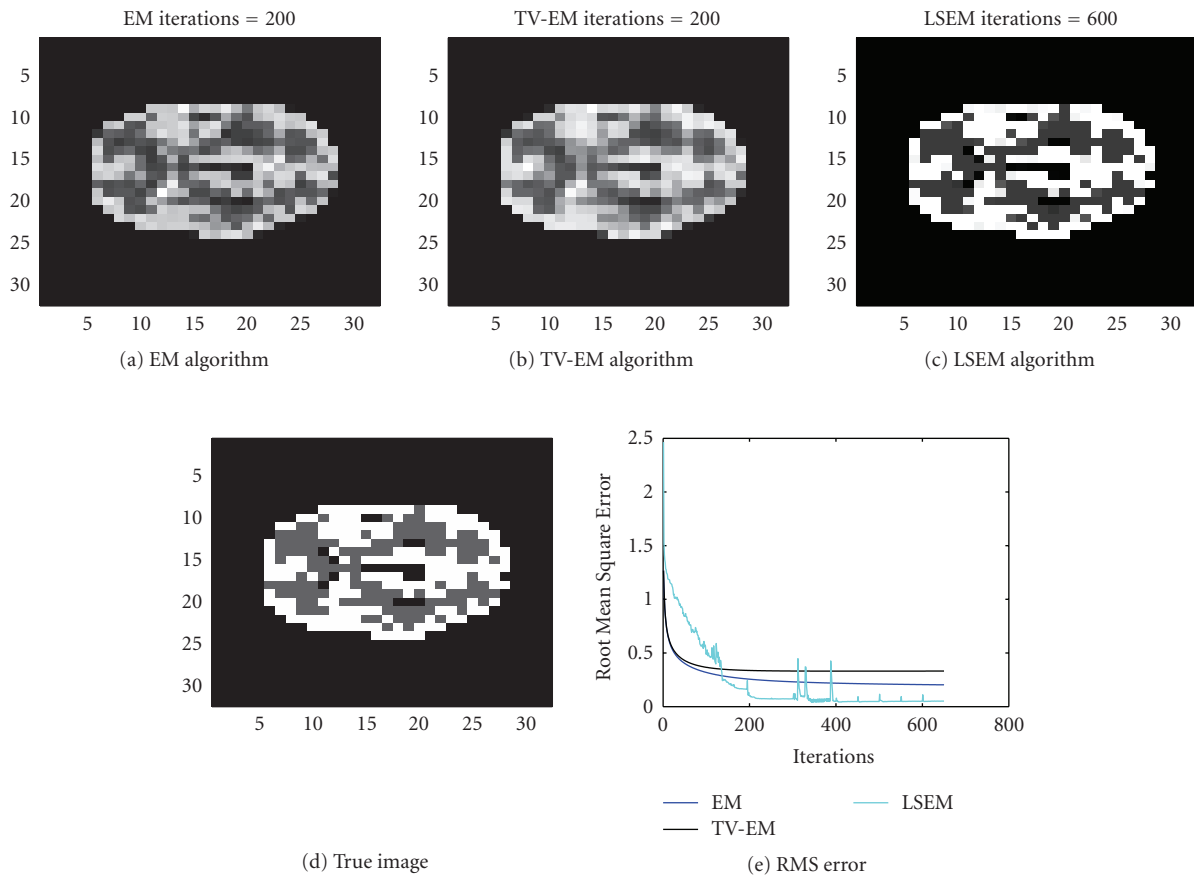
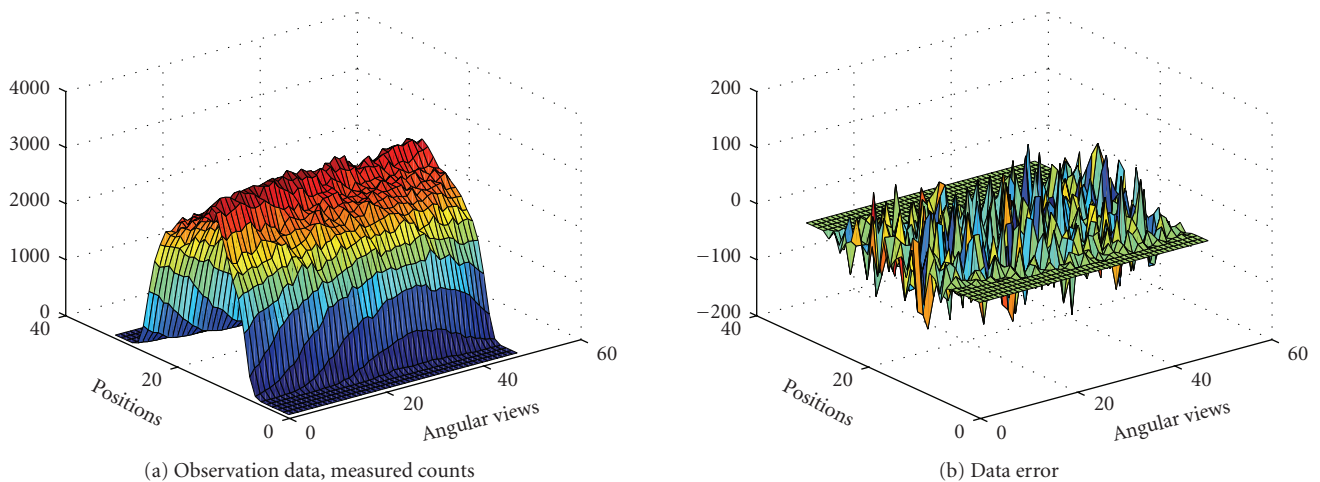


FIGURE 10: Construction of a PET image with different algorithms.

FIGURE 11: Sinogram data, obtained by forward projection: $n = P\lambda$ plus Poisson noise.

information will improve the image reconstruction capacity noticeably. First, we assume both ϕ_1 and ϕ_2 to be known, which means that all the boundaries are known a priori, and we just need to recover the piecewise constant intensity values of the image. The result is shown in Figure 15. Compared

with the results in Figure 14, we see that a prior information of the geometrical objects improves the reconstruction dramatically. We need only about 20 iterations to reconstruct a perfect image. In this case, after 200 iterations, the intensity values were recovered pretty well as $\{0, 1.01, 3.98\}$.

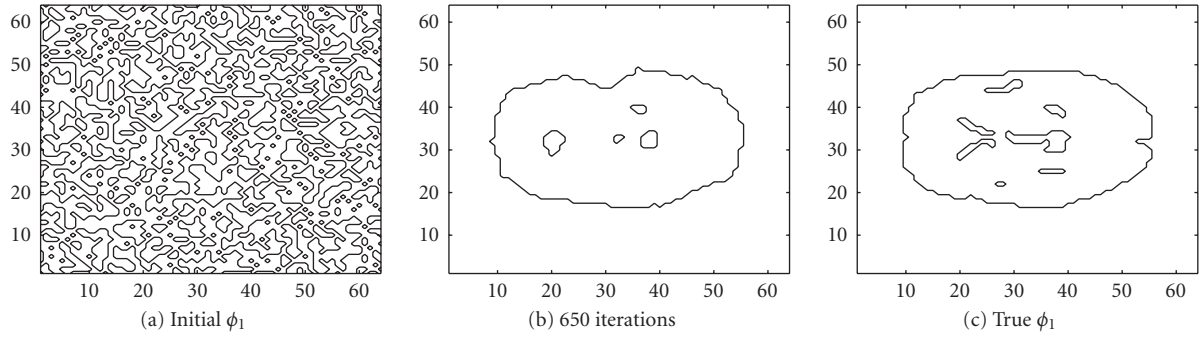


FIGURE 12: Interfaces given by the zero level set of ϕ_1 .

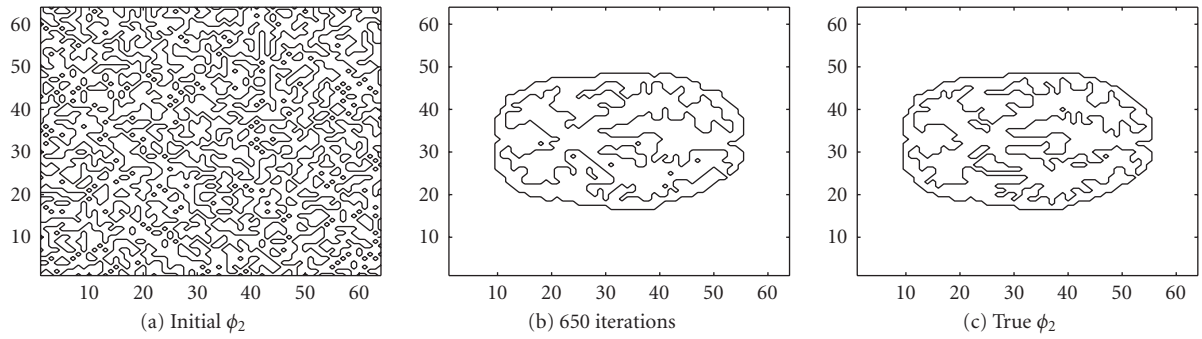


FIGURE 13: Interfaces given by the zero level set of ϕ_2 .

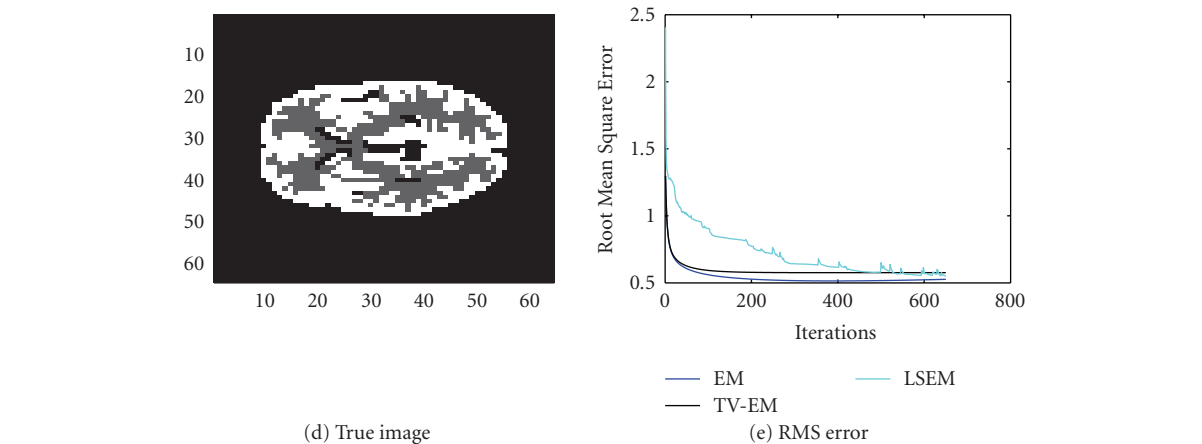
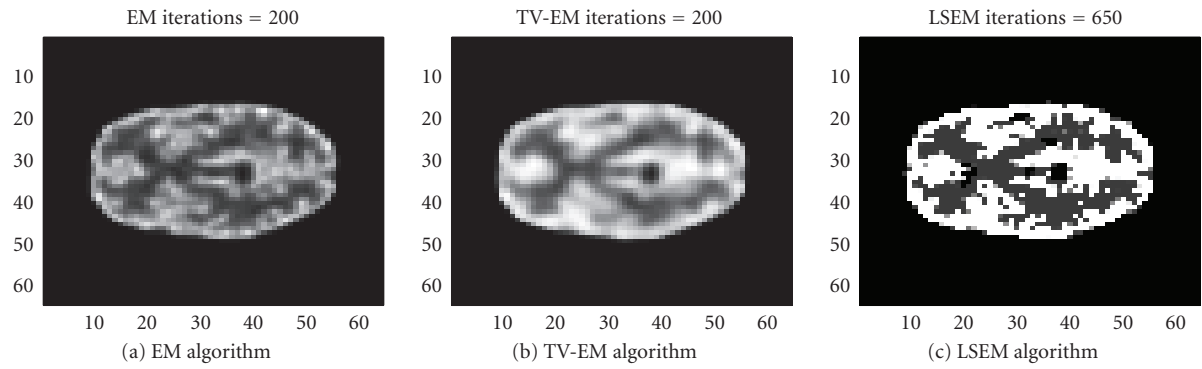
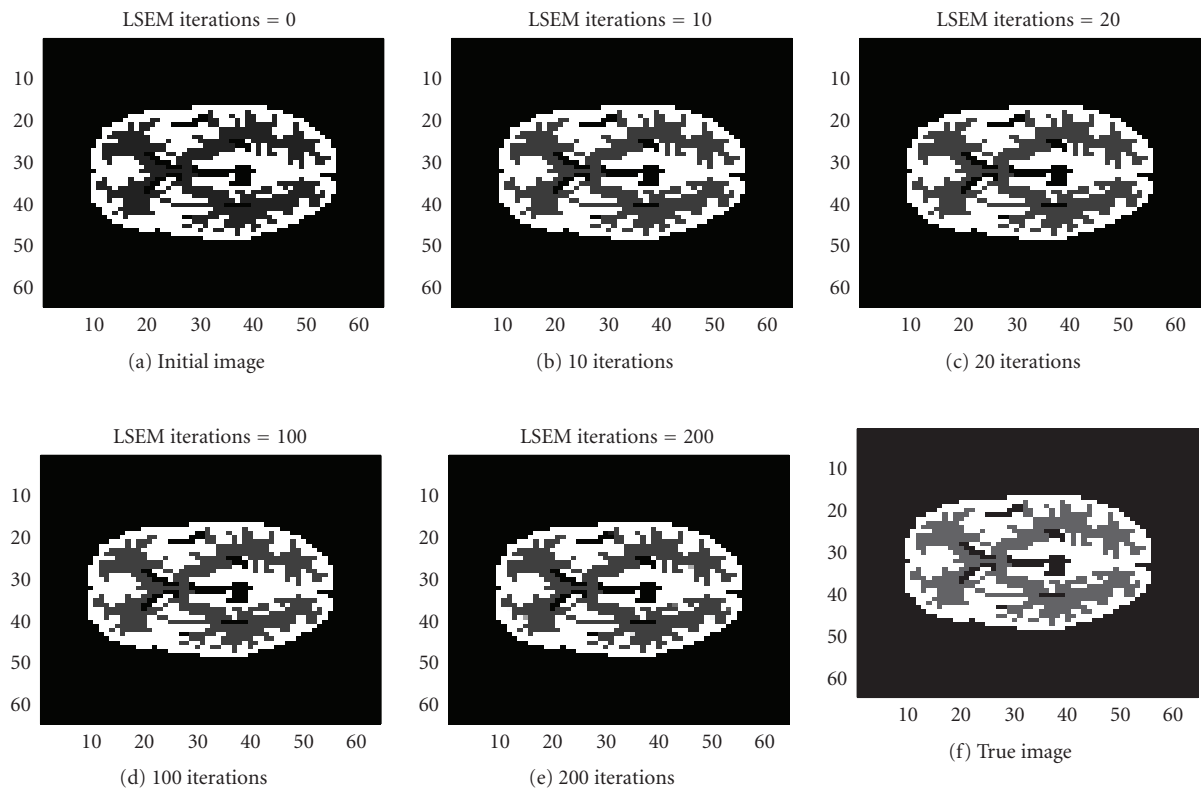
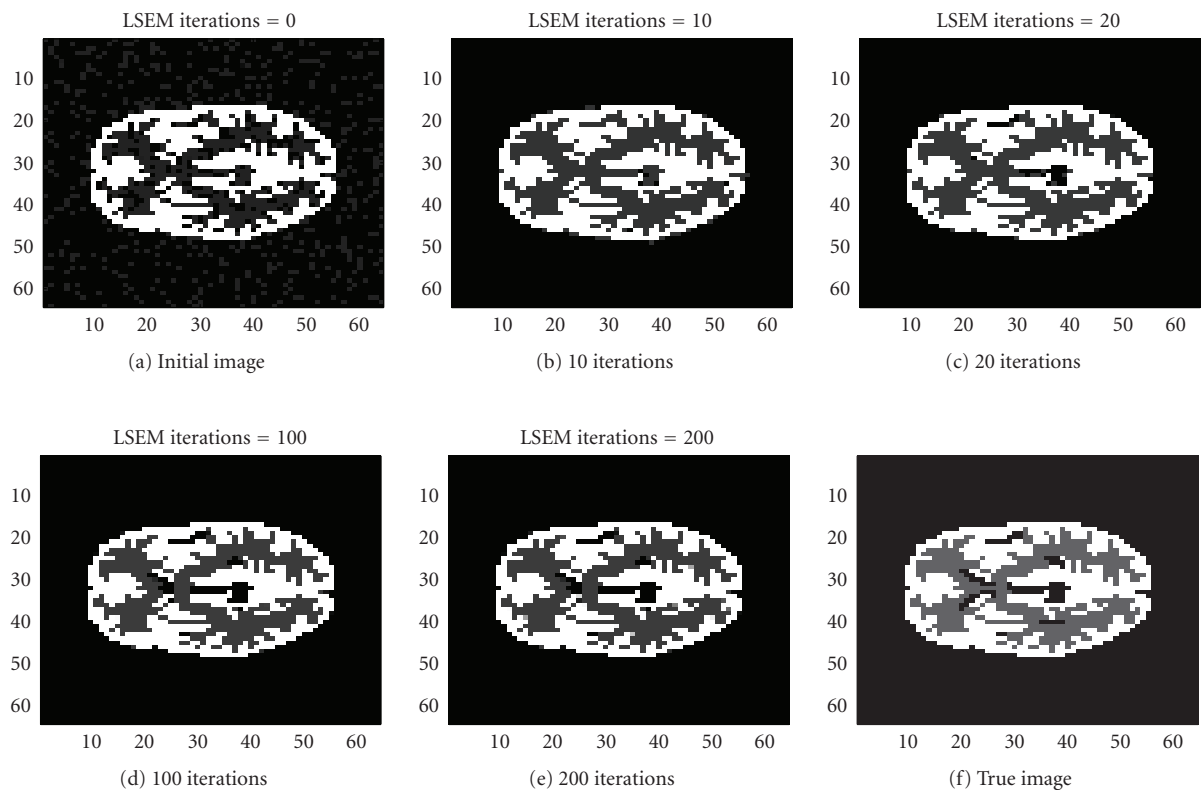


FIGURE 14: 64×64 segmented MRI slice of the brain.

FIGURE 15: 64×64 segmented MRI slice of the brain.FIGURE 16: 64×64 segmented MRI slice of the brain.

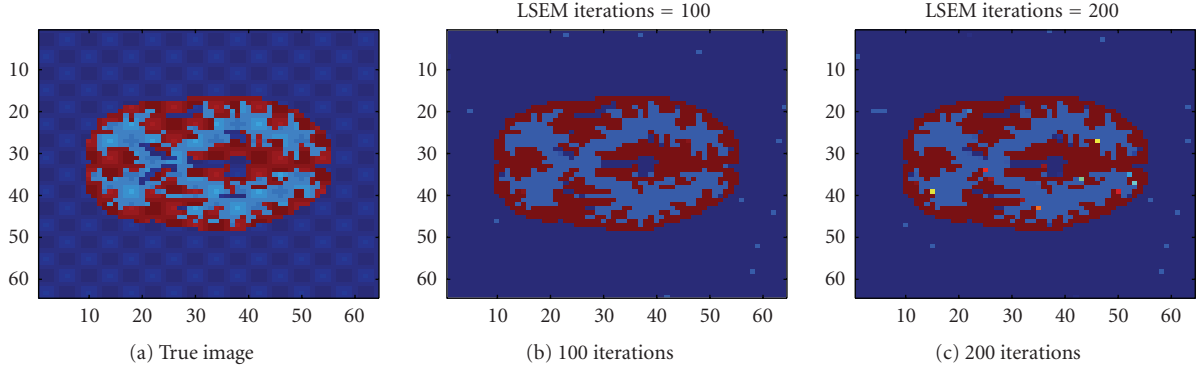


FIGURE 17: 64×64 segmented MRI slice of the brain, nonpiecewise constant by adding $\sin()$ functions.

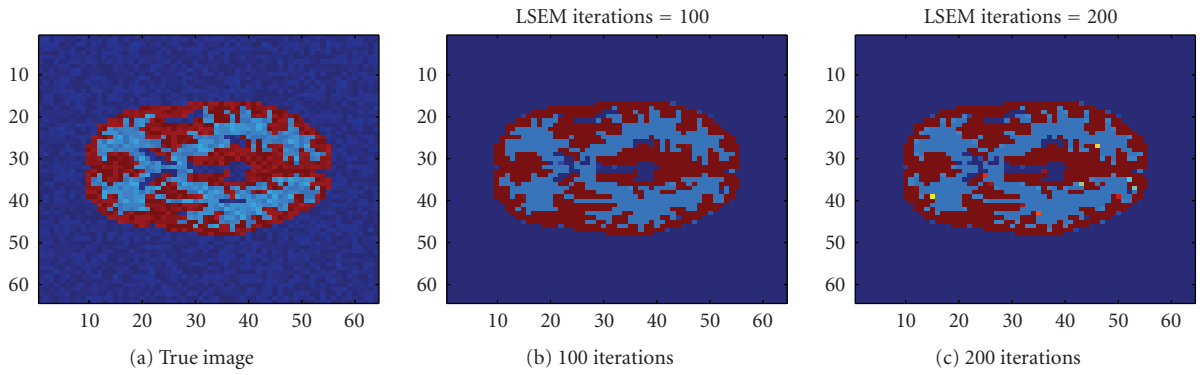


FIGURE 18: 64×64 segmented MRI slice of the brain, nonpiecewise constant by adding $\text{Rand}()$ functions.

Next, we assume ϕ_2 to be known, and let ϕ_1 evolves freely. This corresponds to wrong or incomplete anatomical information. The results are shown in Figure 16. From this example, we see that LSEM can tolerate wrong or incomplete anatomical priors. In this case, LSEM will try to discard the wrong information. After 200 iterations, the intensity values were recovered as $\{0, 0.97, 3.99\}$.

In our final example, we try to show that our method works well for nonpiecewise constant images. Let $\lambda(x, y)$ denotes the 64×64 true piecewise constant image as in the above example. We also assume that ϕ_2 is known, while ϕ_1 is unknown.

Firstly, we add a smooth function to the original piecewise constant image, so that the true image is somehow piecewise smooth,

$$\bar{\lambda}(x, y) = \lambda(x, y) + \sigma \star (\sin(16\pi x) \sin(16\pi y)). \quad (27)$$

The original true image as well as the reconstructed image are shown in Figure 17. We use $\sigma = 0.1$ in this test. The intensity values were recovered as $\{0, 0.92, 3.99\}$.

Then, we add random noise to the true piecewise constant image by

$$\bar{\lambda}(x, y) = \lambda(x, y) + \sigma \star (\text{Rand}(x, y) - 0.5), \quad (28)$$

where $\text{Rand}(x, y)$ produces uniformly distributed real numbers between $[0, 1]$. In this test, we use $\sigma = 0.2$.

The original true image as well as the reconstructed image are shown in Figure 18. The intensity values were recovered as $\{0, 0.99, 3.99\}$.

7. CONCLUSIONS

We have applied a level set method to the positron emission tomography reconstruction problem, based on the assumption that the active values can be identified with different levels.

The basic idea is to modify the maximum likelihood expectation maximization algorithm by using a level set formulation. With this approach, we can incorporate anatomical prior information naturally and easily into the algorithm.

ACKNOWLEDGMENTS

The authors would like to thank Sung-Cheng Huang at the Department of Molecular and Medical Pharmacology, University of Los Angeles, for providing the PET data for all the numerical examples in this paper. The authors acknowledge

support from the NSF under contracts NSF ACI-0072112, NSF INT-0072863, NSF DMS 99-73341, NSF DMS-0610079, from the ONR under grants N00014-96-1-10277, N00014-06-1-0345, from the NIH under grants P20MH65166, U54 RR021813, from the Norwegian Research Council of Norway, from CMA (Center of Mathematics for Applications), and from CIPR (Center for integrated Petroleum Research).

REFERENCES

- [1] S. R. Deans, *The Radon Transform and Some of Its Applications*, John Wiley & Sons, New York, NY, USA, 1983.
- [2] M. Bertero and P. Boccacci, *Introduction to Inverse Problems in Imaging*, Institute of Physics, Bristol, UK, 1998.
- [3] A. K. Louis, "Parametric reconstruction of a biomagnetic imaging," in *Inverse Problems in Scattering and Imaging*, M. Bertero and E. R. Pike, Eds., pp. 156–163, Adam Hilger, Bristol, UK, 1992.
- [4] A. P. Dempster, N. M. Laird, and D. B. Rubin, "Maximum likelihood from incomplete data via the EM algorithm," *Journal of the Royal Statistical Society, Series B*, vol. 39, no. 1, pp. 1–38, 1977.
- [5] K. Lange and R. Carson, "EM reconstruction algorithms for emission and transmission tomography," *Journal of Computer Assisted Tomography*, vol. 8, no. 2, pp. 306–316, 1984.
- [6] L. A. Shepp and Y. Vardi, "Maximum likelihood reconstruction for emission tomography," *IEEE Transactions on Medical Imaging*, vol. 1, no. 2, pp. 113–122, 1982.
- [7] E. Veklerov and J. Llacer, "Stopping rule for the MLE algorithm based on statistical hypothesis testing," *IEEE Transactions on Medical Imaging*, vol. 6, no. 4, pp. 313–319, 1987.
- [8] T. Hebert and R. Leahy, "A generalized EM algorithm for 3-D Bayesian reconstruction from Poisson data using Gibbs priors," *IEEE Transactions on Medical Imaging*, vol. 8, no. 2, pp. 194–202, 1989.
- [9] P. J. Green, "Bayesian reconstructions from emission tomography data using a modified EM algorithm," *IEEE Transactions on Medical Imaging*, vol. 9, no. 1, pp. 84–93, 1990.
- [10] S. Alenius and U. Ruotsalainen, "Bayesian image reconstruction for emission tomography based on median root prior," *European Journal of Nuclear Medicine*, vol. 24, no. 3, pp. 258–265, 1997.
- [11] L. I. Rudin, S. Osher, and E. Fatemi, "Nonlinear total variation based noise removal algorithms," *Physica D*, vol. 60, no. 1–4, pp. 259–268, 1992.
- [12] M. Lysaker, S. Osher, and X.-C. Tai, "Noise removal using smoothed normals and surface fitting," *IEEE Transactions on Image Processing*, vol. 13, no. 10, pp. 1345–1357, 2004.
- [13] C. R. Vogel and M. E. Oman, "Iterative methods for total variation denoising," *SIAM Journal on Scientific Computing*, vol. 17, no. 1, pp. 227–238, 1996.
- [14] D. Dobson and O. Scherzer, "Analysis of regularized total variation penalty methods for denoising," *Inverse Problems*, vol. 12, no. 5, pp. 601–617, 1996.
- [15] O. Scherzer and J. Weickert, "Relations between regularization and diffusion filtering," *Journal of Mathematical Imaging and Vision*, vol. 12, no. 1, pp. 43–63, 2000.
- [16] M. J. Black, G. Sapiro, D. H. Marimont, and D. Heeger, "Robust anisotropic diffusion," *IEEE Transactions on Image Processing*, vol. 7, no. 3, pp. 421–432, 1998.
- [17] S. Teboul, L. Blanc-Féraud, G. Aubert, and M. Barlaud, "Variational approach for edge-preserving regularization using coupled PDE's," *IEEE Transactions on Image Processing*, vol. 7, no. 3, pp. 387–397, 1998.
- [18] E. Jonsson, S. C. Huang, and T. F. Chan, "Total variation regularization in positron emission tomography," Tech. Rep. CAM Report 98-48, Department of Mathematics, UCLA, Los Angeles, Calif, USA, 1998.
- [19] D. F. Yu and J. A. Fessler, "Edge-preserving tomographic reconstruction with nonlocal regularization," *IEEE Transactions on Medical Imaging*, vol. 21, no. 2, pp. 159–173, 2002.
- [20] E. Ü. Mumcuoglu, R. M. Leahy, and S. R. Cherry, "Bayesian reconstruction of PET images: methodology and performance analysis," *Physics in Medicine and Biology*, vol. 41, no. 9, pp. 1777–1807, 1996.
- [21] C. Comtat, P. E. Kinahan, J. A. Fessler, et al., "Clinically feasible reconstruction of 3D whole-body PET/CT data using blurred anatomical labels," *Physics in Medicine and Biology*, vol. 47, no. 1, pp. 1–20, 2002.
- [22] B. A. Ardekani, M. Braun, B. F. Hutton, I. Kanno, and H. Iida, "Minimum cross-entropy reconstruction of PET images using prior anatomical information," *Physics in Medicine and Biology*, vol. 41, no. 11, pp. 2497–2517, 1996.
- [23] M. Schwaiger, S. Ziegler, and S. G. Nekolla, "PET/CT: challenge for nuclear cardiology," *Journal of Nuclear Medicine*, vol. 46, no. 10, pp. 1664–1678, 2005.
- [24] A. M. Alessio, P. E. Kinahan, P. M. Cheng, H. Vesselle, and J. S. Karp, "PET/CT scanner instrumentation, challenges, and solutions," *Radiologic Clinics of North America*, vol. 42, no. 6, pp. 1017–1032, 2004.
- [25] S. Osher and J. A. Sethian, "Fronts propagating with curvature-dependent speed: algorithms based on Hamilton-Jacobi formulations," *Journal of Computational Physics*, vol. 79, no. 1, pp. 12–49, 1988.
- [26] S. Osher and R. P. Fedkiw, "Level set methods: an overview and some recent results," *Journal of Computational Physics*, vol. 169, no. 2, pp. 463–502, 2001.
- [27] J. A. Sethian, *Level Set Methods and Fast Marching Methods: Evolving Interfaces in Computational Geometry, Fluid Mechanics, Computer Vision, and Materials Science*, vol. 3 of *Cambridge Monographs on Applied and Computational Mathematics*, Cambridge University Press, Cambridge, UK, 2nd edition, 1999.
- [28] S. Osher and R. P. Fedkiw, *Level Set Methods and Dynamic Implicit Surfaces*, vol. 153 of *Applied Mathematical Sciences*, Springer, New York, NY, USA, 2003.
- [29] X.-C. Tai and T. F. Chan, "A survey on multiple set methods with applications for identifying piecewise constant function," *International Journal of Numerical Analysis and Modeling*, vol. 1, no. 1, pp. 25–47, 2004.
- [30] E. T. Chung, T. F. Chan, and X.-C. Tai, "Electrical impedance tomography using level set representation and total variational regularization," *Journal of Computational Physics*, vol. 205, no. 1, pp. 357–372, 2005.
- [31] O. Dorn, E. L. Miller, and C. M. Rappaport, "A shape reconstruction method for electromagnetic tomography using adjacent fields and level sets," *Inverse Problems*, vol. 16, no. 5, pp. 1119–1156, 2000.
- [32] A. Litman, D. Lesselier, and F. Santosa, "Reconstruction of a two-dimensional binary obstacle by controlled evolution of a level-set," *Inverse Problems*, vol. 14, no. 3, pp. 685–706, 1998.

- [33] H. Feng, W. C. Karl, and D. A. Castañon, "A curve evolution approach to object-based tomographic reconstruction," *IEEE Transactions on Image Processing*, vol. 12, no. 1, pp. 44–57, 2003.
- [34] J. C. Ye, Y. Bresler, and P. Moulin, "A self-referencing level-set method for image reconstruction from sparse fourier samples," *International Journal of Computer Vision*, vol. 50, no. 3, pp. 253–270, 2002.
- [35] R. T. Whitaker and V. Elangovan, "A direct approach to estimating surfaces in tomographic data," *Medical Image Analysis*, vol. 6, no. 3, pp. 235–249, 2002.
- [36] P.-C. Chiao, W. L. Rogers, N. H. Clinthorne, J. A. Fessler, and A. O. Hero, "Model-based estimation for dynamic cardiac studies using ECT," *IEEE Transactions on Medical Imaging*, vol. 13, no. 2, pp. 217–226, 1994.
- [37] P.-C. Chiao, W. L. Rogers, J. A. Fessler, N. H. Clinthorne, and A. O. Hero, "Model-based estimation with boundary side information or boundary regularization," *IEEE Transactions on Medical Imaging*, vol. 13, no. 2, pp. 227–234, 1994.
- [38] C. V. Alvino and A. J. Yezzi Jr., "Tomographic reconstruction of piecewise smooth images," in *Proceedings of IEEE Computer Society Conference on Computer Vision and Pattern Recognition (CVPR '04)*, vol. 1, pp. 576–581, Washington, DC, USA, June–July 2004.
- [39] L. A. Vese and T. F. Chan, "A multiphase level set framework for image segmentation using the Mumford and Shah model," *International Journal of Computer Vision*, vol. 50, no. 3, pp. 271–293, 2002.
- [40] T. F. Chan and X.-C. Tai, "Level set and total variation regularization for elliptic inverse problems with discontinuous coefficients," *Journal of Computational Physics*, vol. 193, no. 1, pp. 40–66, 2004.
- [41] J. Llacer, S. Andraea, E. Veklerov, and E. J. Hoffman, "Towards a practical implementation of the MLE algorithm for positron emission tomography," *IEEE Transactions on Nuclear Science*, vol. 33, no. 1, pp. 468–477, 1985.
- [42] E. Veklerov, J. Llacer, and E. J. Hoffman, "MLE reconstructions of a brain phantom using a Monte Carlo transition matrix and a statistical stopping rule," *IEEE Transactions on Nuclear Science*, vol. 35, no. 1, part 1-2, pp. 603–607, 1988.
- [43] D. L. Snyder and M. I. Miller, "The use of sieves to stabilize images produced with the EM algorithm for emission tomography," *IEEE Transactions on Nuclear Science*, vol. 32, no. 5, pp. 3864–3872, 1985.
- [44] J. Lie, M. Lysaker, and X.-C. Tai, "A variant of the level set method and applications to image segmentation," Tech. Rep. CAM Report 03-50, Department of Mathematics, UCLA, Los Angeles, Calif, USA, 2003.
- [45] H.-K. Zhao, T. F. Chan, B. Merriman, and S. Osher, "A variational level set approach to multiphase motion," *Journal of Computational Physics*, vol. 127, no. 1, pp. 179–195, 1996.
- [46] T. F. Chan and L. A. Vese, "Image segmentation using level sets and the piecewise constant Mumford-Shah model," Tech. Rep. CAM Report 00-14, Department of Mathematics, UCLA, Los Angeles, Calif, USA, April 2000, revised December 2000.
- [47] D. Peng, B. Merriman, S. Osher, H. Zhao, and M. Kang, "A PDE-based fast local level set method," *Journal of Computational Physics*, vol. 155, no. 2, pp. 410–438, 1999.
- [48] G. Gindi, M. Lee, A. Rangarajan, and I. G. Zubal, "Bayesian reconstruction of functional images using anatomical information as priors," *IEEE Transactions on Medical Imaging*, vol. 12, no. 4, pp. 670–680, 1993.
- [49] C. C. Meltzer, R. N. Bryan, H. H. Holcomb, et al., "Anatomical localization for PET using MR imaging," *Journal of Computer Assisted Tomography*, vol. 14, no. 3, pp. 418–426, 1990.
- [50] A. C. Evans, C. Beil, S. Marrett, C. J. Thompson, and A. Hakim, "Anatomical-functional correlation using an adjustable MRI-based region of interest atlas with positron emission tomography," *Journal of Cerebral Blood Flow and Metabolism*, vol. 8, no. 4, pp. 513–530, 1988.

Research Article

Magnetic Field Distribution and Signal Decay in Functional MRI in Very High Fields (up to 9.4 T) Using Monte Carlo Diffusion Modeling

Bernd Michael Mueller-Bierl,¹ Kamil Uludag,¹ Philippe L. Pereira,² and Fritz Schick³

¹Max-Planck Institute for Biological Cybernetics, Spemannstraße 41, 72076 Tübingen, Germany

²Department of Diagnostic Radiology, University Clinic Tuebingen, 72076 Tübingen, Germany

³Section on Experimental Radiology, Department of Diagnostic Radiology, University Clinic Tuebingen, 72076 Tübingen, Germany

Received 28 September 2006; Revised 30 May 2007; Accepted 25 August 2007

Recommended by Tie Zhou

Extravascular signal decay rate R_2 or R_2^* as a function of blood oxygenation, geometry, and field strength was calculated using a Monte Carlo (MC) algorithm for a wider parameter range than hitherto by others. The relaxation rates of gradient-recalled-echo (GRE) and Hahn-spin-echo (HSE) imaging in the presence of blood vessels (ranging from capillaries to veins) have been computed for a wide range of field strengths up to 9.4 T and 50% blood deoxygenation. The maximum HSE decay was found to be shifted to lower radii in higher compared to lower field strengths. For GRE, however, the relaxation rate was greatest for large vessels at any field strength. In addition, assessments of computational reliability have been carried out by investigating the influence of the time step, the Monte Carlo step procedure, boundary conditions, the number of angles between the vessel and the exterior field B_0 , the influence of neighboring vessels having the same orientation as the central vessel, and the number of proton spins. The results were compared with those obtained from a field distribution of the vessel computed by an analytic formula describing the field distribution of an ideal object (an infinitely long cylinder). It was found that the time step is not critical for values equal to or lower than 200 microseconds. The choice of the MC step procedure (three-dimensional Gaussian diffusion, constant one- or three-dimensional diffusion step) also failed to influence the results significantly; in contrast, the free boundary conditions, as well as taking too few angles into account, did introduce errors. Next neighbor vessels with the same orientation as the main vessel did not contribute significantly to signal decay. The total number of particles simulated was also found to play a minor role in computing R_2/R_2^* .

Copyright © 2007 Bernd Michael Mueller-Bierl et al. This is an open access article distributed under the Creative Commons Attribution License, which permits unrestricted use, distribution, and reproduction in any medium, provided the original work is properly cited.

1. INTRODUCTION

The effect of diffusion on signal decay in blood oxygenation level-dependent (BOLD) imaging is mainly due to the extravascular contribution of spins, especially at high field strengths >4 T [1]. In the current study, the well-known Monte Carlo (MC) approach modeling Brownian diffusion of protons in a background magnetic field has been used to compute extravascular (EV) BOLD signal changes. To this end, the static dipole model presented previously [2] has been extended to a dynamic model describing the sampling of phases of the individual protons moving in the inhomogeneous magnetic field.

Earlier studies on the effect of subvoxel variations in magnetic susceptibility were reported by Fisel et al. [3]. Weis-

skoff et al. compared MC simulations with experiments with polystyrene microspheres to demonstrate that enhanced relaxation can be explained quantitatively for both spin-echo and gradient-echo experiments [4]. The effect of an endogenous paramagnetic agent (deoxygenated hemoglobin) on image contrast has been addressed by several authors, for example, Ogawa et al. [5], Kennan et al. [6], and Boxerman et al. [7]. All models are based on the fact that in the vicinity of capillaries and venules, local magnetic field distortions are generated by the presence of paramagnetic deoxyhemoglobin in the blood.

Data from the models in the literature so far have mostly been restricted to a magnetic field strength of 1.5 T, that is, the clinical scanner field strength in the past, and mostly for GRE only. However, nowadays, scanners with high or

ultra-high field strength for humans up to 9.4 T are available for research, and EV-BOLD data for these field strengths both for GRE and HSE have not yet been provided. The aim of the present work, therefore, was to investigate these issues at such high magnetic field strengths.

To examine the contribution of extravascular spin in isolation from other factors, an impenetrable vessel wall boundary for extravascular spins was assumed. The range of investigated susceptibility values was determined using a deoxygenation content of 5% at 1.5 T as the lowest susceptibility value and up to 50% at 9.4 T as the highest value. In addition, standard approaches used in the literature have been evaluated as to how they influence the computed relaxation rates. In particular, the choice of the time step, the diffusion step, the number of angles and the influence of neighboring vessels, and the number of protons were examined.

2. THEORY

Our aim was to study signal decay due to the phase sampling of the individual spins during their random movement. The spins in the brain parenchyma are diffusing in a background magnetic field caused by deoxygenated blood present in capillaries, venules, and veins. The field distribution is therefore determined by vessels inside a computational volume, filled with deoxygenated blood. The susceptibility creating the field distribution around the blood vessel is proportional to the level of blood deoxygenation and to the exterior field.

Weisskoff et al. proposed generalizing their results obtained using a numerical model by the use of the Bloch-Torrey equation [4]. Fujita also established a dimensionless equation which is ruled by two parameters [8]. We briefly recapitulate their arguments in the following paragraph and thereby show how their theories relate to one other.

Because the MC method solution must respect the Bloch-Torrey equations, generalized scaling laws might be derived in advance to generalize the numerical solutions [4]. If the length scale is made dimensionless by $x \mapsto y = \lambda \cdot x$, we obtain

$$\frac{dS(y, t)}{dt} = i\omega(y) \cdot S(y, t) + (\lambda^2 D) \cdot \nabla^2 S(y, t). \quad (1)$$

If the time scale is made dimensionless by $t \mapsto t' = t/\gamma$, we obtain

$$\frac{dS(x, t')}{dt} = i \cdot \gamma \cdot \omega(x) \cdot S(x, t') + (\gamma \cdot D) \cdot \nabla^2 S(x, t'). \quad (2)$$

Substituting λ by $\lambda \mapsto 1/R$ and γ by $\gamma \mapsto TE$, the general scale independent relation

$$\frac{dS}{dt} = -i \cdot \alpha \cdot S + \beta \cdot \nabla^2 S \quad (3)$$

with $\alpha = \omega \cdot TE$ and $\beta = DTE/R^2$ can be established. From this equation, (3), (1), and (2) follow as special cases. The minus sign in (3) indicates the direction of rotation in the complex plane and therefore can be omitted. In the present article, we use cgs units with $D = 1 \mu\text{m}^2/\text{ms}$ and $TE = 40$ milliseconds.

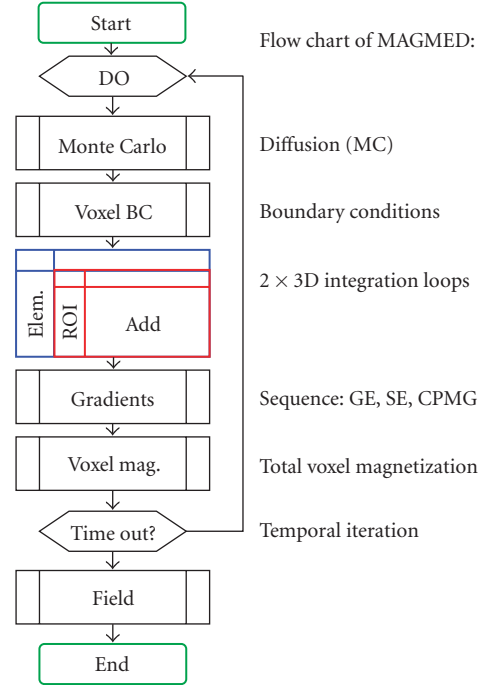


FIGURE 1: Flow chart of the model. It consists of the dipole model and a Monte Carlo time-step procedure. The inner of the two 3D loops is substituted in the present work by a known field distribution for the element (i.e., the field distribution for an infinite vessel).

3. MATERIAL AND METHODS

3.1. Flow chart

Our model is similar to that of Boxerman et al. [7]. A flow chart illustrating the model is shown in Figure 1. The total signal is computed from individual complex transverse magnetizations of the protons, which are accumulating phases in the magnetic background field. The magnetic background field is described either by an analytic formula, or by integrating the individual contributions from the discretized susceptibility distribution.

We used the field distribution caused by a vessel segment approximated by a paramagnetic cylinder with infinite length to be the susceptibility distribution for an infinite vessel, which is given by

$$\begin{aligned} \delta\omega \cdot f(x) &= \delta\omega \cdot \left(\frac{1}{r}\right)^2 \cos(2 \cdot \phi) \sin(\theta) \quad (r \geq 1) \\ &= \delta\omega \cdot \left(\cos^2 \theta - \frac{1}{3}\right) \quad (r \geq 1), \end{aligned} \quad (4)$$

where θ is the angle between the cylinder and the direction of the static magnetic field, r and ϕ represent the nondimensional radial coordinate relative to the vessel radius R and the azimuthal angle in the plane orthogonal to the cylinder, respectively, and $\delta\omega$ is the susceptibility-induced maximal frequency shift occurring at the vessel surface, given by

$$\delta\omega = 2\pi \cdot \Delta\chi \cdot \omega_0 \text{Hct}(1 - Y). \quad (5)$$

In (5), Hct denotes the haematocrit value, that is, the fraction of the volume taken up by the red blood cells, $\Delta\chi$ is the volume susceptibility difference per unit Hct between fully oxygenated and fully deoxygenated blood, ω_0 is the static magnetic field strength in terms of frequency, and Y is the degree of blood oxygenation.

Our parameter space was given by a haematocrit value of Hct = 0.4, a susceptibility of fully deoxygenated blood of $\Delta\chi = 0.18$ ppm (cgs units). Frequency thus varied from 1.4454 Hz (corresponding to $1-Y = 5\%$ at 1.5 T) to 65×1.4454 Hz (90.58 Hz corresponding to $1-Y = 50\%$ at 9.4 T) in steps of 5.7816 Hz. The radii varied from $3 \mu\text{m}$ to $60 \mu\text{m}$ in logarithmical equidistant values.

Alternatively, one could discretize the paramagnetic cylinder representing the vessel into elementary volumes, for example, of size of the computational cell. In the dipole model, to each elementary volume, a dipole strength $p_m = M\Delta V$ is assigned, where M is the magnetization proportional to the exterior field strength $M = \chi B_0$. The elementary volume then contributes to the field distribution by an amount of $\Delta B_z = (p_m/r^3)(3\cos^2\theta - 1)$.

To compute the total field distortion B_z , a spatial integration to summate all contributions has to be performed. Diffusion was computed according to 3 models which can be distinguished by the choice of the diffusion step. They are given by the following definitions.

STEP1D

Take a fixed step ($\ell = \sqrt{2D\tau}$) in each direction (along the positive or negative axis, directions chosen randomly).

STEP3D

Take a fixed step ($\ell = \sqrt{6D\tau}$) in a randomly chosen direction.

GAUSS3D

Take a random step with a Gaussian distribution ($\sigma = \sqrt{6D\tau}$) in a randomly chosen direction.

In the formulae, D is the diffusion coefficient and τ is the time step. As diffusion strength, we used $D = 1 \mu\text{m}^2/\text{ms}$, which is typical for the cerebral cortex [7]. As a random generator, the routine ran1 from the numerical recipes [9] was chosen. The various MC step methods were first tested by computing the radial distribution of the protons after N time steps for M protons. Unless stated otherwise, the time step τ was chosen as 10 microseconds and TE was 40 milliseconds at maximum, and the number of protons was 24^3 .

Using these definitions, the routines given by Ogawa et al. [5] (Step3D), Boxerman et al. [7] (Gauss1D), and Weiskoff et al. [4] (Gauss1D) were explored. Gauss1D, of course, is a hybrid of Step1D and Gauss3D. The arbitrarily chosen direction must be determined from random values lying inside a sphere (except the origin). To determine the direction, the values have been projected onto the unit sphere's surface. The time step was chosen as either 10 microseconds or 200 microseconds for the GE and SE signal relaxation rate computations. Initial positioning and the Monte Carlo steps

were ruled by two separate random generators from Press et al., that is, using the same starting conditions, the results can be reproduced completely. Computations have been repeated and mean values have been calculated to reduce numerical noise due to the finite-sized sample of proton spins.

The model consists of the following steps:

- (1) place a cylinder with a given orientation relative to B_0 in a volume of interest;
- (2) distribute protons randomly in that volume of interest;
- (3) compute the field at the location of each proton as a superposition of the field generated by the cylinder;
- (4) (optional) add the gradient fields from the MR sequence at the location of each proton (e.g., to simulate a CPMG echo train);
- (5) advance the phase of each proton according to its local field and, in case of a 180° pulse for HSE, invert the direction of phase accumulation;
- (6) advance each proton in an MC step in an arbitrary direction (in the case of a 3D step chosen from an arbitrary position on the surface of a unit sphere);
- (7) if the proton has transgressed the cylinder wall, repeat step (6) with a given probability, which is determined by the vessel wall porosity (in our case: repeat step (6) always);
- (8) if the proton has left the volume of interest, it might reenter, depending on suitable boundary conditions.

The resulting signal was computed by summing all (normalized) complex magnetizations of the EV spins. Spins which did not contribute (spins inside the vessel) were ignored.

In (4), the cosine of the angle is computed as a scalar vector product. This, together with expressing the trigonometric functions by a cosine function, prevents the evaluation of trigonometric series, which is highly time consuming.

Instead of one cylinder, we also used 5 and 9 cylinders as illustrated, for example, by Kennan et al. for 5 cylinders [6].

As conditions at the limits of the computational domain, we used periodical boundary conditions (with the spins reentering the computational domain from the adjacent side of the domain), reflecting boundary conditions (with the spins being reflected at the limits of the domain), and free boundary conditions (where the spins are free to leave the domain).

Background gradients can be added to the exterior field at any time during the computations, so that diffusion-sensitive sequences like CPMG can be established.

The occurrence of vessel direction varies with $\sin(\theta)$, where θ is the angle between the exterior field and the vessel orientation. For our computations, we used 6, 9, and 18 angles, equally distributed between 0 and 90° . The total signal from vessels with varying orientation thus becomes [5]

$$S_{\text{tot}} = \frac{\sum \sin(\theta) \cdot |S(\theta)|}{\sum \sin(\theta)}. \quad (6)$$

The relaxation rate R2 was computed using a two-point evaluation function at TE = 16 milliseconds and TE = 40 milliseconds assuming $S_{\text{tot}} = S_0^* \exp(-TE \cdot R2)$ [5].

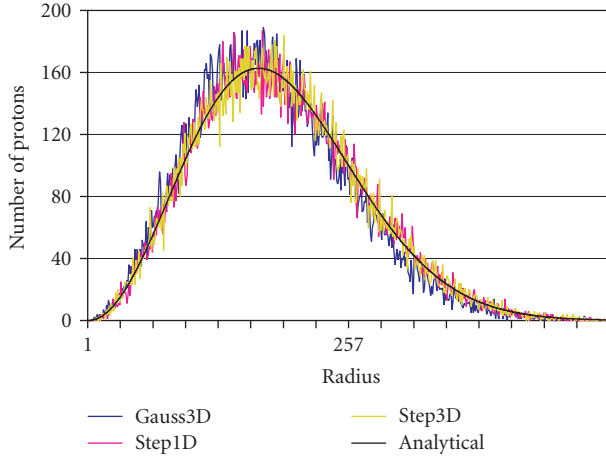


FIGURE 2: The radial spin position distribution shown after diffusion at time interval T_D . The protons all started from the origin at $T = 0$ and propagated in space corresponding to the different Monte Carlo step procedures Step1D, Step3D, and Gauss3D.

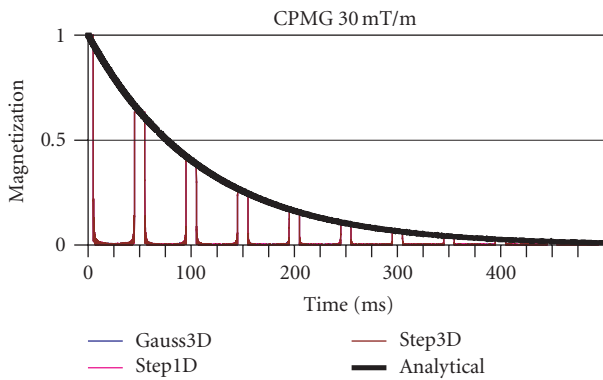


FIGURE 3: The analytical versus the computed decay curve of the transverse magnetization shown for a CPMG set of parameters.

4. NUMERICAL RESULTS

Testing of the diffusion process is shown in Figures 2 and 3: Figure 2 shows the distribution of spins after a fixed diffusion time T_D together with the theoretical distribution. Figure 3 shows the CPMG signal decay together with its analytical course. Both the local spin distribution as well as the CPMG signal decay follows the theoretical predictions with some random noise due to the limited number of protons.

Results for the computation of R_2/R_2^* for GRE and HSE imaging are shown in Figure 4. The curves are the mean values of 8 computations, each with a different random series initialization. Time step length has been set at 10 microseconds within these simulations. As can be seen, HSE relaxation rates are greatest for small radii, whereas for GRE large vessel radii have the highest relaxation rates. In addition, as expected, the relaxation rate both for GRE and HSE

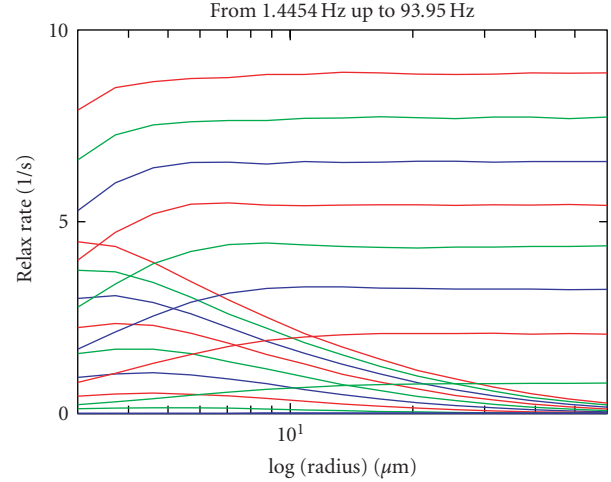


FIGURE 4: R_2/R_2^* relaxation rate (in s^{-1}) for SE, GE, from deoxygenation corresponding to a frequency of 1.4454 Hz to 65×1.4454 Hz. Data are shown in steps of 8×1.4454 Hz. The time step length in these computations was 10 microseconds. The mean value for 8 computations with different random series initialization is shown.

increase with blood oxygenation and field strength. Higher susceptibility for HSE results in shifting the maximal relaxation rate to even smaller radii.

Comparison of these results to computations with a time step length of 200 microseconds is shown in Figure 5. They agree with the results using the smaller time steps. The 200-microsecond data are slightly noisier since there is no averaging as in the 10-microsecond data, which have been computed 8 times for different random series initialization. Comparisons to a Gauss3D diffusion step computation and to a free boundary condition computation are also shown (time step 200 microseconds in both). Only the data for the free boundary computation are slightly inconsistent with the others.

Figure 6 compares the results of the 8 computations with a computation using 9 or 18 angles instead of 6 (time step 200 microseconds each). A nonnegligible deviation of the GE curve, and a slightly smaller deviation also for the SE curve can be seen (in the static dephasing regime: a deviation of 5% for 6 angles, i.e., a deviation of 2.5% for 9 compared to 18 angles). Again, data from the 9-angle versus 18-angle comparison have been computed only once.

In Figure 7, neighbor rods are taken into account and the result is compared to the result of the 8 computations with different random series initialization. Data for the 5 or 9 next neighbors have been computed once. There are no apparent differences compared to the computations with only one vessel.

Finally, in Figure 8, the data for different numbers of spins in the computational domain can be found. The numbers of spins distributed in the computational domain were 24^3 , 30^3 , 36^3 , 42^3 , and 48^3 (time step 200 microseconds each). A change in the number of spins does not result in any significant difference between the calculated relaxation rates.

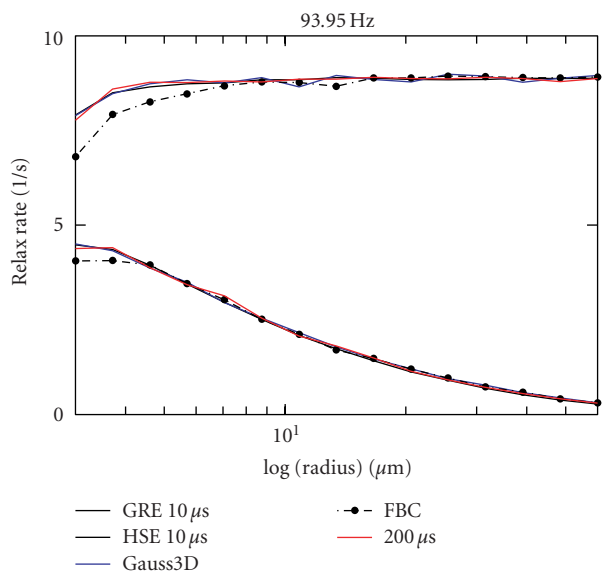


FIGURE 5: $R2/R2^*$ relaxation rate (in s^{-1}) for time step length of 10 microseconds versus 200 microseconds. Data for the Gauss3D step and for the free boundary conditions are also shown. The free boundary condition data clearly deviate from the other data.

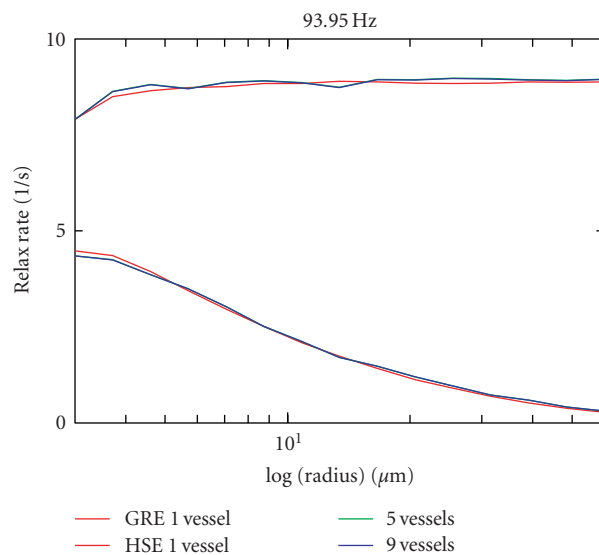


FIGURE 7: $R2/R2^*$ relaxation rates (in s^{-1}) shown for 5 vessels (central vessel and 4 next neighbors), respectively, shown for 9 vessels (8 next neighbors) versus data for one single vessel. All neighbor vessels possess the same direction as the central vessel.

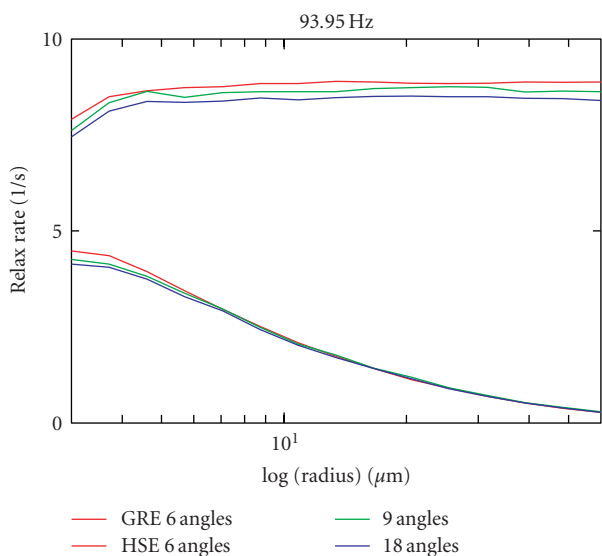


FIGURE 6: $R2/R2^*$ relaxation rates (in s^{-1}) shown for 9 angles and 18 angles compared to the data for 6 angles between the exterior field and the vessel direction.

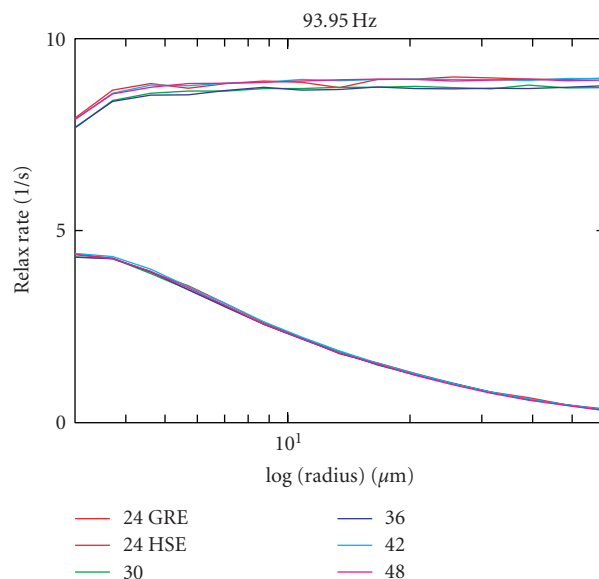


FIGURE 8: $R2/R2^*$ relaxation rates (in s^{-1}) shown for the computational set up with edge lengths of the computational cell of 24, 30, 36, 42, and 48 mean spin-to-spin distances along each edge, corresponding to 24^3 , 30^3 , 36^3 , 42^3 , and 48^3 spins in each computational cell.

5. DISCUSSION

When compared to lower field strengths, the maxima of the spin-echo decay were found to be shifted to lower radii. A set-up with too few angles as well as the use of free boundary conditions introduces errors and therefore should be avoided. All other parameters (time-step, number of protons, and influence of neighboring vessels of the same orientation,

choice of the MC step model used) did not influence the results in our computations.

The current loop approach according to Biot Savart proved the use of the dipole formulae for a finite voxel element to be correct [2]. The plot of the field distribution of an infinite vessel is in agreement with the field distribution of a very long discretized vessel. However, we found that results for a discretized cylinder slightly deviate from the results for

an infinitely long cylinder. For consistency, we show only results obtained for the infinite cylinder in the present work. Moreover, the CPMG decay experiment showed that our diffusion modeling works quite well for all MC step methods investigated.

As discussed by Ogawa et al. [5], at the limit of infinite numbers of spins and time steps, the signal $S(\theta)$ in (6) would be real. However, because we use a finite number of proton spins, there is a residual complex part of the signal. In (6), we forced S to be real by taking its absolute value. However, as the number of spins increases, the residual part should diminish and, at the limit of infinite numbers of protons, should vanish.

The precursor modeling approaches according to Balac et al. [10], Bhagwandien et al. [11], Lüdeke et al. [12], and Bakker et al. [13] are all limited in that they rely either on singular analytical solutions for spheres and cylinders, or on complicated procedures such as boundary element methods (BEMs), finite differences (FDs), or finite element methods (FEMs). The dipole model, in contrast, uses arbitrarily chosen elements (discretized to a grid) in combination with simple geometries (spheres, finite cylinders, parallelepipeds). This allows the design of special interventional instruments (e.g., a biopsy needle with markers) and the computation of the decay of the transverse magnetization in “real world” geometry as in a trabecular bone model, or in a vessel network to model signal decay in brain parenchyma. Branches of vessels might be simulated using our model. Use of analytic field distributions remains possible, thereby allowing modeling similar to Boxerman et al. [7], Ogawa et al. [5], Kennan et al. [6], or Fujita [8].

Discretization of the susceptibility distribution can be made more precise than the mean distance between protons by introducing distance factors [14]. An estimate of arbitrarily high resolution can then be achieved by Richardson Extrapolation [9].

Intra- and extravascular pools were separated by a routine which tests whether a spin is intra- or extravascular. The same routine can be used to detect the transgression of a boundary, and in the case of impenetrable vessel walls, the diffusion step can then be rejected until a transgression-free step has been attained. This is achieved by testing whether a spin was extravascular before the MC step but becomes intravascular after it, or vice versa. Actually, vessel walls are to be regarded as impenetrable, because exchange rates are much longer (typically 500 milliseconds) than TE (typically 100 milliseconds) as discussed in Fisel et al. [3], and in Boxerman et al. [7]. Using a rejection with probability P (drawn from a random series), vessel walls might be modeled as partially penetrable. Spins belonging to the intravascular pool are not considered to contribute to the BOLD signal.

The boundaries of the computational domain might be treated as periodical boundary conditions, reflection of spins at the boundaries or by no conditions at all. However, we observed that tests with such penetrable boundaries (also called “free boundary conditions”) lead to slightly false results.

Let us summarize an important, specific finding revealed in Figure 4 of Section 3. At high field strength (9.4 T), spin-

echo imaging is especially sensitive at about $3\ \mu\text{m}$ radii. The maximum of the spin-echo decay is shifted to lower radii than with lower field strengths. This makes spin-echo imaging especially sensitive to small vessels and capillaries.

The computation with 18 angles revealed a source of discretization error. The 6 angles used regularly in our computations essentially yield only an approximate result. However, since the effort to compute with 18 angles is 3 times greater, we have restricted our analysis to 6 angles. One should bear in mind that this leads to a (somehow limited and therefore minor) error in $R2/R2^*$. Moreover, we found that placing vessels in the next 6 or 9 neighbor volumes does not change the result. Vessels with orientations different from the orientation of the central vessel in the next neighbor volumes have not been investigated and are left for future work.

From 24^3 protons on, the result does not change significantly with increasing numbers of protons. However, to obtain smoother curves (less numerical noise due to a limited number of protons), computations might be repeated using different random initializations for the MC step procedure. Computing time largely depends on the hardware resources available. For the computations with TE = 40 milliseconds in steps of 10 microseconds, computing the complete parameter-space for one random series initialization value with 24^3 protons took approximately 8 days on a Pentium machine with a clock rate of 1.8 GHz.

The model might be further improved by introducing Bloch's equations instead of considering a constant transverse magnetization. Pulses and gradients can then be simulated to model a real pulse sequence with all its implications regarding magnetization. The diffusion constant might also be replaced by a diffusion tensor, making the treatment of problems based on diffusion anisotropy possible.

REFERENCES

- [1] B. E. Hoppel, R. M. Weisskoff, K. R. Thulborn, J. B. Moore, K. K. Kwong, and B. R. Rosen, “Measurement of regional blood oxygenation and cerebral hemodynamics,” *Magnetic Resonance in Medicine*, vol. 30, no. 6, pp. 715–723, 1993.
- [2] B. M. Müller-Bierl, H. Graf, U. Lauer, G. Steidle, and F. Schick, “Numerical modeling of needle tip artifacts in MR gradient echo imaging,” *Medical Physics*, vol. 31, no. 3, pp. 579–587, 2004.
- [3] C. R. Fisel, J. L. Ackerman, R. B. Buxton, et al., “MR contrast due to microscopically heterogeneous magnetic susceptibility: numerical simulations and applications to cerebral physiology,” *Magnetic Resonance in Medicine*, vol. 17, no. 2, pp. 336–347, 1991.
- [4] R. M. Weisskoff, C. S. Zuo, J. L. Boxerman, and B. R. Rosen, “Microscopic susceptibility variation and transverse relaxation: theory and experiment,” *Magnetic Resonance in Medicine*, vol. 31, no. 6, pp. 601–610, 1994.
- [5] S. Ogawa, R. S. Menon, D. W. Tank, et al., “Functional brain mapping by blood oxygenation level-dependent contrast magnetic resonance imaging. A comparison of signal characteristics with a biophysical model,” *Biophysical Journal*, vol. 64, no. 3, pp. 803–812, 1993.
- [6] R. P. Kennan, J. Zhong, and J. C. Gore, “Intravascular susceptibility contrast mechanisms in tissues,” *Magnetic Resonance in Medicine*, vol. 31, no. 1, pp. 9–21, 1994.

-
- [7] J. L. Boxerman, L. M. Hamberg, B. R. Rosen, and R. M. Weisskoff, "MR contrast due to intravascular magnetic susceptibility perturbations," *Magnetic Resonance in Medicine*, vol. 34, no. 4, pp. 555–566, 1995.
- [8] N. Fujita, "Extravascular contribution of blood oxygenation level-dependent signal changes: a numerical analysis based on a vascular network model," *Magnetic Resonance in Medicine*, vol. 46, no. 4, pp. 723–734, 2001.
- [9] W. H. Press, S. A. Teukolsky, W. T. Vetterling, and B. P. Flannery, *Numerical Recipes in C++. The Art of Scientific Computing*, Cambridge University Press, Cambridge, UK, 2nd edition, 2002.
- [10] S. Balac, G. Caloz, G. Cathelineau, B. Chauvel, and J. D. de Certaines, "Integral method for numerical simulation of MRI artifacts induced by metallic implants," *Magnetic Resonance in Medicine*, vol. 45, no. 4, pp. 724–727, 2001.
- [11] R. Bhagwandien, R. van Ee, R. Beersma, C. J. G. Bakker, M. A. Moerland, and J. J. W. Lagendijk, "Numerical analysis of the magnetic field for arbitrary magnetic susceptibility distributions in 2D," *Magnetic Resonance Imaging*, vol. 10, no. 2, pp. 299–313, 1992.
- [12] K. M. Lüdeke, P. Röschmann, and R. Tischler, "Susceptibility artefacts in NMR imaging," *Magnetic Resonance Imaging*, vol. 3, no. 4, pp. 329–343, 1985.
- [13] C. J. G. Bakker, R. Bhagwandien, M. A. Moerland, and M. Fuderer, "Susceptibility artifacts in 2DFT spin-echo and gradient-echo imaging: the cylinder model revisited," *Magnetic Resonance Imaging*, vol. 11, no. 4, pp. 539–548, 1993.
- [14] B. M. Müller-Bierl, H. Graf, P. L. Pereira, and F. Schick, "Numerical simulations of intra-voxel dephasing effects and signal voids in gradient echo MR imaging using different sub-grid sizes," *Magnetic Resonance Materials in Physics, Biology and Medicine*, vol. 19, no. 2, pp. 88–95, 2006.

Research Article

Total Variation Regularization of Matrix-Valued Images

Oddvar Christiansen,¹ Tin-Man Lee,² Johan Lie,¹ Usha Sinha,² and Tony F. Chan³

¹Department of Mathematics, Faculty of Mathematics and Natural Sciences, University of Bergen, 5008 Bergen, Norway

²Medical Imaging Informatics Group, Department of Radiological Sciences, University of California, Los Angeles, CA 90024, USA

³Division of Physical Sciences, College of letters science, University of California, Los Angeles, CA 90095, USA

Received 30 October 2006; Accepted 13 March 2007

Recommended by Hongkai Zhao

We generalize the total variation restoration model, introduced by Rudin, Osher, and Fatemi in 1992, to matrix-valued data, in particular, to diffusion tensor images (DTIs). Our model is a natural extension of the color total variation model proposed by Blomgren and Chan in 1998. We treat the diffusion matrix D implicitly as the product $D = LL^T$, and work with the elements of L as variables, instead of working directly on the elements of D . This ensures positive definiteness of the tensor during the regularization flow, which is essential when regularizing DTI. We perform numerical experiments on both synthetical data and 3D human brain DTI, and measure the quantitative behavior of the proposed model.

Copyright © 2007 Oddvar Christiansen et al. This is an open access article distributed under the Creative Commons Attribution License, which permits unrestricted use, distribution, and reproduction in any medium, provided the original work is properly cited.

1. INTRODUCTION

Image processing methods using variational calculus and partial differential equations (PDEs) have been popular for a long time in the image processing research community. Among popular PDE methods are the anisotropic diffusion method proposed by Perona and Malik [1], the total variation method introduced by Rudin et al. [2], and various methods related to these [3–7]. Many of these methods were originally introduced for scalar-valued (gray-scale) images, and were later generalized to vector-valued (color) images.

During the last decade or so, a new magnetic resonance modality called diffusion tensor imaging (DTI) has been extensively studied [8–13]. Using DTI, it is possible to study anatomical structures like the nerve fibers in the human brain noninvasively. The DTI images are matrix valued. In each voxel of the imaging domain, we construct a *diffusion tensor* (i.e., *diffusion matrix*) D based on a series of K direction-specific MR measurements $\{S_k\}_{k=1}^K$. The matrix $D \in R^{3 \times 3}$ is a symmetric, positive definite matrix

$$D = \Lambda V^{-1}, \quad (1)$$

where V is an orthogonal matrix, and Λ is a diagonal matrix with positive elements. We may look at the diffusion matrix as a hyperellipse where the eigenvectors $\{V_i\}_{i=1}^3$ span the ellipsoid, and the corresponding eigenvalues $\{\lambda_i\}_{i=1}^3$ determine the length of each semiaxis (see Figure 1). It is customary to

arrange the eigenvalues in decreasing order. By the diffusion tensor model we assume that the set of images $\{S_k\}_{k=1}^K$ is related to the nonweighted image S_0 by the Stejskal-Tanner equation [14, 15]

$$S_k = S_0 e^{-bg_k^T D g_k}, \quad k = 1, 2, \dots, K. \quad (2)$$

Here $g_k \in R^3$ denotes the direction associated with S_k , and $b > 0$ is a scalar which among other factors depends on the acquisition time and the strength of the magnetic field [16]. Since $D \in R^{3 \times 3}$ is symmetric, it has six degrees of freedom. Thus at least six measurements $\{S_k\}_{k=1}^6$ are required to estimate the tensor, as well as the nonweighted measurement S_0 . The tensor D can be estimated from (2). In the case of more than six measurements S_k , we can estimate D by, for example, a least-squares minimization. From the eigenvalue decomposition of the diffusion tensor, we can reveal properties like the dominant diffusion direction and the anisotropy of diffusing water molecules [17]. This information can be used to construct maps of the anatomy of the brain.

From the developments in DTI, a need for robust regularization methods for matrix-valued images has emerged. As far as the authors are aware of, there exists no state-of-the-art method for regularization of tensor-valued images, although many methods have been proposed [18–21].

All measurements $\{S_k\}_{k=1}^K$ contain noise, which degrades the accuracy of the estimated tensor. Compared with conventional MR, direction-sensitive acquisitions have a lower

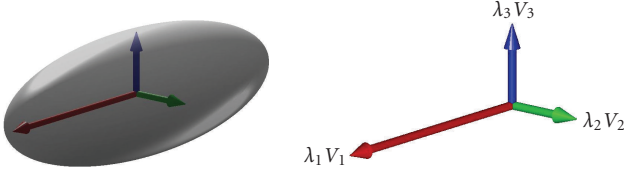


FIGURE 1: The diffusion matrix D can be represented by a diffusion ellipsoid, where the semiaxes are spanned by the eigenvectors $\{V_i\}_{i=1}^3$ of D , and the length of each semiaxis is given by the eigenvalues $\{\lambda_i\}_{i=1}^3$. In this illustration, the diffusion is anisotropic. The principal diffusion direction is along eigenvector V_1 .

signal-to-noise ratio (SNR). Thus the gradient weighted images $\{S_k\}_{k=1}^K$ contain more noise than S_0 . There are several ways to increase the accuracy of the estimated tensor. The most intuitive way is to make an average of a series of repeated measurements. Alternatively, we can increase the number of gradient directions. An obvious disadvantage of both of these approaches is the increased scanner time. Perhaps a better way to improve the quality of the tensor is by postprocessing the data. In this paper, we follow this approach, by introducing a regularization method for tensor-valued data.

Since D models diffusion, regularization methods in DTI must preserve the positive definiteness of D . A positive definite matrix has only positive eigenvalues, which is necessary from the physical modeling perspective. In a minimization method for regularization of the tensor data, one possible way to ensure positive definiteness would be to impose a constraint on the minimization problem. Then the constrained problem would have a solution which is on the manifold of positive definite matrices. Regularization of tensor-valued data constrained to manifolds has been studied during the last couple of years, see [22–24]. We however follow a different strategy. Using essentially the same idea as Wang et al. did in a slightly different setting, we treat D implicitly by writing D as the product $D = LL^T$, where L is a lower triangular matrix [18]. Every symmetric positive definite (SPD) matrix has a factorization on this form. We will in this work develop a regularization method for diffusion tensor images by generalizing methods previously developed for scalar- and vector-valued images [2, 25].

Before we go into details of the proposed method, we briefly introduce the total variation (TV) methods for scalar- and vector-valued images. During the last 15 years or so, TV models have undergone extensive studies, initiated by the work of Rudin, Osher, and Fatemi (ROF) [2].

Define the total variation (TV) seminorm for scalar-valued data as

$$\text{TV}[u] = \int_{\Omega} |\nabla u| dx. \quad (3)$$

Throughout this paper, ∇ denotes the spatial gradient, while $\nabla \cdot$ denotes the divergence operator. In the ROF model, the TV seminorm with an added L_2 fidelity norm is minimized

$$\min_u \left\{ G(u, f, \lambda) = \text{TV}[u] + \frac{\lambda}{2} \|u - f\|_2^2 \right\}. \quad (4)$$

Note that we can write the functional G more abstractly as

$$G(u, f, \lambda) = R(u) + \frac{\lambda}{2} F(u, f), \quad (5)$$

where $R(u)$ is a regularization functional and $F(u, f)$ is a fidelity functional. The regularization term is a geometric functional measuring smoothness of the estimated solution. The fidelity term is a measure of fitness of the estimated solution compared to the input data. It is customary to measure the fidelity in the sense of least squares. Equation (4) has the corresponding Euler-Lagrange equation

$$\partial_u G = -\nabla \cdot \left(\frac{\nabla u}{|\nabla u|} \right) + \lambda(u - f). \quad (6)$$

We can find a minimum of (4) by searching for a steady state of

$$\frac{\partial u}{\partial t} = -\partial_u G, \quad (7)$$

which is the way the ROF model was first formulated [2]. Alternatively, we can directly attack the zero of the Euler-Lagrange equation

$$-\partial_u G = 0, \quad (8)$$

for example, by a fixed-point iteration [26]. This is in general less time consuming than solving the equation using the method of steepest descent, but more tedious to carry out numerically. When we generalize the method to matrix-valued images, we solve the minimization problem by the method of steepest descent. Various methods have been proposed to generalize the ROF model to vector-valued image regularization. Among the successful methods, we find the color TV model developed by Blomgren and Chan [25] and the model by Sapiro [27]. Blomgren and Chan [25] generalized the ROF model to color (vector) image regularization using a set of coupled equations

$$\left\{ \frac{\partial u_i}{\partial t} = \alpha_i \nabla \cdot \left(\frac{\nabla u_i}{|\nabla u_i|} \right) - \lambda(u_i - f_i), \quad i = 1, 2, 3 \right\} \quad (9)$$

with

$$\alpha_i = \frac{\text{TV}[u_i]}{\text{TV}[\mathbf{u}]}, \quad i = 1, 2, 3, \quad (10)$$

$$\text{TV}[\mathbf{u}] = \sqrt{\sum_{i=1}^3 \text{TV}[u_i]^2}.$$

The weight α_i in (9) acts as a coupling between the geometric part of the three image channels. In this work, we extend in a natural way the color TV model of Blomgren and Chan to a matrix TV model. However, the method we propose is not restricted to our choice of regularization functional (TV). For a detailed treatment of TV regularization methods we refer the reader to the recent book by Chan and Shen [5].

In Section 2, we define the minimization problem that we propose to solve, and arrive at the Euler-Lagrange equations

corresponding to this minimization problem. We perform numerical experiments in Section 3, before we finish the paper in Section 4 with a conclusion. Details on the Euler-Lagrange equation and the numerical implementation are given in the appendix at the end of the paper.

2. MINIMIZATION PROBLEM

In this section, we introduce the functional that we minimize in order to regularize tensor-valued data. Let L be a lower triangular matrix. We define D by

$$D = LL^T. \quad (11)$$

This has immediate implications on D : symmetry, positive definiteness, and orthogonality of eigenvectors. These properties are required by the diffusion tensor model. Thus (11) is a natural choice. We define ℓ_{ij} as the element in the i th row and j th column of L . The elements d_{ij} are defined in the same manner.

Let us look at the algebraic equation expressing D as a function of ℓ_{ij} . We derive the expressions for $D \in R^{3 \times 3} \subset \text{SPD}$. We explicitly write out the matrix multiplication (11),

$$D = \begin{pmatrix} \ell_{11}^2 & \ell_{11}\ell_{21} & \ell_{11}\ell_{31} \\ \ell_{11}\ell_{21} & \ell_{21}^2 + \ell_{22}^2 & \ell_{21}\ell_{31} + \ell_{22}\ell_{32} \\ \ell_{11}\ell_{31} & \ell_{21}\ell_{31} + \ell_{22}\ell_{32} & \ell_{31}^2 + \ell_{32}^2 + \ell_{33}^2 \end{pmatrix}. \quad (12)$$

In our proposed model, we solve a minimization problem in terms of ℓ_{ij} . For each unique ℓ_{kl} , we minimize

$$\min_{\ell_{kl}} \left\{ \sqrt{\sum_{ij} \text{TV}[d_{ij}(\ell_{kl})]^2} + \frac{\lambda}{2} \sum_{ij} \|d_{ij} - \hat{d}_{ij}\|_2^2 \right\}, \quad (13)$$

where $\{kl\} \in \{11, 21, 22, 31, 32, 33\}$ and \hat{d}_{ij} denotes the elements of the tensor estimated from the noisy data. As in the scalar model, the functional (13) has the abstract form (5). The scalar ROF ($\text{TV} - L_2$) functional is convex. But when we introduce the factorization (11) into the model, we cannot expect the functional (13) to be convex or even quasiconvex. However, from numerical experiments where we used different (random) initial conditions we ended up with almost exactly the same solution. This means that even though we are not able to prove that the functional is convex, we have indications that it is at least quasiconvex.

We note that minimizing the functional (13) is related to the functional used by Wang et al. [18]. Apart from the fact that they simultaneously estimate and regularize the tensor, there are fundamental differences between our proposed regularization functional and the functional proposed by Wang et al. Even though we represent the diffusion matrix on the form of a Cholesky factorization, we regularize the elements of the full diffusion tensor D , while Wang et al. regularize the elements of the lower triangular matrix L . Intuitively, regularizing the elements of D is more direct than regularizing the elements of L . We highlight the difference between Wang's method and our proposed method by a numerical simulation in a simplified setting in Section 3. In addition, the method proposed in this paper has a coupling between all

elements of D in the regularization PDE, while the method proposed by Wang et al. does not have such a coupling between the channels.

We also note that the functional (13) is chosen mainly because of the good properties of the corresponding scalar- and vector-valued functionals [2, 25], with edge preservation as the most prominent property. Depending on the application at hand, other functionals might be considered as alternatives. The framework developed in this paper is however applicable for other regularization functionals as well.

2.1. Euler-Lagrange equations

In this section, we derive the Euler-Lagrange equations corresponding to the minimization functional (13). We first differentiate the fidelity functional

$$\begin{aligned} \frac{\partial F}{\partial \ell_{kl}} &= \frac{\partial}{\partial \ell_{kl}} \sum_{ij} \|d_{ij} - \hat{d}_{ij}\|_2^2 \\ &= 2 \sum_{ij} (d_{ij} - \hat{d}_{ij}) \frac{\partial d_{ij}}{\partial \ell_{kl}}. \end{aligned} \quad (14)$$

We differentiate D with respect to ℓ_{kl} , for example

$$\frac{\partial D}{\partial \ell_{11}} = \begin{pmatrix} 2\ell_{11} & \ell_{21} & \ell_{31} \\ \ell_{21} & 0 & 0 \\ \ell_{31} & 0 & 0 \end{pmatrix}. \quad (15)$$

The other derivatives follow the same pattern. Writing out (14), we find the derivative of the fidelity functional,

$$\begin{aligned} \frac{\partial F}{\partial \ell_{kl}} &= 2 \left[(d_{11} - \hat{d}_{11}) \frac{\partial d_{11}}{\partial \ell_{kl}} + 2(d_{21} - \hat{d}_{21}) \frac{\partial d_{21}}{\partial \ell_{kl}} \right. \\ &\quad + (d_{22} - \hat{d}_{22}) \frac{\partial d_{22}}{\partial \ell_{kl}} + 2(d_{31} - \hat{d}_{31}) \frac{\partial d_{31}}{\partial \ell_{kl}} \\ &\quad \left. + 2(d_{32} - \hat{d}_{32}) \frac{\partial d_{32}}{\partial \ell_{kl}} + (d_{33} - \hat{d}_{33}) \frac{\partial d_{33}}{\partial \ell_{kl}} \right], \end{aligned} \quad (16)$$

where $\{d_{ij}\}_{i=1,j=1}^3$ denote the elements of the matrix D . We differentiate the regularization functional in (13). Define the total variation norm of a matrix $D \in R^3 \times R^3$ as

$$\begin{aligned} \text{TV}[D] &= \left(\text{TV}[d_{11}(\ell_{ij})]^2 + 2\text{TV}[d_{21}(\ell_{ij})]^2 \right. \\ &\quad + \text{TV}[d_{22}(\ell_{ij})]^2 + 2\text{TV}[d_{31}(\ell_{ij})]^2 \\ &\quad \left. + 2\text{TV}[d_{32}(\ell_{ij})]^2 + \text{TV}[d_{33}(\ell_{ij})]^2 \right)^{1/2}. \end{aligned} \quad (17)$$

This is a straightforward generalization of the total variation norm of a vector [25].

Using the chain rule, we find the derivatives of the regularization functional to be

$$\frac{\partial R}{\partial \ell_{kl}} = - \sum_{ij} \alpha_{ij} \nabla \cdot \left(\frac{\nabla d_{ij}}{|\nabla d_{ij}|} \right) \frac{\partial d_{ij}}{\partial \ell_{kl}}, \quad (18)$$

with

$$\alpha_{ij} = \frac{\text{TV}[d_{ij}]}{\text{TV}[D]}. \quad (19)$$

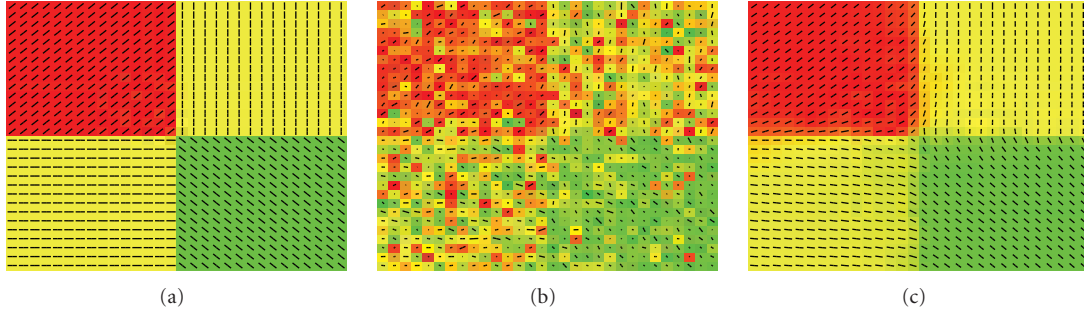


FIGURE 2: A synthetically produced purely anisotropic tensor field with four distinct regions is degraded with normally distributed noise. The noisy field is then processed with our proposed method: (a) the clean vector field D_0 ; (b) the noisy field \hat{D} ; (c) the recovered field D .

Note here that this derivative is essentially similar to the derivative in the color TV model of Blomgren and Chan [25], but with the important difference that we represent the diffusion matrix by its Cholesky factors.

In the next section, we perform numerical simulations using the method proposed in this paper. We give more details on the Euler-Lagrange equations in the appendix, which also contains some details on the numerical implementation of the model.

3. NUMERICAL EXPERIMENTS

In this section we perform numerical experiments on synthetically constructed tensor fields and real tensor fields from a human brain. The numerical implementation of the method is briefly discussed in the appendix.

For the synthetical fields we have constructed clean tensor fields, which are degraded with noise with a prior known distribution. Thus, we are able to measure how well the method performs on synthetical data. For the real human brain DTI, the “true” solution is of course not known in advance. In this case, we measure the performance of the method in terms of a reference solution where a large series of acquisitions are averaged. This is explained in detail in Section 3.3. For the numerical implementation of the method and some of the visualizations, we have used Matlab [28].

3.1. Synthetical tensor fields

In the first numerical experiment, displayed in Figure 2, we test the performance of the proposed method on a simple tensor field. This field is mapping a square domain $\Omega \subset \mathbb{R}^2$, with four distinct regions, to $\mathbb{R}^{2 \times 2}$. We construct the clean tensor-valued data by prescribing the eigenvalues and corresponding eigenvectors. The values of each element of L is in the range $[0, 1]$. Then we add normally distributed noise $\eta(\sigma)$ to each element of the Cholesky factorization of the matrix, that is, $\hat{L} = L + \eta(\sigma)$. Finally, the degraded diffusion tensor is constructed by $\hat{D} = \hat{L}\hat{L}^T$. The noise levels in the simulations in Figures 2 and 4 are given by $\sigma = 0.35$ and $\sigma = 0.25$, respectively. The time step is $\Delta t = 0.001$. Note that the discontinuities in the data are preserved in the solution, that

is, the edge preserving property of scalar and vector-valued TV flow is kept in the proposed matrix-valued flow. In the first example, the diffusion is anisotropic in the whole domain. To show how the proposed method differentiates between isotropic and anisotropic regions we show a similar example where one of the four regions is interchanged with an isotropic region. The isotropic region is constructed by considering the orthogonal matrix Q from the QR factorization of a random 2×2 matrix. The columns of the matrix Q are considered to be the eigenvectors of the diffusion tensor. We specify two random numbers in the range $[0, 1]$ as the eigenvalues of the tensor. Thus the diffusion is random in the isotropic region. As we can observe from these two numerical examples on synthetical data, edges are preserved in the regularized images. We observe that even when the noise level is high, we are able to reconstruct an image which is close to the true noise-free image.

From these numerical experiments on synthetical data we see that the proposed method gives encouraging results. Similarly as in the scalar- and vector-valued settings, edges are well preserved. We further investigate the edge preservation in the next experiment.

3.2. Qualitative experiments

To highlight the qualitative differences between regularizing the elements of the tensor D and the elements of the Cholesky factors L , we have constructed a simple numerical example in 1D. We have removed the fidelity measure from the model, thus the method is in this setting merely a diffusion filter. Thus we have simplified the model in such a way that we can study the qualitative behavior of the two regularization filters in the same setting (see Figure 3). From this example, we clearly see that when we regularize D the edges are better preserved than when we regularize L . Note that Wang et al. regularize the Cholesky factors [18].

We also present a numerical example in 2D where we solve the PDEs first as an uncoupled system, that is, by employing the weighting factors $\alpha_{ij} = 1$, and then as a coupled system where we use the weighting factors from (10). We denote the clean field by D , the noisy field by \hat{D} , the field regularized with the uncoupled system by D^u and the field regularized with the coupled system by D^c . In Figures 5(a)–5(d),

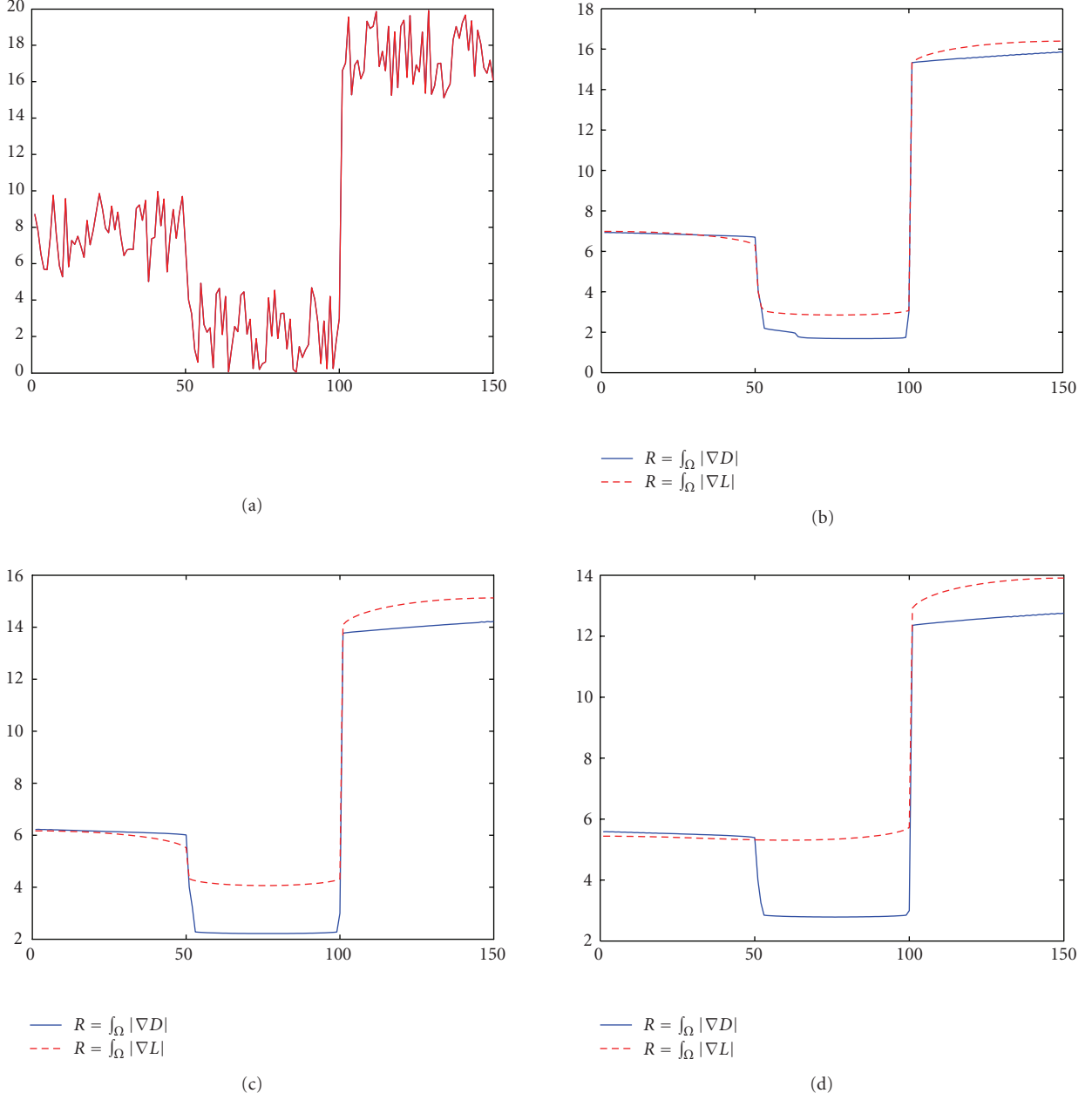


FIGURE 3: A simple 1D example showing the qualitative behavior of the model for regularizers $\int_{\Omega} |\nabla L|$ and $\int_{\Omega} |\nabla D|$. The noisy signal in (a) is processed with both flows. Subfigures (b), (c), and (d) are snapshots during the flow at the three times $t = 8$, $t = 16$, and $t = 24$.

we show the elements D_{11} , \hat{D}_{11} , D_{11}^u , and D_{11}^c , respectively. Subindexes denote the elements of the matrix field. Figures 5(e)–5(h) show the elements D_{12} , \hat{D}_{12} , D_{12}^u , and D_{12}^c , while Figures 5(i)–5(l) show the element D_{22} , \hat{D}_{22} , D_{22}^u , and D_{22}^c . From Figure 5, we observe that the uncoupled system does not discriminate the noise from the weak signal. The coupled system on the other hand better discriminates the noise from the weak signal. A similar 1D example is shown by Blomgren and Chan using the color TV model [25].

In the next section, we go one step further and process real human brain DTMRI.

3.3. Human brain DTMRI

We also perform numerical experiments on DTMRI acquisitions of a healthy human brain from a volunteer. The human subject data is acquired using a 3.0 T scanner (Magnetom Trio, Siemens Medical Solutions, Erlangen, Germany) with an 8-element head coil array and a gradient subsystem with the maximum gradient strength of 40 mT/m and maximum slew rate of 200 mT/m/ms. The DTI data is based on spin-echo single-shot EPI acquired utilizing generalized autocalibrating partially parallel acquisitions (GRAPPA)

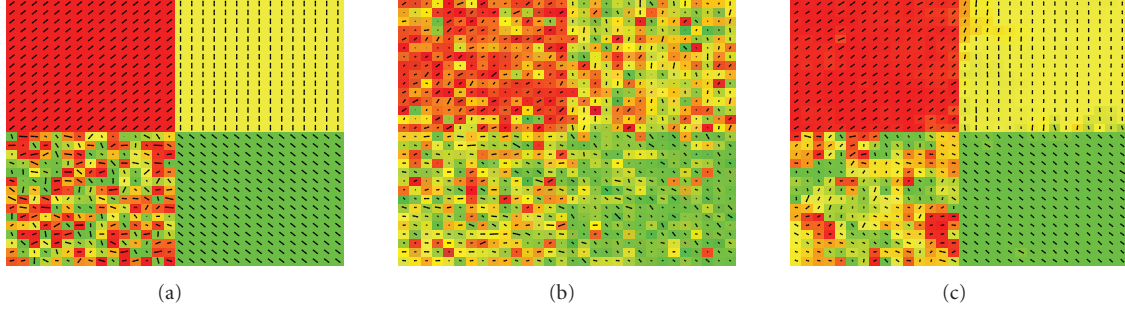


FIGURE 4: Visualization of (a) the true vector field, (b) the noisy field, and (c) the recovered field. In this example, the tensor field is isotropic in the lower-left corner, anisotropic in the other parts.

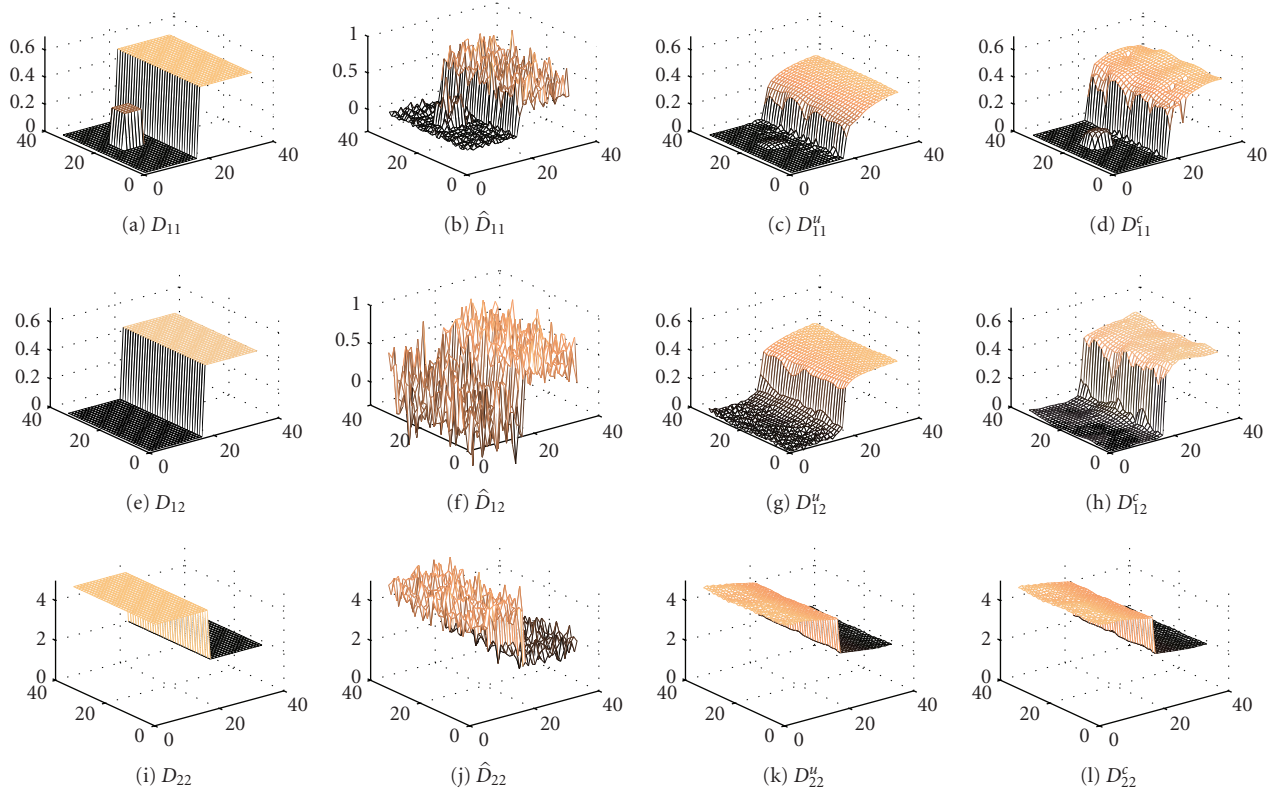


FIGURE 5: A noisy 2D tensor field is regularized. In this example, the smallest parts of the signal are not easily discriminated from the noise.

technique with acceleration factor of 2 and 64 reference lines. The DTI acquisition consists of one baseline EPI and six diffusion weighted images (b-factor of 1000 s/mm^2) along the following gradient directions: $G_1 = 1/\sqrt{2}[1, 0, 1]^T$, $G_2 = 1/\sqrt{2}[-1, 0, 1]^T$, $G_3 = 1/\sqrt{2}[0, 1, 1]^T$, $G_4 = 1/\sqrt{2}[0, 1, -1]^T$, $G_5 = 1/\sqrt{2}[1, 1, 0]^T$, $G_6 = 1/\sqrt{2}[1, 1, 0]^T$. Each acquisition has the following parameters: TE/TR/averages is 91 ms/10000 ms/2, FOV is $256 \text{ mm} \times 256 \text{ mm}$, slice thickness/gap is 2 mm/0 mm, acquisition matrix is 192×192 pixels, and partial Fourier encoding is 75%.

For validation of the proposed regularization method on real data, we construct a reference solution D^* by averaging 18 replications. Each replication consists of six-direction

weighted and one nonweighted acquisitions. This reference solution is compared to solutions where averages of two, four, and six replications are postprocessed with the proposed regularization method. As a measure of the distance between the reference solution and the processed solution, we use the following metric:

$$\begin{aligned}
 m(D, D^*) = & \left([d_{11} - d_{11}^*]^2 + 2[d_{12} - d_{12}^*]^2 \right. \\
 & + 2[d_{13} - d_{13}^*]^2 + [d_{22} - d_{22}^*]^2 \\
 & \left. + 2[d_{23} - d_{23}^*]^2 + [d_{33} - d_{33}^*]^2 \right)^{1/2}.
 \end{aligned} \tag{20}$$

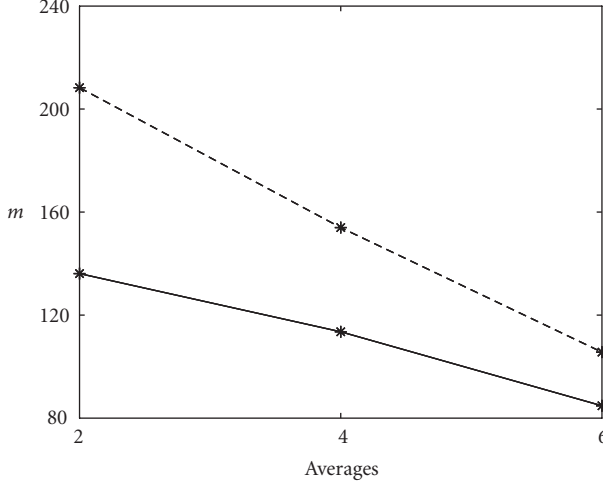


FIGURE 6: Comparison of $m(D, D^*)$ for the original tensors (dashed) and the regularized tensors (solid) versus the number of averaged acquisitions.

TABLE 1: The distance $m(D, D^*)$ of the regularized and the nonregularized tensor fields from the numerical examples shown in Figures 7 and 8.

Averages	λ	Reg. $m(D, D^*)$	Nonreg. $m(D, D^*)$
2	9	136.1	208.3
4	13	113.5	154
6	19	84.8	105.6

TABLE 2: The average deviation angle (ADA) of the noisy data, the processed data (two different regularization parameters), and the reference data.

Data(↓) ADA (→)	Global	ROI 1	ROI 2	ROI 3
Noisy (4 avgs.)	12.32	32.92	41.02	42.87
Denoised, $\lambda = 13$	6.27	11.77	31.50	25.27
Denoised $\lambda = 20$	7.58	13.34	32.88	28.86
Clean image (18 avgs.)	6.65	18.23	24.80	24.80

For each simulation, we report the regularization parameter λ and the metric $m(\cdot, \cdot)$ in Table 1 and in Figure 6. We display the result before and after applying the proposed method on real DTMRI data in Figures 7 and 8. In the figures, we display a 2D slice of an RGB direction encoded fractional anisotropy (FA) measure defined by

$$FA = \sqrt{\frac{3}{2} \frac{(\bar{\lambda} - \lambda_1)^2 + (\bar{\lambda} - \lambda_2)^2 + (\bar{\lambda} - \lambda_3)^2}{\lambda_1^2 + \lambda_2^2 + \lambda_3^2}}, \quad (21)$$

where $\bar{\lambda} = (\lambda_1 + \lambda_2 + \lambda_3)/3$. The FA measure is direction-encoded as described by Pajevic and Pierpaoli [29]. We use the DTMRI software DTIStudio to construct the visualizations [30]. In the figures, we show the color-coded FA.

The noise level is different for each simulation due to the varying number of acquisitions. Consequently, the regularization parameter λ is different for each simulation. However, for clinical applications, the regularization parameter is estimated once for each imaging protocol. When this is done, the same regularization parameter can be used for subsequent applications of the same imaging protocol.

3.4. Human brain ROI study

Since our algorithm regularizes the tensor field, we focus on the evaluation of the tensor field, and the derived scalar FA map. However, we note that from the processed tensor field, we may reconstruct the corresponding diffusion weighted images $\{S_i\}_{i=1}^6$ by (2). There are obvious visual improvements in the processed diffusion weighted images compared to the noisy diffusion weighted images. Edges are preserved and noise is suppressed. Quantitatively, the mean and standard deviation at certain homogeneous regions of interests (ROIs) show significant improvements. We will now assess the visual and quantitative improvements in terms of the denoised tensors.

For qualitative evaluation, we select three regions of interest (ROIs) from one slice of the acquired images, with a 15-by-15 voxel size. We plot the 2D projection of the eigenvector corresponding to the major eigenvalue in Figure 9. From Figure 9, we can clearly see that our method preserves discontinuities (edges) in the tensor field, while it smooths the tensor field in homogeneous regions. The denoised tensor field from the 4-average acquisition is close to the tensor field obtained from the 18-average acquisition.

For quantitative measures, we use the average deviation angle (ADA) index of Chen and Hsu to measure if the tensor field undergoes gradual changes or sharp turns [21]. The PDE filtering is performed after the tensors are computed, so we use the angle deviation in adjacent voxels as a measure of its performance instead of normalized magnitude of diffusion tensor error (NMTE) index [21]. Denote the eigenvector corresponding to the largest eigenvalue by V^* . Define the ADA by

$$ADA = \frac{\Delta\alpha_{i-1} + \Delta\alpha_{i+1} + \Delta\alpha_{j-1} + \Delta\alpha_{j+1} + \Delta\alpha_{k-1} + \Delta\alpha_{k+1}}{6}, \quad (22)$$

where, for example, $\Delta\alpha_{i-1} = \cos^{-1}(|(V_{ijk}^*, V_{i-1jk}^*)|)$. We note that we use the absolute value of the inner product (\cdot, \cdot) to accommodate antisense directional vectors. A small change in direction from one voxel to its neighbor gives a small ADA, while a large change in direction gives a large ADA.

After masking the background, we compute the average ADA within the brain, and call it the global ADA. From Table 2, we see that the global ADA of the data is reduced from 12.31 to 6.27 by the denoising algorithm, whereas the 18-average clean data has an ADA of 6.65. With a higher data fidelity requirement (when λ is larger, e.g., 20), the smoothing is not very aggressive and the ADA is not as close as when $\lambda = 13$. When λ is less than 13 (data not shown here), the smoothing is excessive and the ADA values fall well below the

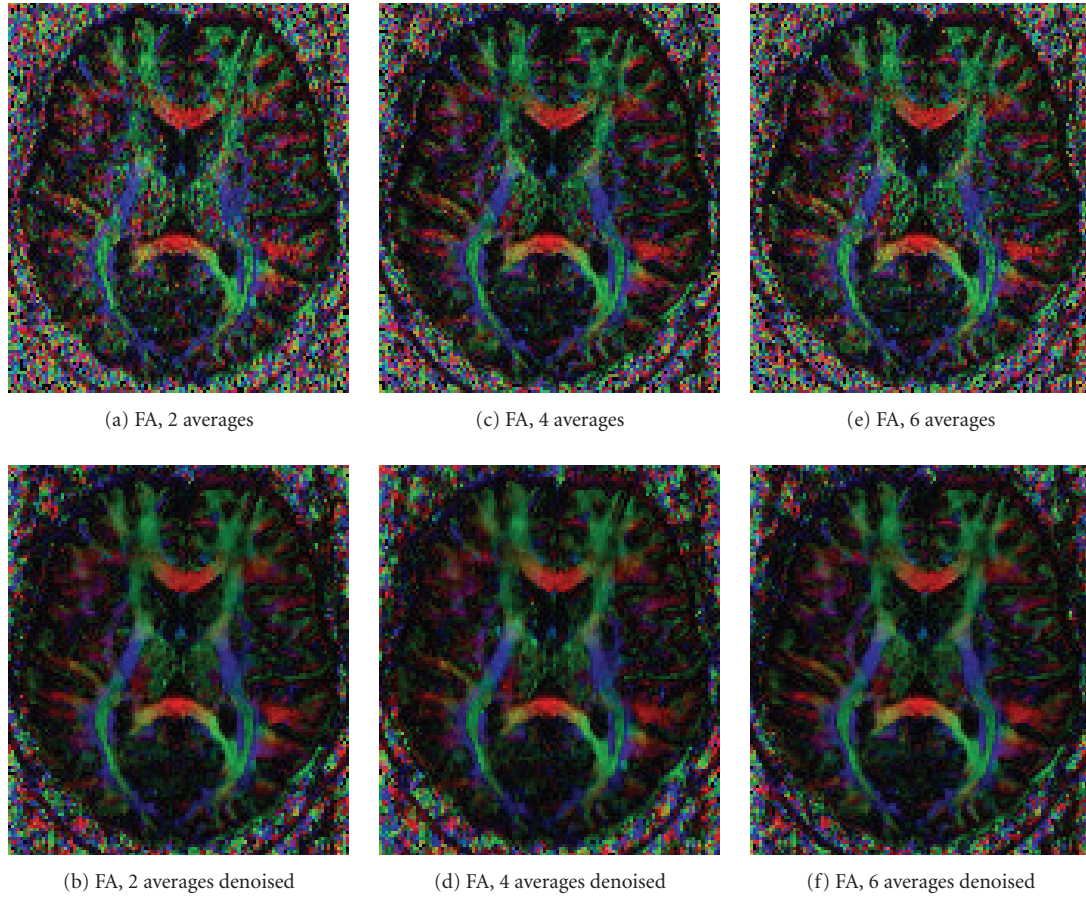


FIGURE 7: Color-coded fractional anisotropy (FA) maps constructed from averages of two (a), four (c), and six (e) acquisitions, and the corresponding denoised maps (b), (d), and (f).

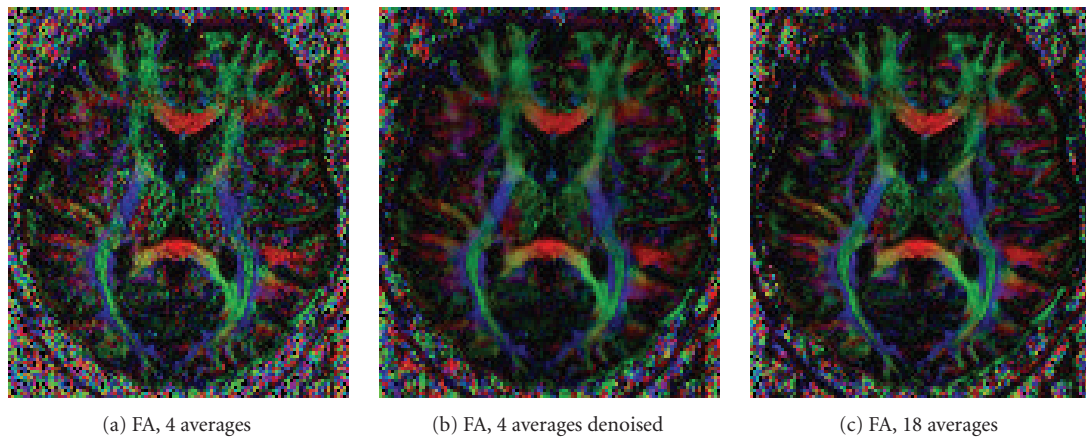


FIGURE 8: The noisy 4-average acquisition (a) is compared with the denoised acquisition (b) and a reference solution at 18 averages.

ADA of the 18-average data. From this information, we conclude that for the current acquisition data, $\lambda = 13$ is the best choice. The ADA at selected ROIs is larger than the global ADA because in those regions, there are obvious edges that contributed to the relatively large ADA values. Compared

with the noisy 4-average data, the denoised data show significant improvements. Using the regularization parameter $\lambda = 13$, the ADA is close to the ADA of the 18-average data. The ADAs of all the ROIs are however reduced compared to the noisy data.

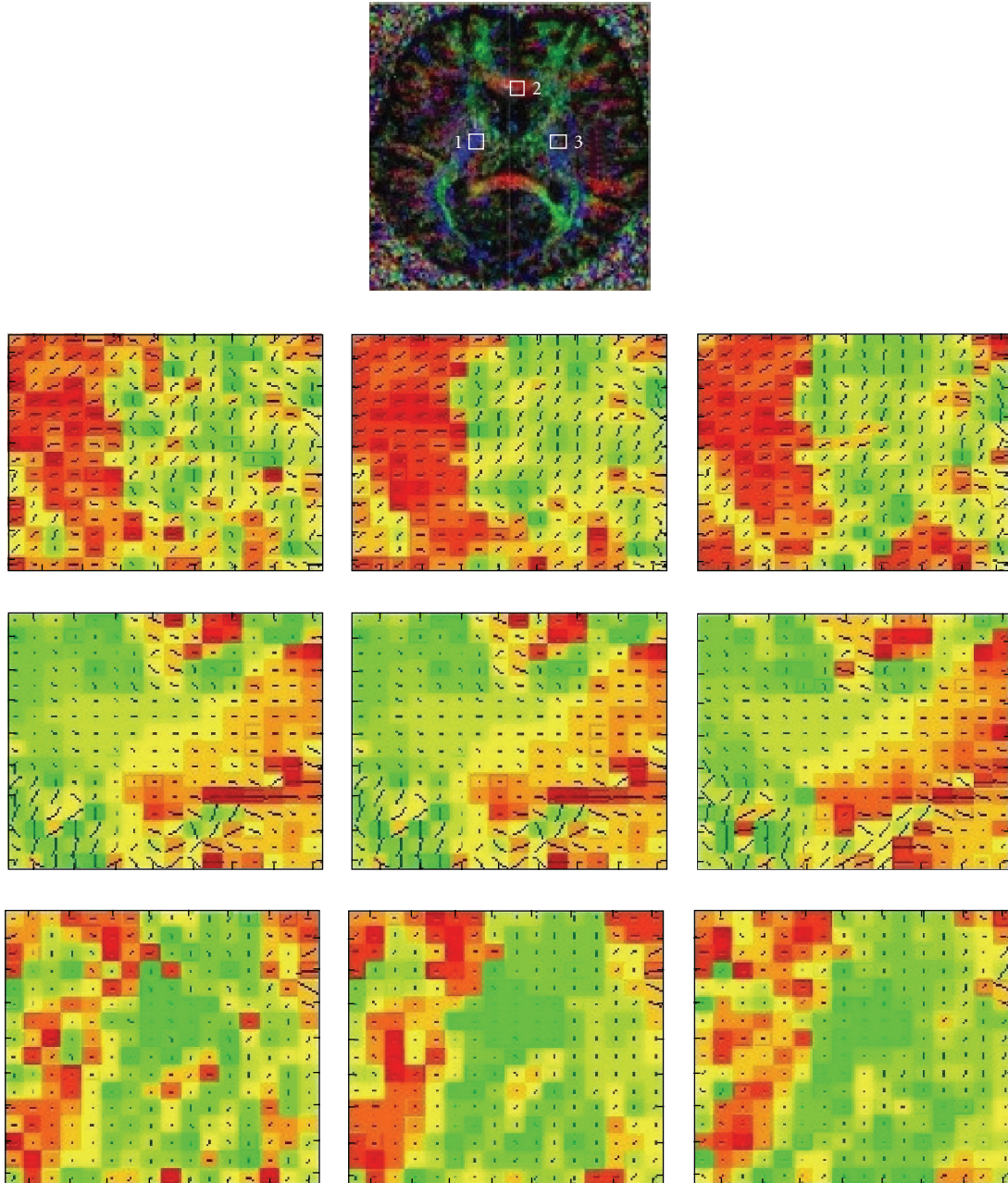


FIGURE 9: ROI study. Top image shows the ROIs that we use. The second row from left to right: the noisy (4-average) data, denoised data with $\lambda = 13$, and clean (18-average) data of ROI 1. The third row from left to right: the noisy (4-average) data, denoised data with $\lambda = 13$, and clean (18-average) data of ROI 2. The fourth row from left to right: the noisy (4-average) data, denoised data with $\lambda = 13$, and clean (18-average) data of ROI 3.

4. CONCLUSION

In this work, we have generalized the color TV regularization method of Blomgren and Chan [25] to yield a structure preserving regularization method for matrix-valued images. We have shown that the proposed method performs well as a regularization method with the important property of preserving both edges in the data and positive definiteness of the diffusion tensor. Numerical experiments on synthetically

produced data and real data from DTI of a human brain of a healthy volunteer indicate good performance of the proposed method.

ACKNOWLEDGMENTS

The authors would like to thank Dr. Siamak Ardekani at UCLA for kindly providing the DRMRI data used in this project. We would also like to thank Dr. Jerome Darbon for

his very useful comments on the paper. The work of Johan Lie has been funded by the Norwegian Research Council, Project BeMatA. The work of Tony F. Chan and Tin-Man Lee has been funded by NSF, ONR, and NIH.

APPENDIX

A. EULER-LAGRANGE EQUATION AND NUMERICAL IMPLEMENTATION

In this appendix, we explicitly write out the Euler-Lagrange equations corresponding to the minimization functional (13). In addition, the numerical scheme used in the simulations in Section 3 is briefly discussed.

Using the short-hand notation

$$p(x_{ij}) = \alpha_{ij} \nabla \cdot \left(\frac{\nabla x_{ij}}{|\nabla x_{ij}|} \right), \quad (\text{A.1})$$

we can write out the derivatives of R and F as

$$\begin{aligned} \frac{\partial R}{\partial \ell_{11}} &= 2(\ell_{11} p(\ell_{11}^2) + \ell_{21} p(\ell_{11} \ell_{21}) + \ell_{31} p(\ell_{11} \ell_{31})), \\ \frac{\partial R}{\partial \ell_{21}} &= 2(\ell_{11} p(\ell_{11} \ell_{21}) + \ell_{21} p(\ell_{21}^2 + \ell_{22}^2) \\ &\quad + \ell_{31} p(\ell_{21} \ell_{31} + \ell_{22} \ell_{32})), \\ \frac{\partial R}{\partial \ell_{22}} &= 2(\ell_{22} p(\ell_{21}^2 + \ell_{22}^2) + \ell_{32} p(\ell_{21} \ell_{31} + \ell_{22} \ell_{32})), \\ \frac{\partial R}{\partial \ell_{31}} &= 2(\ell_{11} p(\ell_{11} \ell_{31}) + \ell_{21} p(\ell_{21} \ell_{31} + \ell_{22} \ell_{32}) \\ &\quad + \ell_{31} p(\ell_{31}^2 + \ell_{32}^2 + \ell_{33}^2)), \\ \frac{\partial R}{\partial \ell_{32}} &= 2(\ell_{22} p(\ell_{21} \ell_{31} + \ell_{22} \ell_{32}) + \ell_{32} p(\ell_{31}^2 + \ell_{32}^2 + \ell_{33}^2)), \\ \frac{\partial R}{\partial \ell_{33}} &= (2\ell_{33} p(\ell_{31}^2 + \ell_{32}^2 + \ell_{33}^2)), \\ \frac{\partial F}{\partial \ell_{11}} &= 4[(d_{11} - \hat{d}_{11})\ell_{11} + (d_{21} - \hat{d}_{21})\ell_{21} + (d_{31} - \hat{d}_{31})\ell_{31}], \\ \frac{\partial F}{\partial \ell_{21}} &= 4[(d_{21} - \hat{d}_{21})\ell_{11} + (d_{22} - \hat{d}_{22})\ell_{21} + (d_{32} - \hat{d}_{32})\ell_{31}], \\ \frac{\partial F}{\partial \ell_{22}} &= 4[(d_{22} - \hat{d}_{22})\ell_{22} + (d_{32} - \hat{d}_{32})\ell_{32}], \\ \frac{\partial F}{\partial \ell_{32}} &= 4[(d_{32} - \hat{d}_{32})\ell_{22} + (d_{33} - \hat{d}_{33})\ell_{32}], \\ \frac{\partial F}{\partial \ell_{31}} &= 4[(d_{31} - \hat{d}_{31})\ell_{11} + (d_{32} - \hat{d}_{32})\ell_{21} + (d_{33} - \hat{d}_{33})\ell_{31}], \\ \frac{\partial F}{\partial \ell_{33}} &= 4[(d_{33} - \hat{d}_{33})\ell_{33}]. \end{aligned} \quad (\text{A.2})$$

By combining each of the equations

$$\frac{\partial G}{\partial \ell_{ij}} = \frac{\partial R}{\partial \ell_{ij}} + \frac{\partial F}{\partial \ell_{ij}}, \quad \{ij\} \in \{11, 21, 22, 31, 32, 33\}, \quad (\text{A.3})$$

we arrive at the Euler-Lagrange equations corresponding to the minimization problem (13). In the numerical simula-

tions, we use the steepest descent method with a fixed time step. Thus, we have the six equations,

$$d_{ij}^{n+1} = d_{ij}^n - \Delta t \frac{\partial G^n}{\partial \ell_{ij}}, \quad \{kl\} \in \{11, 21, 22, 31, 32, 33\}, \quad (\text{A.4})$$

where n is the iteration index, and Δt is the time-step parameter. We approximate the gradient $\partial G/\partial \ell_{ij}$ by standard finite difference schemes, see, for example, [4]. We here note that each iteration of the form (A.4) is performed sequentially. Thus, the equations are solved as a coupled system of six PDEs.

REFERENCES

- [1] P. Perona and J. Malik, "Scale-space and edge detection using anisotropic diffusion," *IEEE Transactions on Pattern Analysis and Machine Intelligence*, vol. 12, no. 7, pp. 629–639, 1990.
- [2] L. I. Rudin, S. Osher, and E. Fatemi, "Nonlinear total variation based noise removal algorithms," *Physica D*, vol. 60, no. 1–4, pp. 259–268, 1992.
- [3] M. Lysaker, S. Osher, and X.-C. Tai, "Noise removal using smoothed normals and surface fitting," *IEEE Transactions on Image Processing*, vol. 13, no. 10, pp. 1345–1357, 2004.
- [4] T. F. Chan and S. Esedoglu, "Aspects of total variation regularized L^1 function approximation," *SIAM Journal on Applied Mathematics*, vol. 65, no. 5, pp. 1817–1837, 2005.
- [5] T. F. Chan and J. Shen, *Image Processing and Analysis: Variational, PDE, Wavelet, and Stochastic Methods*, SIAM, Philadelphia, Pa, USA, 2005.
- [6] J. Weickert, "A review of nonlinear diffusion filtering," in *Proceedings of the 1st International Conference on Scale-Space Theory in Computer Vision*, vol. 1252 of *Lecture Notes in Computer Science*, pp. 3–28, Utrecht, The Netherlands, July 1997.
- [7] J. Weickert and T. Brox, "Diffusion and regularization of vector- and matrix-valued images," Tech. Rep. preprint no. 58, Fachrichtung 6.1 Mathematik, Universitat des Saarlandes, Saarbrücken, Germany, 2002.
- [8] P. J. Basser, J. Mattiello, and D. LeBihan, "MR diffusion tensor spectroscopy and imaging," *Biophysical Journal*, vol. 66, no. 1, pp. 259–267, 1994.
- [9] D. Le Bihan, J.-F. Mangin, C. Poupon, et al., "Diffusion tensor imaging: concepts and applications," *Journal of Magnetic Resonance Imaging*, vol. 13, no. 4, pp. 534–546, 2001.
- [10] C.-F. Westin, S. E. Maier, H. Mamata, A. Nabavi, F. A. Jolesz, and R. Kikinis, "Processing and visualization for diffusion tensor MRI," *Medical Image Analysis*, vol. 6, no. 2, pp. 93–108, 2002.
- [11] S. Mori and P. B. Barker, "Diffusion magnetic resonance imaging: its principle and applications," *The Anatomical Record*, vol. 257, no. 3, pp. 102–109, 1999.
- [12] S. Mori and P. C. M. van Zijl, "Fiber tracking: principles and strategies—a technical review," *NMR in Biomedicine*, vol. 15, no. 7–8, pp. 468–480, 2002.
- [13] R. Bammer, "Basic principles of diffusion-weighted imaging," *European Journal of Radiology*, vol. 45, no. 3, pp. 169–184, 2003.
- [14] E. O. Stejskal and J. E. Tanner, "Spin diffusion measurements: spin echoes in the presence of a time-dependent field gradient," *The Journal of Chemical Physics*, vol. 42, no. 1, pp. 288–292, 1965.

- [15] E. O. Stejskal, "Use of spin echoes in a pulsed magnetic-field gradient to study anisotropic, restricted diffusion and flow," *The Journal of Chemical Physics*, vol. 43, no. 10, pp. 3597–3603, 1965.
- [16] P. Tofts, Ed., *Quantitative MRI of the Brain*, John Wiley & Sons, New York, NY, USA, 2005.
- [17] C.-F. Westin, S. E. Maier, H. Mamata, A. Nabavi, F. A. Jolesz, and R. Kikinis, "Processing and visualization for diffusion tensor MRI," *Medical Image Analysis*, vol. 6, no. 2, pp. 93–108, 2002.
- [18] Z. Wang, B. C. Vemuri, Y. Chen, and T. H. Mareci, "A constrained variational principle for direct estimation and smoothing of the diffusion tensor field from complex DWI," *IEEE Transactions on Medical Imaging*, vol. 23, no. 8, pp. 930–939, 2004.
- [19] D. Tschumperlé and R. Deriche, "Variational frameworks for DT-MRI estimation, regularization and visualization," in *Proceedings of the 9th IEEE International Conference on Computer Vision (ICCV '03)*, vol. 1, pp. 116–121, Nice, France, October 2003.
- [20] C.-F. Westin and H. Knutsson, "Tensor field regularization using normalized convolution," in *Proceedings of the 9th International Conference on Computer Aided Systems Theory (EUROCAST '03)*, R. Moreno-Diaz and F. Pichler, Eds., vol. 2809 of *Lecture Notes in Computer Science*, pp. 564–572, Las Palmas de Gran Canaria, Canary Islands, Spain, February 2003.
- [21] B. Chen and E. W. Hsu, "Noise removal in magnetic resonance diffusion tensor imaging," *Magnetic Resonance in Medicine*, vol. 54, no. 2, pp. 393–401, 2005.
- [22] C. Chef'd'hotel, D. Tschumperlé, R. Deriche, and O. Faugeras, "Regularizing flows for constrained matrix-valued images," *Journal of Mathematical Imaging and Vision*, vol. 20, no. 1-2, pp. 147–162, 2004.
- [23] Y. Gur and N. Sochen, "Denoising tensors via Lie group flows," in *Proceedings of the 3rd International Workshop on Variational, Geometric, and Level Set Methods in Computer Vision (VLSM '05)*, vol. 3752 of *Lecture Notes in Computer Science*, pp. 13–24, Springer, Beijing, China, October 2005.
- [24] D. Groisser, "Some differential-geometric remarks on a method for minimizing constrained functionals of matrix-valued functions," *Journal of Mathematical Imaging and Vision*, vol. 24, no. 3, pp. 349–358, 2006.
- [25] P. Blomgren and T. F. Chan, "Color TV: total variation methods for restoration of vector-valued images," *IEEE Transactions on Image Processing*, vol. 7, no. 3, pp. 304–309, 1998.
- [26] T. F. Chan, G. H. Golub, and P. Mulet, "A nonlinear primal-dual method for total variation-based image restoration," *SIAM Journal of Scientific Computing*, vol. 20, no. 6, pp. 1964–1977, 1999.
- [27] G. Sapiro, "Color snakes," Tech. Rep. HPL-95-113, Hewlett Packard Computer Peripherals Laboratory, Palo Alto, Calif, USA, 1995.
- [28] The Mathworks, "MatLab, The Language of Technical Computing," <http://www.mathworks.com/matlab/>.
- [29] S. Pajevic and C. Pierpaoli, "Color schemes to represent the orientation of anisotropic tissues from diffusion tensor data: application to white matter fiber tract mapping in the human brain," *Magnetic Resonance in Medicine*, vol. 42, no. 3, pp. 526–540, 1999.
- [30] Mori and coworkers, "DTI-studio", <http://cmmr.med.jhmi.edu/>.

Research Article

Thalamus Segmentation from Diffusion Tensor Magnetic Resonance Imaging

Ye Duan, Xiaoling Li, and Yongjian Xi

Department of Computer Science, College of Engineering, University of Missouri-Columbia, Columbia, MO 65211-2060, USA

Received 23 October 2006; Revised 31 May 2007; Accepted 8 September 2007

Recommended by Hongkai Zhao

We propose a semi-automatic thalamus and thalamus nuclei segmentation algorithm from diffusion tensor magnetic resonance imaging (DT-MRI) based on the mean-shift algorithm. Comparing with existing thalamus segmentation algorithms which are mainly based on K-means algorithm, our mean-shift-based algorithm is more flexible and adaptive. It does not assume a Gaussian distribution or a fixed number of clusters. Furthermore, the single parameter in the mean-shift-based algorithm supports hierarchical clustering naturally.

Copyright © 2007 Ye Duan et al. This is an open access article distributed under the Creative Commons Attribution License, which permits unrestricted use, distribution, and reproduction in any medium, provided the original work is properly cited.

1. INTRODUCTION

Thalamus is the relay center for nerve impulses in the brain. It mediates communication among sensory, motor, and associative brain regions. Axons from almost every sensory system connect here as the last site before the information reaches the cerebral cortex. Information received from the diverse brain regions is passed on to the cortex through the thalamus. Anatomically, thalamus is the largest, most internal structures of the diencephalon consisting of dual lobe masses of gray matter. It is located at the rostral end of the mid brain on each side of the third ventricle. Each lobe is about 4 centimeters. Motor nuclei of the thalamus receive signals from the striatum, cerebellum, project into the motor, and premotor areas of the cerebral cortex. The thalamus play a major role in the regulation of consciousness, alertness, arousal, and attention and is thus considered part of the limbic system.

Thalamus and thalamus nuclei segmentation have become more and more essential for a wide range of clinical and research applications. For example, thalamus changes in terms of volume and intensity are involved in a large number of diseases, such as schizophrenia, Parkinson's disease, and multiple sclerosis. Conventional imaging modalities such as computerized tomography (CT) or magnetic resonance imaging (MRI) however, do not provide the necessary image contrast to differentiate the individual thalamic nuclei. On the other hand, a new noninvasive imaging modality diffusion tensor magnetic resonance imaging (DT-

MRI) can relate the image intensities to the relative mobility of tissue water molecules [1]. In DT-MRI, a tensor describing local water diffusion is calculated for each voxel from measurements of diffusion in several directions. Since water diffusion along neural fiber tracts of the brain is highly anisotropic, DT-MRI had been used to study the brain connectivity by extracting the fiber tracts from the brain white matter. Most recently, researchers have started to use DT-MRI for segmentation purposes. Wiegell et al. [2] among of the first to segment thalamic nuclei directly from the DT-MRI data by using a k-means algorithm. Behrens et al. [3] proposed an algorithm to identify the thalamic nuclei by mapping the connections between the thalamus and the cortex. Jonasson et al. [4] presented a method for segmenting the thalamus and its subnuclei by propagating a set of coupled level sets through a region-based force defined from the similarity measure between the most representative tensor of each level sets and its neighboring voxels.

In this paper, we propose a semi-automatic thalamus and thalamus nuclei segmentation algorithm from diffusion tensor magnetic resonance imaging (DT-MRI) based on the mean-shift algorithm [5]. Comparing with existing thalamus segmentation algorithms which are based on K-means algorithm [2] or use K-means as an initialization [4], our mean-shift-based algorithm is more flexible and adaptive. It does not assume a Gaussian distribution or a fixed number of clusters. Furthermore, the single parameter in the mean-shift-based algorithm supports hierarchical clustering naturally. We will briefly review the background on diffusion

tensor magnetic resonance imaging and mean shift clustering in Section 2. The main algorithm for thalamus and thalamus nuclei segmentation will be described in Section 3. Experimental results are shown in Section 4. Finally, the conclusion and some future work directions are discussed in Section 5.

2. BACKGROUND

2.1. Diffusion tensor imaging

Diffusion tensor magnetic resonance imaging (DT-MRI) is a recent MR imaging modality. In diffusion tensor MRI, a tensor describing local water diffusion is acquired for each voxel. The geometric nature of the diffusion tensors can quantitatively characterize the local structure in tissues such as bone, muscles, and white matter of the brain. A good review on DT-MRI can be found in [1, 6].

In general, the symmetric 3 by 3 diffusion tensor matrix D has six degrees of freedom (number of independent coefficients in a matrix representation). To estimate the tensor, then, at least six measurements (taken from different non-collinear gradient directions) are needed, in addition to the baseline image data S_0 . Thus for each slice in the data set, seven images need to be collected with different diffusion weightings and gradient directions. Let S_0 represents the signal intensity in the absence of a diffusion-sensitizing field gradient and S_k the signal intensity in the presence of gradient $g_k = (g_{k_x}, g_{k_y}, g_{k_z})$, $k = 1, \dots, 6$. The equation for the loss in signal intensity due to diffusion is given by the Stejskal-Tanner formula:

$$\ln(S_k) = \ln(S_0) - \gamma^2 \delta^2 \left(\Delta - \frac{\delta}{3} \right) g_k^T D g_k, \quad (1)$$

where γ is the gyromagnetic ratio of hydrogen H (protons), δ is the duration of the diffusion sensitizing gradient pulses, and Δ is the time between the centers of the two pulses. The tensor D can then be computed by solving this system of six equations (1).

2.2. Mean shift clustering

Mean shift is a powerful general purpose technique for clustering scattered data [5]. Instead of assuming a fixed number of clusters as is common with other clustering methods (e.g. K-means), mean shift extracts the modes of the density function. We will review briefly the mean shift algorithm in the following. For a complete description of mean shift, please refer to the original paper [5].

Given an arbitrary set of n points $\chi = x_1, \dots, x_n$ in the d -dimensional Euclidean space R^d . The multivariate kernel density estimate obtained with kernel $K(x)$ and window radius h , computed in the point x , is defined as

$$\hat{f}(x) = \frac{1}{nh^d} \sum_{i=1}^n K\left(\frac{x-x_i}{h}\right), \quad (2)$$

where $K(x)$ is the spherically symmetric kernel function satisfying

$$K(x) \geq 0, \quad \int_{R^d} K(x) dx = 1, \quad (3)$$

and h is a smoothing parameter called the bandwidth.

We can further define a profile function $k(x)$ for the kernel function $K(x)$ of (2) such that

$$K(x) = c_{k,d} k(\|x\|^2), \quad (4)$$

where $c_{k,d}$ is the normalized constant. The density estimator of (2) can then be rewritten as

$$\hat{f}(x) = \frac{c_{k,d}}{nh^d} \sum_{i=1}^n k\left(\left\|\frac{x-x_i}{h}\right\|^2\right). \quad (5)$$

Assume now that we are interested in subdividing scattered data χ into a set of clusters. It is natural to consider the points where \hat{f} defined by (5) have local maxima as centers of the clusters. The simplest method to find the local maxima of the \hat{f} is to compute the gradient of \hat{f} and use a hill-climbing process to map each input point to its local maxima (i.e., mode) defined by \hat{f} . These resulting modes can then be used to select cluster shapes using basins of attraction, and can have very nontrivial shapes unlike k-means clustering where points are simply assigned to the nearest cluster center. The single bandwidth parameter h allows the number of clusters to be chosen in terms of a length scale in the input point space.

From (5) we can compute the gradient of \hat{f} :

$$\nabla \hat{f}(x) = \frac{2c_{k,d}}{nh^{d+2}} \sum_{i=1}^n g\left(\left\|\frac{x-x_i}{h}\right\|^2\right) m(x), \quad (6)$$

where $g(x) = -k'(x)$. $m(x)$ is the mean shift vector and is given by

$$m(x) = \frac{\sum_{i=1}^n x_i g(\|(x-x_i)/h\|^2)}{\sum_{i=1}^n g(\|(x-x_i)/h\|^2)} - x, \quad (7)$$

for example, the difference between the weighted mean, using the kernel g for weights, and x , the center of the kernel (window). The general mean shift clustering procedure consists of the following two steps:

- (1) initialize: $y_0 = x$;
- (2) update by hill climbing: $y_{j+1} = y_j + m(y_j)$ until convergence.

3. THALAMUS AND THALAMUS NUCLEI SEGMENTATION BY MEAN SHIFT

In this section, we will describe our framework for thalamus and thalamus nuclei segmentation from DT-MRI data based on the previously described mean-shift algorithm. There are

two different domains of similarity: spatial and tensor in the DT-MRI image data, for example, each point x_i in the data set χ of the joint spatial-tensor domain has two components of different nature, $x_i = (x_i^s, x_i^r)$, where x_i^s is the spatial component, and x_i^r is the tensor component. The mean shift algorithm can be employed by extending the density estimator of (5) with the following separable kernels:

$$\hat{f}(x) = C \sum_{i=1}^n k_s \left(\left\| \frac{x^s - x_i^s}{h_s} \right\|^2 \right) k_r \left(\left\| \frac{x^r - x_i^r}{h_r} \right\|^2 \right), \quad (8)$$

here k_s is the kernel profile in the spatial domain with bandwidth parameter h_s , k_r is the kernel profile in the tensor domain with bandwidth parameter h_r , and C is the corresponding normalization constant. As suggested by [5], an Epanechnikov kernel with profile $k_E(x)$,

$$k_E(x) = \begin{cases} 1 - x & \text{if } 0 \leq x \leq 1, \\ 0 & \text{otherwise,} \end{cases} \quad (9)$$

or a (truncated) normal kernel with profile $k_N(x) = \exp(-1/2x), x > 0$, always provides satisfactory performance, so the user only has to set the bandwidth parameter $h = (h_s, h_r)$, which, by controlling the size of the kernel, determines the resolution of the mode selection. For DT-MRI data, we have tried both kernels and found no significant difference. In our experiment we choose the Epanechnikov kernel because of its simplicity. The distance metric in the spatial domain is the Euclidian distance metric, the distance metric in the tensor domain is the following Frobenius norm:

$$\|x_1^r - x_2^r\| = \sqrt{\text{Trace}((D_{x_1} - D_{x_2})(D_{x_1} - D_{x_2})^T)}, \quad (10)$$

D_{x_1}, D_{x_2} are the tensor matrices at points x_1, x_2 , respectively.

4. EXPERIMENTAL RESULTS ON REAL AND SYNTHETIC DATA

4.1. Synthetic data

To validate our method, we have applied our method on some synthetic data. For comparison purpose, we use the same synthetic data used in [4]. A slice of the synthetic tensor field is shown in Figure 6. In Figure 7, the regions have been segmented on the synthetic field without any noise added. In Figure 8, noise is added into the same synthetic field at signal-to-noise-ratio (SNR) level 32. In both of these two examples, our algorithm obtained much better results than both the K-means algorithm and the method of [4].

4.2. Real data

In this section, we will show some of the experimental results of thalamus and thalamus nuclei segmentation from DT-MRI data. Figure 1 illustrates the thalamus segmentation process. The initial thalamus segmentation is conducted

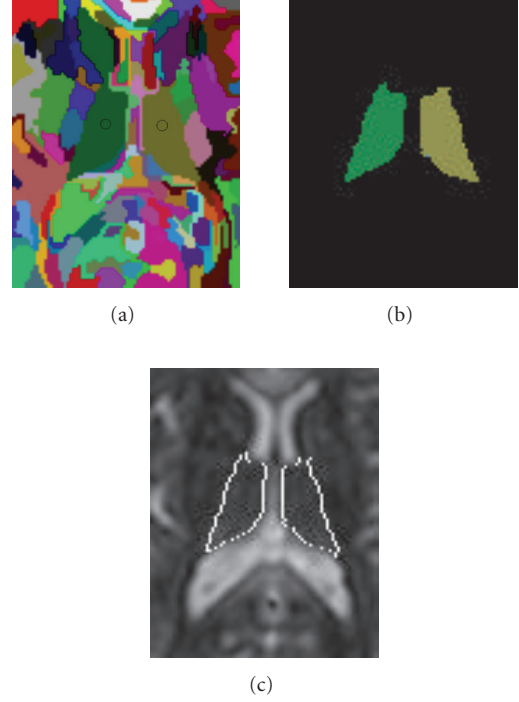


FIGURE 1: Thalamus segmentation. (a) The initial thalamus segmentation is conducted interactively, that is, the user need to identify the pair of symmetric clusters (left thalamus and right thalamus, marked by circles in the figure for illustration) from other clusters. Since the thalamus is bounded by relatively homogenous structures such as the fiber tract and Cerebrospinal fluid (CSF), this step can be done quite easily. (b) Extracted pair of thalamus. (c) Extracted pair of thalamus superimposed on the original DT-MRI image.

interactively, for example, after applying the mean shift algorithm with a bigger bandwidth parameter, the user needs to identify the pair of symmetric clusters (left thalamus and right thalamus, marked by circles in Figure 1(a) for illustration) from other clusters. Since the thalamus is bounded by relatively homogenous structures such as the fiber tract and Cerebrospinal fluid (CSF), this step can be done quite easily (Figure 1(b)). In this example, the bandwidth parameter is set as $h = (h_s, h_r) = (7, 13)$.

The initially segmented thalamus will then serve as the mask for the subsequent thalamus nuclei segmentation, which will be conducted automatically with a smaller bandwidth parameter. The parameter chosen will determine the scale of features detected, so different values may be desired based on the data set quality, features of interest, and so forth. Figure 2 shows the thalamus nuclei segmentation results of the left thalamus. To illustrate the hierarchical nature of the mean-shift-based algorithm, we fixed the spatial bandwidth h_s as 7, and gradually reduced the tensor bandwidth h_r from 13 (Figure 2(a)) to 11 (Figure 2(b)), 10.5 (Figure 2(c)), 10 (Figure 2(d)), and 8 (Figure 2(e)). By gradually reducing the bandwidth, more and more detailed nuclei structures can be seen.

We conducted similar hierarchical segmentation for the right thalamus as well and is shown in Figure 3. We again

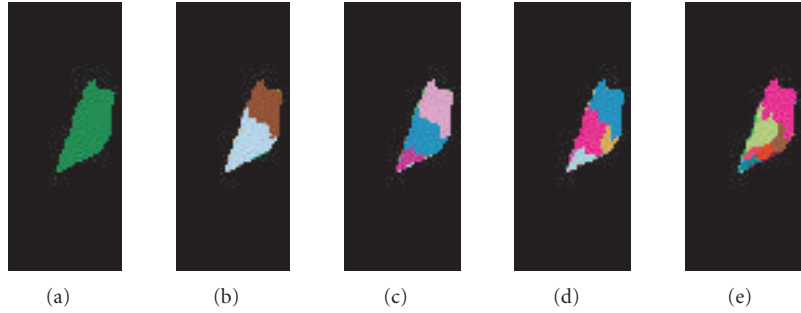


FIGURE 2: Mean shift based hierarchical thalamus nuclei segmentation results of the left thalamus. (a) The segmented left thalamus by setting the bandwidth parameter as $h = (h_s, h_r) = (7, 13)$. (b) The segmented anterior and posterior parts of the left thalamus by setting the bandwidth parameter as $h = (h_s, h_r) = (7, 11)$. (c) The segmentation result by setting the bandwidth parameter as $h = (h_s, h_r) = (7, 10.5)$. (d) The segmentation result by setting the bandwidth parameter as $h = (h_s, h_r) = (7, 10)$. (e) The segmented thalamus nuclei by setting the bandwidth parameter $h = (h_s, h_r) = (7, 8)$.

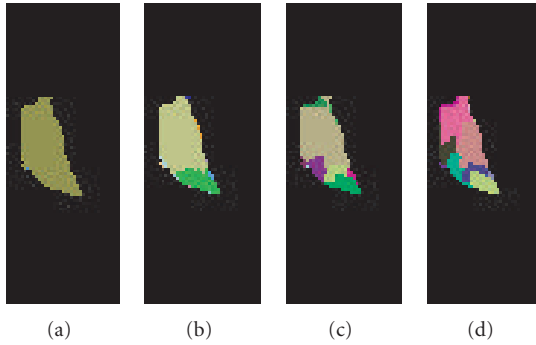


FIGURE 3: Hierarchical thalamus nuclei segmentation results of the right thalamus. (a) The right thalamus, $h = (h_s, h_r) = (7, 13)$. (b) The segmented anterior and posterior parts of the right thalamus, $h = (h_s, h_r) = (7, 11)$. (c) The segmentation result by setting the bandwidth parameter as $h = (h_s, h_r) = (7, 7)$. (d) The segmented thalamus nuclei by setting the bandwidth parameter $h = (h_s, h_r) = (1, 1.5)$.

fixed the spatial bandwidth h_s as 7, and gradually reduced the tensor bandwidth h_r from 13 (Figure 3(a)) to 11 (Figure 3(b)), and 7 (Figure 3(c)). However, quite different settings of the bandwidth parameter need to be chosen $h = (h_s, h_r) = (1, 1.5)$ to obtain the desired final thalamus nuclei segmentation (Figure 3(d)). We do not know the exact reason of this (the different parameter setting for the left and right thalamus), one of the possible reasons might be the artifact during the image acquisition process (e.g., the image slice is not totally orthogonal across the thalamus), or the nuclei structures between the left and the right thalamus are not symmetrical indeed. More experiments and research are certainly needed in the future to answer these questions. Nonetheless, if we compare Figure 2(e) and Figure 3(d) with Figure 4, which is the histological atlas of the human thalamus with nuclei outlined by black lines [3], we can see they are very close. Finally, a 3D rendering of the thalamus nuclei segmentation result is shown in Figure 5.



FIGURE 4: The histological atlas of the human thalamus with nuclei outlined by black lines (Image courtesy of Behrens et al. [3]).

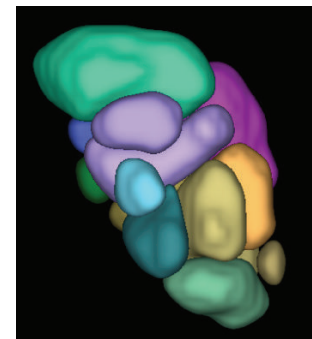


FIGURE 5: A 3D view of the thalamus nuclei segmentation results.

5. DISCUSSION

The main contribution of the paper is the application of the powerful mean shift clustering algorithm for thalamus segmentation from the DT-MRI data. Comparing with existing thalamus segmentation algorithms ([2, 4]) which are based on K-means algorithm, our mean-shift-based algorithm has several potential advantages. (1) Since the mean

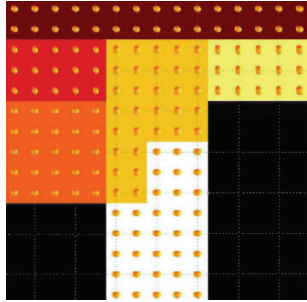


FIGURE 6: A slice of the synthetic tensor field used to test the segmentation method. (Image courtesy of Jonasson et al. [4].)

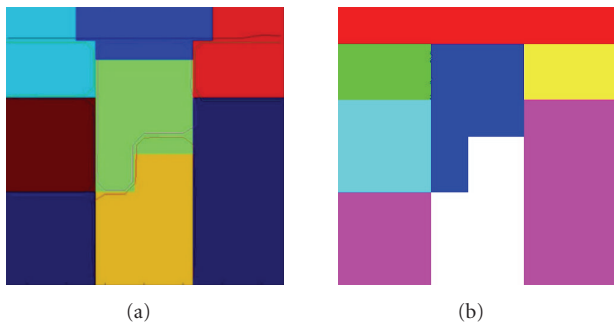


FIGURE 7: Segmentation results on a synthetic field, without any noise added. (a) Results of [4] displayed on the results obtained with the K-means algorithm. (b) Results from our algorithm.

shift algorithm is based on nonparametric density estimation, it does not assume the data is always Gaussian, hence it is more generic and flexible. (2) Unlike K-means algorithm, the mean-shift algorithm does not assume a fixed number of clusters, hence it is more adaptive to the diversity of the dataset. (3) There is only one parameter in the mean-shift-based algorithm, the bandwidth parameter, which controls the scale of the features detected. (4) And by setting the bandwidth parameter from large to small, mean shift naturally supports hierarchical clustering, as shown in this paper on thalamus and thalamus nuclei segmentation.

There are two main directions to further improve the thalamus segmentation results: (1) currently, the thalamus segmentation is conducted semi-automatically, that is, the user has to pick the pair of distinct clusters (left and right parts of the thalamus) from other neighboring clusters such as the fiber tracts and CSE. Although this is quite easy to do, it would be even better if the thalamus can be automatically segmented; moreover, a postprocessing active-contour-based diffusion step (as is done in [4]) might be able to further smooth the nuclei boundary obtained from the clustering algorithm. (2) We would like to work closely with domain specialists such as neurobiologists to verify and validate the segmentation results, and to identify the thalamus nuclei structures. The collaboration with domain specialists will also help us to choose the best bandwidth parameter for

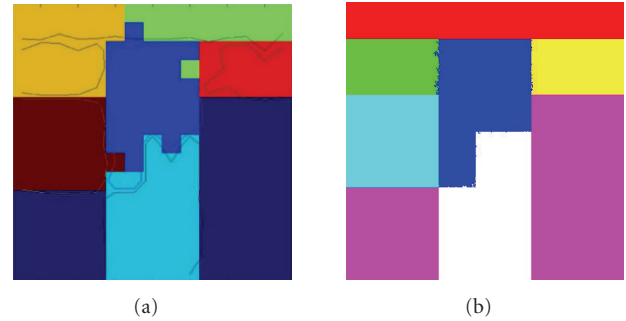


FIGURE 8: Segmentation results on a synthetic field, with SNR = 32. (a) Results of [4] displayed on the results obtained with the K-means algorithm. (b) Results from our algorithm.

the mean shift algorithm to create clinically most meaningful segmentation results.

ACKNOWLEDGMENTS

The authors are very grateful to Dr. Susumu Mori and his Laboratory of Brain Anatomical MRI at Johns Hopkins University for providing the 2.5 mm resolution DT-MRI data used in this paper.

REFERENCES

- [1] P. J. Basser, S. Pajevic, C. Pierpaoli, J. Duda, and A. Aldroubi, "In vivo fiber tractography using DT-MRI data," *Magnetic Resonance in Medicine*, vol. 44, no. 4, pp. 625–632, 2000.
- [2] M. R. Wiegell, D. S. Tuch, H. B. W. Larsson, and V. J. Wedeen, "Automatic segmentation of thalamic nuclei from diffusion tensor magnetic resonance imaging," *NeuroImage*, vol. 19, no. 2, pp. 391–401, 2003.
- [3] T. E. Behrens, H. Johansen-Berg, M. W. Woolrich, et al., "Non-invasive mapping of connections between human thalamus and cortex using diffusion imaging," *Nature Neuroscience*, vol. 6, no. 7, pp. 750–757, 2003.
- [4] L. Jonasson, P. Hagmann, C. Pollo, et al., "A level set method for segmentation of the thalamus and its nuclei in DT-MRI," *Signal Processing*, vol. 87, no. 2, pp. 309–321, 2007.
- [5] D. Comaniciu and P. Meer, "Mean shift: a robust approach toward feature space analysis," *IEEE Transactions on Pattern Analysis and Machine Intelligence*, vol. 24, no. 5, pp. 603–619, 2002.
- [6] C.-F. Westin, S. E. Maier, H. Mamata, A. Nabavi, F. A. Jolesz, and R. Kikinis, "Processing and visualization for diffusion tensor MRI," *Medical Image Analysis*, vol. 6, no. 2, pp. 93–108, 2002.

Research Article

The Factorization Method for Electrical Impedance Tomography Data from a New Planar Device

Mustapha Azzouz,¹ Martin Hanke,² Chantal Oesterlein,² and Karl Schilcher¹

¹Institut für Physik, Johannes Gutenberg-Universität Mainz, 55099 Mainz, Germany

²Institut für Mathematik, Johannes Gutenberg-Universität Mainz, 55099 Mainz, Germany

Received 19 September 2006; Revised 28 January 2007; Accepted 11 April 2007

Recommended by Alfred Karl Louis

We present numerical results for two reconstruction methods for a new planar electrical impedance tomography device. This prototype allows noninvasive medical imaging techniques if only one side of a patient is accessible for electric measurements. The two reconstruction methods have different properties: one is a linearization-type method that allows quantitative reconstructions; the other one, that is, the factorization method, is a qualitative one, and is designed to detect anomalies within the body.

Copyright © 2007 Mustapha Azzouz et al. This is an open access article distributed under the Creative Commons Attribution License, which permits unrestricted use, distribution, and reproduction in any medium, provided the original work is properly cited.

1. INTRODUCTION

In electrical impedance tomography (EIT), electric currents are applied to the boundary of an object and the induced surface voltages are measured. These data are used to reconstruct the conductivity distribution in the interior of the object. Important practical applications arise in medical imaging.

Unfortunately, this *inverse conductivity problem* is nonlinear and severely ill-posed. That means that even large conductivity variations in the interior of the object may only lead to tiny changes in the surface data. EIT therefore represents a challenging problem. Most reconstruction procedures that have been proposed include either some iterative or some linearization methods where the ill-posedness is regulated in one way or another (cf., e.g., Holder [1]). It is fair to say that the success in medical applications is rather disappointing, except possibly for two-dimensional situations.

A way out of this dilemma is to reduce the amount of information that is to be extracted from the data by incorporating a priori information. In many applications, for example, in mammography, one may only be interested in finding regions in the interior where the conductivity changes rapidly in comparison to an approximately constant background conductivity. In this way, the ill-posedness is circumvented to a certain extent.

The so-called *factorization method* is a reconstruction scheme that is adapted to this kind of applications. In this

note, we present some first numerical results for this particular method using real EIT data. These data were obtained with a new EIT device developed at our institution which allows to take data in two- and three-dimensional configurations.

In contrast to most previous EIT instruments, but similar to prototypes studied, for example, by Mueller et al. [2], and by Cherepenin et al. [3], our device uses a planar sensing head, and is designed for medical applications where measurements can only be taken from one side of the patient. This is an important issue in the context of mammography, or in monitoring patients in intensive care units, to name only two such applications. We refer to Zou and Guo [4] for a review of further electrical impedance imaging devices for breast cancer detection, including the commercial TS 2000 system.

2. DESCRIPTION OF THE DEVICE

The Mainz tomograph consists of three parts, a sensing head, an electronic device to apply and measure electric potential and current patterns, and a computer for the image reconstruction (cf. Figure 1).

The sensing head has a diameter of 10 cm and consists of 16 large electrodes, arranged on the outer ring of a disk. Through these electrodes the current is injected and both current and voltages can be measured. There is another set of 64 small high-impedance electrodes placed in the interior

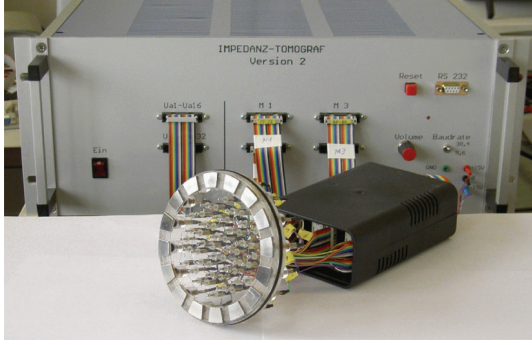


FIGURE 1: The tomograph.

which can be used to measure additional voltages, however, these measurements have not yet been used to solve the inverse problem.

The data acquisition device consists of five modules. The first module is a microcontroller to facilitate the communication between the measuring device and the external components via an RS232 serial interface. The second module generates preset sinusoidal voltages of frequency 5–50 kHz which can be used to drive 16 (or 32) current injecting electrodes. The amplitudes can be set positive or negative by 32 DAC to 16-bit accuracy and can be modulated program-controlled to any desired amplitude pattern. The resulting current at each injection electrode passes through a precision resistor and a special operational amplifier to facilitate the simultaneous measurement of the current. The voltages on the interior electrode are measured with 16-bit accuracy with the help of the third module. The fourth module serves to read the data and to measure the signal by a peak detector largely in parallel via 8 multiplexers of 16 channels each. The measured value of the peak detector is subsequently digitalized to 16-bit accuracy. In the fifth module, finally, the sign of the modulation is defined.

There are $N - 1$ independent measurements for N current injecting electrodes. In most reconstruction algorithms, it is assumed that currents are prescribed and voltages are measured. Because of the much simpler electronic implementation, voltages are applied and currents are measured on the injectors (voltages are also measured in the interior) in our device. It is, however, no problem to convert to current-driven data by linear combination of the various voltage-driven data. For optimal resolution, it is of advantage to apply trigonometric voltage or current patterns of different frequencies (cf., e.g., Newell et al. [5]).

So far we have no clinical data at our disposal. Instead, we have placed the sensing head into the bottom of an appropriate container of large lateral dimensions and filled with a conducting liquid. The level of the liquid in the tank has been kept very low so as to approximate a two-dimensional situation. Various objects have been immersed into the liquid. Measurements have been taken with and without the immersed bodies. The latter serves as reference measurements where necessary. Below we will present numerical tests with real data that have been obtained this way.

3. A LINEARIZATION-TYPE RECONSTRUCTION METHOD

For an isotropic conductivity distribution $\sigma = \sigma(x)$ the electric potential $u = u(x)$ satisfies the equation

$$\nabla \cdot (\sigma \nabla u) = 0, \quad (1)$$

where σ and u are defined in a certain volume Ω . This is a direct consequence of the conservation of the electric current $\mathbf{j} = \sigma \nabla u$. A driving force for nontrivial potentials u is, for example, a current that is injected into Ω through some electrodes attached to a subset $\Gamma \subset \partial\Omega$. The above differential equation is fundamental to the study of EIT. For constant conductivities σ it becomes the homogeneous Laplace equation, whose solutions u are the harmonic functions.

In our application where the device is much smaller than the human body to which it is applied, it appears appropriate to model the volume Ω as a three-dimensional half space, and the subset Γ as a circle, say the unit circle. In fact, as our currents do not penetrate deep into the body, it is even appropriate to further simplify the model, and to identify Ω with its boundary $\partial\Omega$. This results in a two-dimensional model described by the following diffraction problem:

$$\nabla \cdot (\sigma \nabla u) = 0 \quad \text{in } \mathbb{R}^2 \setminus \Gamma, \quad (2)$$

where u is constraint to satisfy

$$[\nu \cdot \mathbf{j}]_{\Gamma} = f, \quad [u]_{\Gamma} = 0, \quad (3)$$

$$|u(x)| = O(1) \quad \text{as } |x| \rightarrow \infty,$$

$$\int_{\Gamma} u \, ds = 0. \quad (4)$$

The square brackets in (3) refer to the jump of the respective quantity within the brackets when moving from the inside to the outside of Γ ; ν is the outer normal of Γ . The first condition in (3) therefore asserts that current f is injected into the body along Γ , whereas the second condition requires that u is continuous across Γ , that is, that the potential on Γ is well-defined. The last condition in (3) eliminates nonphysical solutions, whereas the physical one is unique after fixing the ground potential; this is accomplished via the normalization condition (4).

In the EIT problem known currents are injected and the resulting potentials are measured on Γ . From these data the conductivity σ is to be determined. The currents and potentials on the electrodes are related through the measurement operator

$$M : \begin{cases} \mathcal{L}_{\diamond}^2(\Gamma) \rightarrow \mathcal{L}_{\diamond}^2(\Gamma), \\ f \mapsto u|_{\Gamma}, \end{cases} \quad (5)$$

associated with the differential equation (2), (3), and (4). Here,

$$\mathcal{L}_{\diamond}^2(\Gamma) = \left\{ g \in \mathcal{L}^2(\Gamma) : \int_{\Gamma} g \, ds = 0 \right\} \quad (6)$$

denotes the set of all square integrable functions over Γ with zero mean. Note that we have fixed $u|_{\Gamma}$ to belong to $\mathcal{L}^2_{\diamond}(\Gamma)$ according to (4).

For a simple example let $\sigma = 1$ be constant in \mathbb{R}^2 , in which case we will further on write M_0 for M of (5). Later on, $\sigma = 1$ will be considered as our reference, or background conductivity. The associated potential $u = u_0$ is a solution of the homogeneous Laplace equation inside (and outside) the unit disk, and, using polar coordinates, can be written in the form

$$u_0(r, \theta) = \sum_{k=-\infty}^{\infty} c_k r^{|k|} e^{ik\theta}, \quad 0 \leq r \leq 1, \quad (7)$$

with complex coefficients c_k , $k \in \mathbb{Z}$. On Γ we have

$$u_0(1, \theta) = \sum_{k=-\infty}^{\infty} c_k e^{ik\theta}, \quad (8)$$

and, because of the continuity of the potential across Γ , we obtain

$$u_0(r, \theta) = \sum_{k=-\infty}^{\infty} c_k r^{-|k|} e^{ik\theta}, \quad 1 < r < \infty. \quad (9)$$

In fact, the normalization (4) requires that $c_0 = 0$, and hence, it follows from (3) that

$$f(\theta) = [\nu \cdot \mathbf{j}]_{\Gamma} = \left[\frac{\partial u_0(r, \theta)}{\partial r} \right]_{r=1} = -2 \sum_{k \neq 0} |k| c_k e^{ik\theta}. \quad (10)$$

The eigenfunctions of M_0 are therefore

$$f^{(k)}(\theta) = e^{ik\theta}, \quad k \in \mathbb{Z} \setminus \{0\}, \quad (11)$$

which are mapped onto the potentials

$$u_0^{(k)}(r, \theta) = -\frac{1}{2|k|} \begin{cases} r^{|k|} e^{ik\theta}, & 0 \leq r \leq 1, \\ r^{-|k|} e^{ik\theta}, & 1 < r < \infty. \end{cases} \quad (12)$$

The corresponding eigenvalues of M_0 are given by $-1/(2|k|)$, respectively.

We now turn to the solution of our inverse problem associated with the diffraction problem (2), (3), and (4), namely, the identification of σ given the measurement operator M of (5). We will compare two different algorithms to solve this problem. First, we use a somewhat standard reconstruction method which is based on a certain kind of linearization, and which is close to the method implemented in [2]; second, we apply the factorization method described in the subsequent section. For both methods we will assume that the conductivity fulfills $\sigma = 1$ near Γ and near infinity.

If σ is smooth, (2) can also be written in the form

$$\Delta u = -\nabla(\log \sigma) \cdot \nabla u, \quad x \in \mathbb{R}^2 \setminus \Gamma, \quad (13)$$

and, because of the assumption that $\sigma = 1$ on Γ , we can formally solve problem (13), (3), by using the fundamental solution

$$\Phi(x, x') = \frac{1}{2\pi} \log \frac{1}{|x - x'|} \quad (14)$$

of Laplace's equation (cf., e.g., Kress [6]). This yields

$$u(x) = \int_{\mathbb{R}^2 \setminus \Gamma} \Phi(x, x') \nabla(\log \sigma(x')) \cdot \nabla u(x') dx' - \int_{\Gamma} \Phi(x, x') f(x') ds' + c, \quad (15)$$

where the constant c must be chosen so as to satisfy (4). Note that the second term on the right-hand side of (15) is the corresponding potential u_0 associated with the homogeneous reference conductivity. We can therefore rewrite (15) as

$$u(x) = u_0(x) + \int_{\mathbb{R}^2 \setminus \Gamma} \Phi(x, x') \nabla(\log \sigma(x')) \cdot \nabla u(x') dx' + c. \quad (16)$$

Assuming further that $u \approx u_0$ we can approximate

$$u(x) - u_0(x) \approx \int_{\mathbb{R}^2 \setminus \Gamma} \Phi(x, x') \nabla(\log \sigma(x')) \cdot \nabla u_0(x') dx' + c, \quad (17)$$

and, since u_0 is a harmonic function and because of our assumption that $\sigma = 1$ near Γ and near infinity, a partial integration of the integral on the right-hand side yields

$$\delta u(x) \approx - \int_{\mathbb{R}^2 \setminus \Gamma} \nabla_{x'} \Phi(x, x') \cdot \nabla u_0(x') \log \sigma(x') dx' + c, \quad (18)$$

where we have set

$$\delta u(x) = u(x) - u_0(x). \quad (19)$$

Integrating (18) versus the aforementioned eigenfunctions $f^{(k)}$ of the reference operator M_0 , we get rid of the constant and obtain the system of equations

$$\int_{\mathbb{R}^2 \setminus \Gamma} K_k(x') \log \sigma(x') dx' = \int_{\Gamma} f^{(k)}(x) \delta u(x) ds, \quad k \in \mathbb{Z} \setminus \{0\}, \quad (20)$$

where

$$K_k(x) = -\nabla u_0^{(k)}(x) \cdot \nabla u_0(x), \quad (21)$$

and $u_0^{(k)}$ is the reference potential corresponding to the input current $f^{(k)}$ (cf. (12)).

We mention that the same linear system is obtained in the first step of Newton's method if the initial conductivity guess is the constant $\sigma_0 = 1$, and is to be replaced by $\sigma_1 = 1 + \log \sigma$ which is a good approximation of σ if the latter is close to one (cf., e.g., [2] or [7]).

Every boundary current we apply leads to such a system of (20). If we further assume that the conductivity is homogeneous outside of Γ , that is, coincides with the background conductivity, then the left-hand side of (20) simplifies to an integral over the unit disk only. The combined set of all these equations can be inverted to obtain the conductivity σ . Note, however, that (20) is an approximate identity only, based on

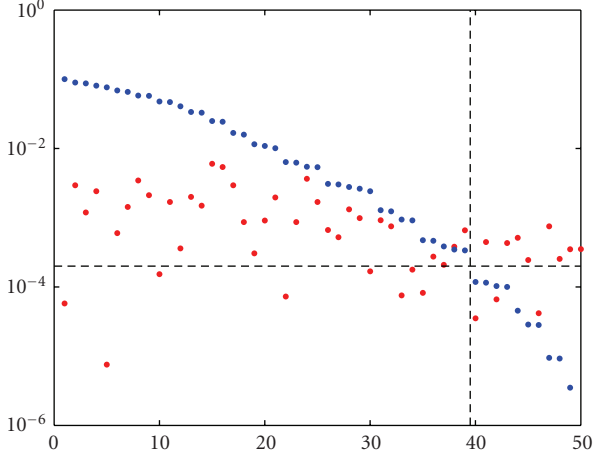


FIGURE 2: Singular values (blue) and singular components (red) of the right-hand side.

the assumption that $u \approx u_0$. Also, since the problem is ill-posed, we need to regularize this linear system. We implemented the truncated singular value decomposition for this purpose. Figure 2 shows the singular values of the matrix and the corresponding singular components of the right-hand side of (20) for a particular set of data. As indicated by the dashed lines, we used the gap in the singular values near the crossover point with the singular components for truncation.

Figure 2 corresponds to a setup with a metal object of roughly 12×13 mm that has been immersed into the container as the phantom to be reconstructed. The phantom and the resulting reconstructions are shown in Figure 3. The left-hand reconstruction has been computed from measured reference potentials u_0 corresponding to a tank with no object immersed. The reconstruction on the right has been computed to simulate a situation where only “absolute” data, that is, the potentials u , are available. Here we have approximated δu by eliminating the frequency of the injected current from the Fourier spectrum of u . Both reconstructions are fairly good, although the one with absolute data is only qualitatively correct.

Note that potentials and currents are only measured on the 16 planar electrodes that are clearly visible in the photo of the phantom.

4. THE FACTORIZATION METHOD

Next, we describe the variant of the so-called factorization method which we have implemented for comparison. As a general reference we refer to [8] for more information about this method. In contrast to the previous approach which yields the absolute figures of the conductivity (up to a certain accuracy), this method is not a quantitative one. Instead its purpose is to detect abrupt deviations of the conductivity as compared to a certain reference, namely, the constant background conductivity in our setting. While this approach appears to be quite appropriate for medical applications, it

requires difference data and has not yet been generalized to the use of absolute data.

To be precise, we now assume that the true conductivity

$$\sigma(x) = \begin{cases} \kappa, & x \in D \subset \mathbb{R}^2, \\ 1, & x \in \mathbb{R}^2 \setminus D, \end{cases} \quad (22)$$

is different from the background in some subset $D \subset \mathbb{R}^2$ only. Here, $\kappa \neq 1$ is a constant, and D is assumed to be strictly on one side of Γ , that is, either within the unit disk or completely outside the unit disk. However, D need not be connected, but can be the union of finitely many simply connected domains (anomalies, tumors, etc.).

The basic ingredient for the design and analysis of the factorization method is the representation of the relative data

$$M - M_0 = LFL' \quad (23)$$

as a product of three bounded operators, out of which the first and the last are dual to each other. Recall that M_0 is the measurement operator from (5) associated with the reference conductivity equal to one. The operator L , which is the most important for us, is defined via the exterior Neumann problem

$$\Delta w = 0 \quad \text{in } \mathbb{R}^2 \setminus \bar{D}, \quad \frac{\partial w}{\partial \nu} = \varphi \quad \text{on } \partial D, \quad (24)$$

with the same constraints

$$\int_{\Gamma} w ds = 0, \quad |w(x)| = O(1) \quad \text{as } |x| \rightarrow \infty \quad (25)$$

on w as in (4); given the solution w of (24), (25), the operator L now maps

$$L : \varphi \mapsto w|_{\Gamma}. \quad (26)$$

Because of our assumption that D lies strictly on one side of Γ , it can be shown that L is injective and its range is dense in $\mathcal{L}_{\diamond}^2(\Gamma)$. A more careful analysis which is outside the scope of this paper exhibits the fundamental range identity

$$\mathcal{R}(|M - M_0|^{1/2}) = \mathcal{R}(L), \quad (27)$$

which is crucial for the success of the factorization method. We refer to [9], or Gebauer [10], for details.

To utilize this result we remark that, on the one hand, the left-hand side member of (27) is available to us because of the given measurements. On the other hand, it is quite easy to characterize the elements of $\mathcal{R}(L)$, the right-hand side member of (27). In fact, consider the potential

$$w_{z,d}(x) = \frac{1}{2\pi} \frac{d \cdot (x - z)}{|x - z|^2}, \quad x \in \mathbb{R}^2 \setminus \{z\}, \quad (28)$$

of a dipole in $z \in \mathbb{R}^2 \setminus \Gamma$ with dipole moment $d \in \mathbb{R}^2$, $|d| = 1$, and its trace

$$g_{z,d} = w_{z,d}|_{\Gamma} \in \mathcal{L}_{\diamond}^2(\Gamma) \quad (29)$$

on Γ . Now it is easy to see that $g_{z,d}$ belongs to the range of L , if its singularity z lies within D . Unfortunately, the reverse statement is not quite right. Rather, we have the following theorem.

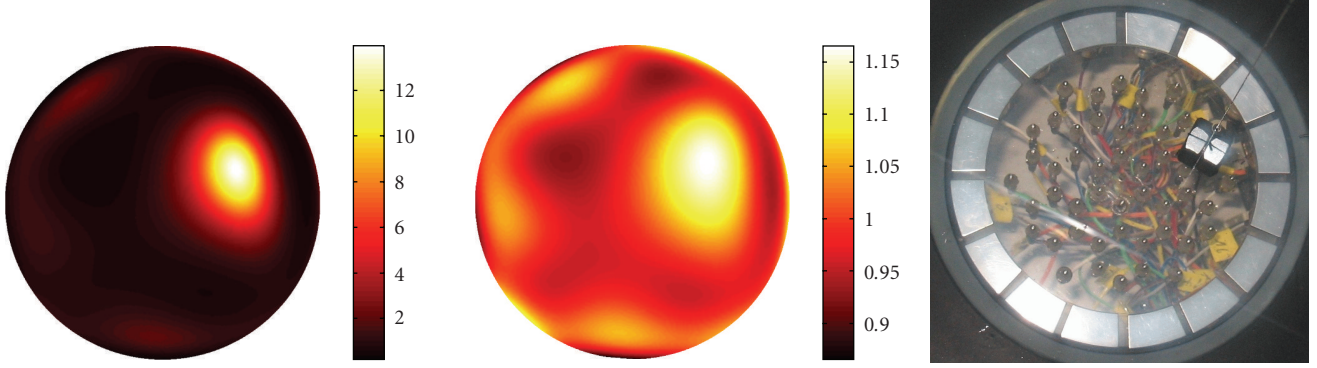


FIGURE 3: Top: Reconstructions with difference (left) and absolute data (right). Bottom: Phantom used for these two reconstructions.

Theorem 1. Assume that D lies strictly on one side of the unit circle Γ , and let D^* be the reflection of D with respect to Γ , that is,

$$D^* = \{x^* = x/|x|^2 : x \in D \setminus \{0\}\}. \quad (30)$$

Then, for $z \in \mathbb{R}^2$, $d \in \mathbb{R}^2$ with $|d| = 1$, and $g_{z,d}$ defined as in (29),

$$g_{z,d} \in \mathcal{R}(L) \quad \text{iff } z \in D \cup D^*. \quad (31)$$

Proof. The key observation for the proof is that for each dipole potential $w_{z,d}$ of (28) with $z \notin (\Gamma \cup \{0\})$ there exists a corresponding potential $w_{z^*,d'}$ of a dipole at z^* with dipole moment d' such that the traces of $w_{z,d}$ and $w_{z^*,d'}$ on Γ are the same. Here, $z^* = z/|z|^2$ is the reflection of z with respect to Γ , and d' is given by

$$d' = \frac{1}{|z|^4} (|z|^2 d - 2(d \cdot z)z). \quad (32)$$

Since we have observed above that $z \in D$ implies that $g_{z,d} \in \mathcal{R}(L)$, we are now in the position to add that $g_{z,d} \in \mathcal{R}(L)$, also if $z \in D^*$. This establishes one direction of the proof. To prove the other direction, assume without loss of generality that D is the subset of $D \cup D^*$ that lies within Γ . Next, consider some $z \in \mathbb{R}^2$ and some dipole moment d for which $g_{z,d}$ belongs to the range of L . Because $w_{z,d}$ has a pole at $x = z$, z cannot belong to Γ in this case. We thus assume for the moment that z lies within the unit disk. The fact that $g_{z,d}$ belongs to $\mathcal{R}(L)$ means that there are appropriate Neumann data φ such that the unique solution w of the exterior Neumann problem (24), (25), and the dipole potential $w_{z,d}$ of (28) have the same trace on Γ . As a consequence, w and $w_{z,d}$ both solve the exterior Dirichlet problem

$$\begin{aligned} \Delta v &= 0 \quad \text{in } |x| > 1, & v|_{\Gamma} &= g_{z,d}, \\ |v(x)| &= O(1) \quad \text{for } |x| \rightarrow \infty, \end{aligned} \quad (33)$$

which is known to have a unique solution (cf., e.g., [6]). Hence, $w = w_{z,d}$, and the unique continuation principle for harmonic functions implies that $w = w_{z,d}$ in the exterior of

$D \cup \{z\}$. However, this implies that $z \in D$, for otherwise the singularity of $w = w_{z,d}$ at z would prohibit w to be harmonic in $\mathbb{R}^2 \setminus \bar{D}$. In the second case, where z is outside the unit disk, we can make use of the remark at the beginning of this proof, which states that $g_{z^*,d'}$ also belongs to $\mathcal{R}(L)$. Since z^* belongs to the unit disk, the previous argument shows that $z^* \in D$, or equivalently, $z \in D^*$, in this case. This completes the proof. \square

By virtue of (27) we can now apply this result to check whether some point z belongs to $D \cup D^*$ by means of the following test:

$$z \in D \cup D^* \quad \text{iff } g_{z,d} \in \mathcal{R}(|M - M_0|^{1/2}). \quad (34)$$

Note that the particular choice of the dipole moment d is irrelevant for this statement.

We remark that in all applications for which the factorization method has been investigated so far (cf., e.g., the examples in [8, 10, 11]) it was always possible to completely characterize the inclusion set D . Here, there is no way to distinguish between D and D^* . Of course, this handicap can be overcome in practice by moving the device and taking an additional set of measurements.

To implement the factorization method, that is, to test (34) numerically, we can proceed in much the same way as described in [8, 12]. According to the so-called Picard criterion, a function $g_{z,d}$ belongs to the range of $|A|^{1/2}$ for some injective compact and selfadjoint operator A (here, $A = M - M_0$) if and only if the series

$$\sum_{n=1}^{\infty} \frac{\langle g_{z,d}, v_n \rangle_{\mathcal{L}^2(\Gamma)}^2}{|\lambda_n|} \quad (35)$$

converges. Here, $\{\lambda_n\}$ is the sequence of eigenvalues of A and v_n are the associated normalized eigenfunctions. Both can be approximated from the given data. Ordering the eigenvalues λ_n such that $|\lambda_n|$ is nonincreasing, the denominators as well as the numerators of the fractions in (35) tend to exhibit a geometric decay. This allows us, for each point $z \in \mathbb{R}^2$ and

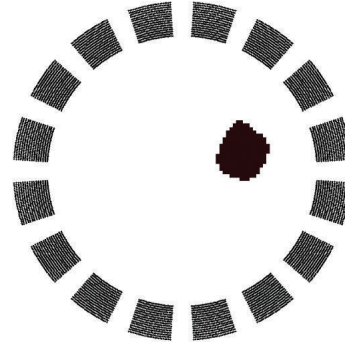


FIGURE 4: A first reconstruction.

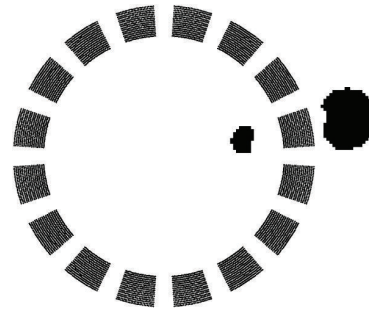
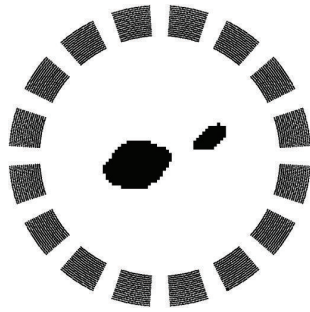


FIGURE 5: Reconstruction of two objects (left) and a “ghost” (right).

each dipole moment $d \in \mathbb{R}^2$ with $|d| = 1$, to fit two scalar parameters $C_{z,d}$ and $q_{z,d}$ to achieve

$$\frac{\langle g_{z,d}, v_n \rangle_{\mathcal{L}^2(\Gamma)}^2}{|\lambda_n|} \approx C_{z,d} q_{z,d}^n, \quad n = 1, 2, 3, \dots, \quad (36)$$

to a reasonable degree of approximation. Therefore, we can base our numerical implementation of (34) on the following test:

$$z \in D \cup D^* \quad \text{iff } q_{z,d} < 1. \quad (37)$$

We refer to [8, 12] for further illustrations and justifications of this test.

Now we turn to some numerical results that have been obtained in [9] this way. In all these computations, test points z were aligned on a two-dimensional square grid with a grid size of 1 mm. If not mentioned otherwise, the grid consists of 101×101 test points, just covering the circle Γ and its interior.

The first example in Figure 4 corresponds to the same measured difference data that we have used for the other algorithm (cf., Figure 3). The black and white plot on the right shows the 16 electrodes together with our reconstruction of the metal object. Figure 5 on the left shows a likewise reconstruction of two objects of sizes 12×13 and 20×22 mm, respectively. Again, the positions of the reconstructed objects match very well with their true locations, however, their shapes are slightly deteriorated.

Finally, the right-hand side of the same Figure 5 contains the reconstruction of only one object whose position (rather, its projection onto the measurement surface) was *exterior* to the device, that is, the circle Γ . Therefore, the grid is somewhat bigger for this example. The true object is found very well, however, the reconstruction also illustrates Theorem 1 because a “ghost,” that is, the reflected object D^* in the interior of Γ , has also been detected.

5. CONCLUSIONS AND OUTLOOK

In this note, we have presented numerical results for two impedance imaging techniques for a newly built planar EIT device designed primarily for medical applications, where only one side of a patient is accessible for taking measurements.

For our numerical experiments, the sensing head of our device has been attached to a large tank filled with conducting liquid. The arrangement allows a good approximation by an infinite plane. One or two metal objects of different sizes were placed inside the liquid.

We have compared two algorithms for the solution of the inverse problem. The first method is based on a certain kind of linearization, and can be used to reconstruct quantitative information about the conductivity distribution. The numerical results show that this approach is suitable for identifying larger anomalies within the body. For the detection of

such anomalies, however, the factorization method is a more appropriate tool, as it is primarily designed for this purpose. In fact, the positions and the sizes of the objects were successfully reconstructed with the factorization method. On the other hand, this method gives no quantitative details about the conductivities. Still, such restricted information is adequate for many medical applications.

In the future, we plan to extend our methods to a fully three-dimensional model of the problem in order to obtain additional information about the depths of the anomalies. The theoretical basis for this has already been laid by Schappell in [13, 14]. Also, the application of our methods to clinical data and the treatment of interrelated side effects like contact impedances at the electrodes is a natural next step on our agenda. We will also exploit the possibility of combining the two reconstruction algorithms in a comprehensive approach.

ACKNOWLEDGMENTS

The authors thank K.-H. Georgi for building the tomograph and for many helpful discussions. The comments of the referees have also been appreciated, as they helped to improve the presentation. Finally, the authors like to thank A. Almasy for her help in generating the figures.

REFERENCES

- [1] D. S. Holder, Ed., *Electrical Impedance Tomography*, Institute of Physics, Bristol, UK, 2005.
- [2] J. L. Mueller, D. Isaacson, and J. C. Newell, "A reconstruction algorithm for electrical impedance tomography data collected on rectangular electrode arrays," *IEEE Transactions on Biomedical Engineering*, vol. 46, no. 11, pp. 1379–1386, 1999.
- [3] V. A. Cherepenin, A. Y. Karpov, A. V. Korjnevsky, et al., "Three-dimensional EIT imaging of breast tissues: system design and clinical testing," *IEEE Transactions on Medical Imaging*, vol. 21, no. 6, pp. 662–667, 2002.
- [4] Y. Zou and Z. Guo, "A review of electrical impedance techniques for breast cancer detection," *Medical Engineering and Physics*, vol. 25, no. 2, pp. 79–90, 2003.
- [5] J. C. Newell, D. G. Gisser, and D. Isaacson, "An electric current tomography," *IEEE Transactions on Biomedical Engineering*, vol. 35, no. 10, pp. 828–833, 1988.
- [6] R. Kress, *Linear Integral Equations*, Springer, New York, NY, USA, 1999.
- [7] K. Paulson, W. Lionheart, and M. Pidcock, "POMPUS: an optimized EIT reconstruction algorithm," *Inverse Problems*, vol. 11, no. 2, pp. 425–437, 1995.
- [8] M. Hanke and M. Brühl, "Recent progress in electrical impedance tomography," *Inverse Problems*, vol. 19, no. 6, pp. S65–S90, 2003.
- [9] C. Oesterlein, "Elektrische Impedanztomographie—Implementierung der Faktorisierungsmethode für ein konkretes Messgerät," Diploma thesis, Universität Mainz, Mainz, Germany, 2006.
- [10] B. Gebauer, "The factorization method for real elliptic problems," *Zeitschrift für Analysis und ihre Anwendung*, vol. 25, no. 1, pp. 81–102, 2006.
- [11] A. Kirsch, "The factorization method for a class of inverse elliptic problems," *Mathematische Nachrichten*, vol. 278, no. 3, pp. 258–277, 2005.
- [12] M. Brühl and M. Hanke, "Numerical implementation of two noniterative methods for locating inclusions by impedance tomography," *Inverse Problems*, vol. 16, no. 4, pp. 1029–1042, 2000.
- [13] M. Hanke and B. Schappel, "The factorization method for electrical impedance tomography in the half space," submitted in *SIAM Journal on Applied Mathematics*.
- [14] B. Schappel, "Die Faktorisierungsmethode für die elektrische Impedanztomographie im Halbraum," Dissertation, Universität Mainz, Mainz, Germany, 2005, <http://nbn-resolving.de/urn/resolver.pl?urn=urn:nbn:de:hebis:77-7427>.

Research Article

Model-Based Reconstructive Elasticity Imaging Using Ultrasound

Salavat R. Aglyamov,^{1,2} Andrei R. Skovoroda,^{2,3} Hua Xie,³ Kang Kim,³ Jonathan M. Rubin,⁴ Matthew O'Donnell,³ Thomas W. Wakefield,⁵ Daniel Myers,⁵ and Stanislav Y. Emelianov¹

¹Department of Biomedical Engineering, University of Texas at Austin, Austin, TX 78712, USA

²Institute of Mathematical Problems of Biology, Russian Academy of Sciences, Pushchino, Moscow Region 142290, Russia

³Department of Biomedical Engineering, University of Michigan, Ann Arbor, MI 48109, USA

⁴Department of Radiology, University of Michigan, Ann Arbor, MI 48109, USA

⁵Department of Surgery, University of Michigan, Ann Arbor, MI 48109, USA

Received 28 September 2006; Revised 2 March 2007; Accepted 16 May 2007

Recommended by Tie Zhou

Elasticity imaging is a reconstructive imaging technique where tissue motion in response to mechanical excitation is measured using modern imaging systems, and the estimated displacements are then used to reconstruct the spatial distribution of Young's modulus. Here we present an ultrasound elasticity imaging method that utilizes the model-based technique for Young's modulus reconstruction. Based on the geometry of the imaged object, only one axial component of the strain tensor is used. The numerical implementation of the method is highly efficient because the reconstruction is based on an analytic solution of the forward elastic problem. The model-based approach is illustrated using two potential clinical applications: differentiation of liver hemangioma and staging of deep venous thrombosis. Overall, these studies demonstrate that model-based reconstructive elasticity imaging can be used in applications where the geometry of the object and the surrounding tissue is somewhat known and certain assumptions about the pathology can be made.

Copyright © 2007 Salavat R. Aglyamov et al. This is an open access article distributed under the Creative Commons Attribution License, which permits unrestricted use, distribution, and reproduction in any medium, provided the original work is properly cited.

1. INTRODUCTION

Elasticity imaging or elastography is a method to remotely estimate elastic properties of biological tissues [1–4]. One of the approaches in elasticity imaging is based on the measurement of local tissue deformation as tissue responds to external or internal quasi-static mechanic loading. Ultrasound, MRI, or other methods can be used to measure the resultant internal tissue motion. Using inverse problem formulations, the elasticity (Young's modulus) distribution is evaluated based on the distribution of the strain tensor components. Initially, elasticity imaging was focused on the non-invasive cancer diagnosis, but then the approach proved to be useful in various other applications including detection of atherosclerotic plaques [5, 6], corneal refractive surgery [7], cardiac strain imaging [8], muscle biomechanics [9], and so forth.

Once the internal tissue motion is measured, the strain image in the tissue can be produced. Usually hard tissue re-

gions are less deformed in comparison with soft regions and, therefore, contrast in strain images is influenced by the tissue elasticity. However, the strain field depends not only on the elastic distribution, but also on global boundary conditions which can be very complicated in real tissues. As a result, the relationship between strain image and elasticity distribution in tissue is not straightforward and reconstruction of Young's modulus is required to determine tissue elasticity quantitatively. Elastic modulus reconstruction in an inhomogeneous material using remote measurements of internal displacements can be posed in a number of ways [10–18]. These approaches can be generally grouped into two categories: direct and indirect (model-based) reconstruction techniques. If all necessary components of the internal displacement vector and strain tensor are available at any point within the object, then reconstruction algorithms based on the mechanical equilibrium equations can be used to describe the unknown distribution of Young's or shear modulus—these techniques, therefore, belong to direct reconstruction

methods. Unfortunately, in direct reconstruction methods, it is often difficult to formulate and solve the inverse problem for an arbitrary geometry and elasticity distribution. However, if any prior knowledge or assumptions about the geometry of the object and boundary conditions can be made, the inverse problem can be solved by using repeated solutions of forward problems with adjusted elasticity parameters. Indeed, if elasticity variations of the object within the region of interest can be modeled based on the object geometry or any other assumptions, then a model-based reconstruction can be performed. Therefore, the model-based elasticity imaging methods could be useful in applications where the existence of the pathology is already determined from the imaging study and pathology characterization rather than detection is required. In such cases, the approximate location and geometry of the pathology is known and certain assumption about tissue elasticity distribution can be made. Note here, that both direct and model-based approaches provide information only about relative elasticity distribution. For absolute Young's modulus reconstruction, either reference point or measurements of stress are required.

Ultrasound is widely used in elasticity imaging since motion of the speckle can be tracked over large range of tissue deformations. However, the accuracy of the lateral displacement estimates is less accurate than axial component of the displacement vector. Indeed, for an ultrasound system, the resolution of axial displacement is limited primarily by the frequency bandwidth of the transducer, and the lateral resolution is determined by the width of the ultrasound beam [19, 20]. Since all displacement components and spatial derivatives are needed in direct reconstruction methods, the anisotropy in the accuracy of the displacement vector measurements is an additional source of noise in elasticity images. In contrast, model-based approaches can be formulated using only axial component of the displacement vector to insure that the quality of Young's modulus reconstruction is independent from the quality of lateral motion tracking.

Here we present the model-based elasticity imaging approach illustrated using two potential clinical applications: characterization of liver hemangiomas and differentiation of deep venous thrombi (DVT). For liver hemangioma, the spherical symmetry of the lesion was assumed, and for DVT a blood clot was described as a cylindrically symmetry object. In both cases, the external surface deformations were applied during continuous ultrasound imaging, and the measurements of tissue motion were performed using block-matching cross-correlation technique. Based on the measured strain images, the Young's modulus was reconstructed. These studies demonstrate that model-based reconstructive elasticity imaging can be used in applications where the geometry of the object and the surrounding tissue is assessable and certain assumptions about the pathology can be made from the ultrasound images.

2. THEORY

The model-based elasticity reconstruction technique is performed in two successive steps. First, the analytical solution

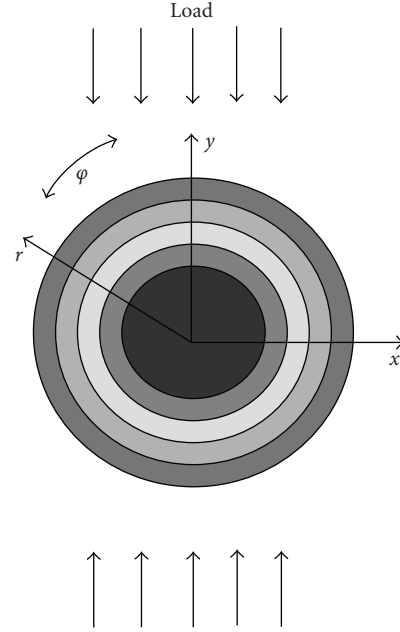


FIGURE 1: Schematic representation of the deformation model. (x, y) refer to Cartesian system of coordinates and (r, ϕ) refer to either cylindrical or spherical system of coordinates. The inhomogeneity is approximated as a layered round object, where the Young's or shear modulus is a function of only the radial coordinate r .

of the forward elastic problem is derived where the displacement and strain fields are determined based on the spatial distribution of Young's modulus in the object and pattern of externally applied deformation. Second, the inverse problem is solved iteratively, where the solution of the forward problem for a modeled object is compared with experimentally measured strains to match the unknown spatial distribution of Young's modulus in a region of interest (ROI). The Young's modulus distribution providing the best agreement is assumed to describe the distribution of elastic properties in the region of interest.

2.1. Forward problem

The formulation of a forward problem is based on a uniaxial deformation of an infinite, incompressible medium with spherical or cylindrically shaped inhomogeneities. Here, we consider only incompressible media since most soft tissues are very close to incompressible materials [21]. The forward problem is formulated in a spherical system of coordinates (r, ϕ, θ) for spherical inclusions and in cylindrical coordinates (r, ϕ, z) for cylindrical inclusions. The origins of the coordinate systems are placed at the centers of the inhomogeneities. The polar axis of both systems of coordinates is along an applied deformation, that is, an angle ϕ is between a radius vector and the deformation direction (see Figure 1). It is assumed that Young's modulus $E(r)$ is a function of only radial position. To find the solution of forward problem for arbitrary Young's modulus $E(r)$ over an ROI, we presume

that the Young's modulus is constant within each subinterval $[r_i, r_{i+1}]$, that is, $E(r) : E_i = \text{const}$, $r \in [r_i, r_{i+1}]$, $i = 1 \dots N$, where N is the total number of subintervals covering the region of interest [22]. The displacement vector \vec{U} must satisfy the equations of static equilibrium for isotropic incompressible linear medium on each subinterval $[r_i, r_{i+1}]$ [23]:

$$\mu \nabla^2 \vec{U} + \nabla p = 0, \quad (1)$$

where p is static internal pressure and μ is shear elastic modulus. For incompressible media, the shear modulus and Young's modulus are related ($\mu = E/3$), and only one modulus (μ or E) is sufficient to describe the elastic properties of the material. In addition, the incompressibility condition must be satisfied: $\text{div } \vec{U} = 0$.

Based on Goodier's solution [24, 25], we attempt to find the solution of (1) under the assumption of spherical symmetry (3D case) in the form

$$\begin{aligned} u_r &= \frac{1}{4} V_r(r) [1 + 3 \cos(2\varphi)], & u_\theta &= 0, \\ u_\varphi &= V_\varphi(r) \sin(2\varphi), \\ p &= P_0(r) + P_1(r) [1 + 3 \cos(2\varphi)], \end{aligned} \quad (2)$$

where the displacement vector components are $\vec{U} = (u_r, u_\varphi, u_\theta)$.

Similarly, solution of (1) under the assumption of cylindrical symmetry (2D case) can be found in the following form:

$$\begin{aligned} u_r &= V_r(r) \cos(2\varphi), & u_\varphi &= V_\varphi(r) \sin(2\varphi), & u_z &= 0, \\ p &= P_0(r) + P_1(r) \cos(2\varphi), \end{aligned} \quad (3)$$

where the components of the displacement vector are $\vec{U} = (u_r, u_\varphi, u_z)$.

Using the incompressibility condition, the relationships between the $V_r(r)$ and $V_\varphi(r)$ are

$$\begin{aligned} V_\varphi &= -\frac{1}{4} \left(2V_r + r \frac{\partial V_r}{\partial r} \right), & \text{for 3D,} \\ V_\varphi &= -\frac{1}{2} \left(V_r + r \frac{\partial V_r}{\partial r} \right), & \text{for 2D.} \end{aligned} \quad (4)$$

Substituting expressions (2)–(4) into (1) and eliminating the pressure, we find $V_r(r)$:

$$\begin{aligned} V_r &= c_1^i r + c_2^i r^3 + c_3^i r^{-2} + c_4^i r^{-4}, & \text{for 3D,} \\ V_r &= c_1^i r + c_2^i r^3 + c_3^i r^{-1} + c_4^i r^{-3}, & \text{for 2D.} \end{aligned} \quad (5)$$

Arbitrary constants $c_1^i, c_2^i, c_3^i, c_4^i$ vary for each $[r_i, r_{i+1}]$ layer. These unknown constants can be found using boundary conditions and the stress and displacement continuity conditions at the boundaries of each layer. To satisfy boundary conditions for (1), the displacements u_r and u_φ must be zero at $r = 0$ (the solution is limited at the center of the system of coordinates), and must match the strains applied at infinity. For uniaxial loading, the condition

$$\lim_{r \rightarrow \infty} \frac{V_r(r)}{r} = \varepsilon_0 \quad (6)$$

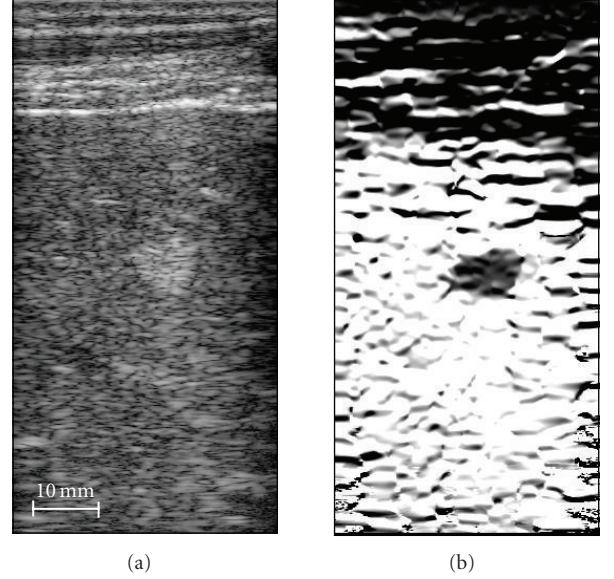


FIGURE 2: Liver hemangioma (a) B-Scan (left) and (b) strain image (right). The images are 38-mm by 78-mm.

must be satisfied, where ε_0 is axial strain at infinity. For homogeneous media, the solution of spherical and cylindrical problems (5) is the same linear function $V_r(r) = \varepsilon_0 \cdot r$.

Hence, the solution of (1) for a specific elasticity distribution can be reduced to the solution of a linear system of algebraic equations. This fact allows us to simplify and to speed up the solution of the forward problem and, as a result, to construct an effective procedure for inverse problem solution.

2.2. Inverse problem

The inverse problem was formulated using a Cartesian system of coordinates since a linear array ultrasound probe was used to measure the internal displacements and the ultrasound images were inherently obtained in a Cartesian system of coordinates (x, y, z) as evident from the ultrasound and strain images presented in Figure 2. Therefore, the analytical solutions of the forward problems formulated in spherical and cylindrical systems of coordinates were converted to a Cartesian system of coordinates. By pushing the ultrasound transducer against the skin, the external surface deformations we applied were such that the ultrasound beam is along the direction of applied deformation.

In ultrasound strain imaging, the quality of axial strain estimates (i.e., signal-to-noise ratio and resolution) is higher than that of other strain tensor components [19, 20]. Therefore, it is desired to construct the inverse problem solution using only one experimentally measured axial component of the strain tensor $\varepsilon_{yy} = \partial u_y / \partial y$, where u_y is the axial component of the displacement vector in Cartesian coordinates.

The theoretical distribution of axial strain in the region of interest can be computed when the following parameters are known: Young's moduli over a set of layers, the center of the

inhomogeneity (x_0, y_0) , and the effective deformation ε_0 at infinity. Using the analytic solution of the forward problem and having experimentally measured the axial strain component, the unknown Young's modulus E_i can be estimated by minimizing the error function, that is, the difference between experimentally measured and theoretically predicted axial strains [22]:

$$\delta = \|\varepsilon_{yy}^{\text{exp}} - \varepsilon_{yy}^{\text{theory}}(E_i, \varepsilon_0, x_0, y_0)\|. \quad (7)$$

In general, the deformation ε_0 and the center (x_0, y_0) of the object can be considered unknown and estimated simultaneously with the unknown distribution of the Young's modulus E_i by minimizing the error function. Alternatively, the applied deformation ε_0 and the center (x_0, y_0) of the object can be derived based on some a priori information.

Hence, elasticity reconstruction reduces to a minimization of the error function of (7) with respect to the unknown elasticity distribution, the geometry of the object, and the details of external loading.

To minimize (7), a gradient-based iterative procedure was implemented [22, 26]. The step size of the gradient method was chosen based on three estimates of error function δ . The minimum of the error function was locally predicted using a second-order polynomial approximation of δ as a function of the unknown parameters under the restriction of a decreasing error. Then, a global linear prediction for all unknowns was used simultaneously to increase the rate of convergence, that is, iterative step sizes for the gradient method were chosen taking into account the second-order polynomial approximation of δ as a function of unknown parameters. This iterative process does not require any additional derivatives of displacement or strain and, therefore, compared to direct elasticity reconstruction methods, does not introduce additional noise associated with higher-order derivatives of the displacement vector and strain tensor components. The high computational speed is achieved by using the analytical solution to calculate forward problem with only a small number of unknown parameters.

3. ELASTICITY RECONSTRUCTION OF LIVER HEMANGIOMA

Hemangioma is the most prevalent benign tumor of the liver, occurring in up to 70% of the population. Hemangiomas can vary in size and be as large as several centimeters. These tumors are filled with vascular channels of various sizes and may also contain fibrous tissue. Thrombi (clotted blood) may be present in the vascular channels. Histologically, the hemangioma is characterized by large, thin-walled blood vessels completely filled with blood [27].

These asymptomatic lesions are often found incidentally on ultrasound or CT when imaging studies are undertaken for other reasons. Once diagnosed, no treatment is necessary, and only large, symptomatic hemangiomas are treated by surgical resection. The diagnosis of hemangioma, however, requires special imaging studies such as nuclear medicine scans using radioactive technetium tagged red blood cells, magnetic resonance or dynamic CT scans with contrast.

Liver hemangiomas can be clearly identified in the ultrasound B-Scan image as a hyperechoic region, and the margins of the tumor are usually well defined. However, routine ultrasound is suggestive but usually not diagnostic. Many other tumors in liver, some of which are malignant, may appear similar on the BScan. Therefore, there is a need to specifically diagnose a detected liver mass in the least invasive and most time/cost efficient way available.

In the literature, hemangiomas are often referred to as soft lesions filled with blood [27]. Therefore, elasticity imaging may help in the diagnosis of hemangiomas. Indeed, most solid tumors are usually harder than the background, so hemangiomas may be distinguished from other liver tumors based on their mechanical properties.

To test the hypothesis that elasticity imaging can detect and diagnose hemangiomas, studies on volunteers with previously diagnosed hemangioma were performed. All subjects gave informed consent, and this study was approved by the University of Michigan Institutional Review Board. In these experiments, the liver was imaged between the ribs using an Ultramark-9 ATL scanner with a linear 128-element array transducer operating at 5 MHz. The system was interfaced with a custom-made circuit board to acquire approximately 120 frames of real-time digital RF signals during 4 seconds. Within this interval, the array, attached to a deformational device residing on a clinical trolley (gurney), was pressed against the body to produce a modest deformation of the liver. In most experiments, surface deformations did not exceed 10–12 mm, and all volunteers indicated no discomfort from the applied stress.

In all experiments, frame-to-frame motion was estimated using a two-dimensional correlation-based phase-sensitive speckle tracking technique [28]. The 2D displacement was estimated from the position of the maximum correlation coefficient, where the axial displacement estimate was refined using the position of the phase zero crossing of the analytic signal correlation. Displacement error was further reduced by filtering spatially adjacent correlation functions prior to displacement estimation [28].

The ultrasound B-Scan image of a liver hemangioma is presented in Figure 2(a). This image is a typical example of hemangiomas, where the location, margins, and size of the tumor are clearly identified. Furthermore, the muscle layers can be easily recognized at the top. This and other images in Figure 2 are 38-mm by 78-mm, where the transducer is located at the top of the image.

The distribution of the normal axial strain (ε_{yy}) is shown in Figure 2(b). This quantitative grayscale image is displayed from 0 to 10 percent strain, where full black corresponds to no strain and full white to 10% strain. The tumor is clearly visible as a low strain region indicating that overall it is harder than the background tissue.

Similar results were obtained from several other volunteers. The apparent overall hardness of a hemangioma, inferred from the strain image, is unexpected given the soft interior of the tumor. However, this result is consistent with information gathered by surgeons in the operating room—when large, symptomatic hemangiomas are treated

by surgical resection, the intact hemangiomas are felt as hard lesions. Pressure applied to the hemangioma, however, ruptures it, releasing blood as it collapses. Therefore, a hemangioma feels hard even it is filled with blood, which has no or low-shear elasticity.

In general, a soft, fluid-filled sack can appear hard if it is encapsulated by a very hard, thin membrane. If the mechanical properties of the shell are similar to that of the lesion, the shell itself would not affect the strain pattern. If the shell is harder than the lesion, however, the strain magnitude inside of the lesion is reduced. In fact, for an infinitely hard and absolutely noncompliant shell, the strain inside of the lesion vanishes regardless of the internal material properties. Therefore, it is reasonable to assume that the thin membrane encapsulating a hemangioma is significantly harder than the lesion's core, and dominates the overall strain pattern within the tumor. The mechanical properties of the shell surrounding a lesion can significantly impact the strain distribution. In particular, the strain images of a heterogeneous lesion surrounded by a hard shell and a uniform hard inclusion appear very similar. It may be possible, however, to estimate the lesion composition in both cases using reconstructive elasticity imaging.

For elasticity imaging of hemangiomas, the mapping of Young's modulus was performed using two approaches: direct reconstruction and model-based reconstruction. Direct reconstruction numerically solves the discretized equilibrium equations for a plane strain condition [10]. The plane strain condition is a reasonable approximation for elasticity imaging of the liver, where deformations are applied through the rib cage resulting in negligible out-of-plane strains. This method does not require any a priori knowledge of the object, and no other assumptions are made. After defining a region of interest containing the lesion, the Young's modulus distribution is reconstructed relative to the modulus of the background tissue (i.e., liver).

In model-based approach we assume that the hemangioma can be modeled as a spherical object such that the elastic modulus within the imaging plane is simply a function of radial position from the center of the tumor. For a realistic tumor, this is a reasonable approximation if the tumor is near no external boundaries. Nevertheless, by assuming a simple model such as this, the model-based reconstruction in the vicinity of the tumor core is far less susceptible to strain noise compared to direct elasticity reconstruction.

The results of the elasticity reconstruction are presented in Figure 3. In Figure 3(a), a 17.5-mm by 17.5-mm region of interest (ROI) of grayscale ultrasound image containing the hemangioma is shown. In direct reconstruction method (see Figure 3(b)), the Young's modulus along the ROI boundary was set to unity, resulting in reconstruction of the Young's modulus relative to liver. Clearly, the overall hemangioma is harder than the background tissue, but it has a softer interior part. This distribution is better depicted in the model-based elasticity image (see Figure 3(c)), where the softer interior part can be easily identified. In model-based reconstruction, the hemangioma was initially modeled as a homogeneous spherical inclusion, that is, object with one layer

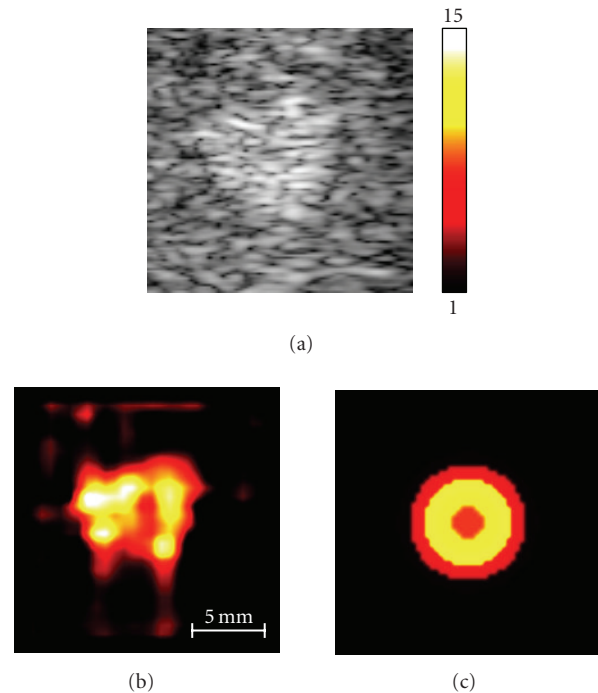


FIGURE 3: B-Scan (a) and elasticity images of hemangioma obtained direct method (b) and model-based method (c).

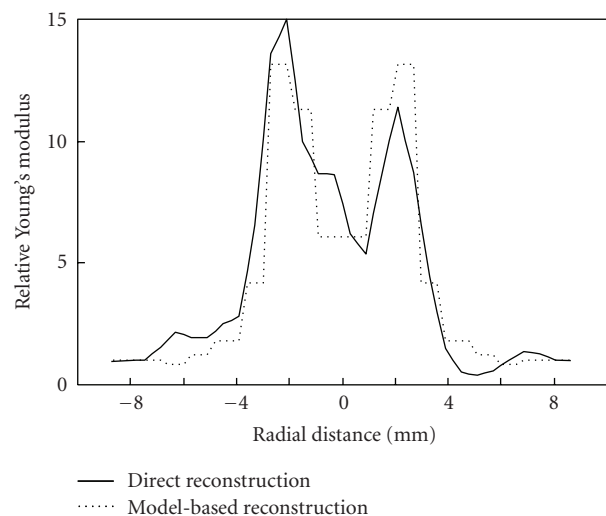


FIGURE 4: The Young's modulus distributions, obtained using direct and model-based reconstruction methods, are compared along the horizontal line intersecting the center of the hemangioma.

only. For a given number of layers, the relative Young's modulus, the external load ϵ_0 and position of hemangioma center (x_0, y_0) were reconstructed by minimizing the error function (7) across the ROI.

The Young's modulus distributions along the horizontal line intersecting the center of the hemangioma are contrasted in Figure 4 indicating reasonable agreement between the two

different reconstruction approaches. In model-based reconstruction approach, only 12 layers were used to describe hemangioma. The results in Figures 3 and 4 correspond closely to the expected elasticity distribution within the hemangioma, where the capsule surrounding the tumor makes the lesion harder overall. Reconstructive elasticity imaging captures the complex composition of such tumors.

The results of this study suggest that diagnosis of liver hemangioma may be possible with reconstructive elasticity imaging. Strain imaging by itself may not be sufficient to differentiate hemangioma from other types of liver tumors since all lesions overall can produce somewhat similar strain images. In contrast, the reconstructed elasticity map may capture the critical differences between the tumors.

4. ELASTICITY RECONSTRUCTION OF DEEP VEIN THROMBOSIS

The leading cause of preventable in-hospital mortality in the USA and other developed countries is pulmonary embolism (PE), which is one of the complications of deep venous thrombosis [29]. DVT occurs when the blood clot forms inside a deep vein (commonly located in the calf or thigh) and either partially or completely blocks the flow of blood in the vein. In pulmonary embolism, a portion of the thrombus detaches from the vessel wall and travels through the veins into the lung. When large emboli lodge in the main pulmonary artery, pulmonary embolism can quickly become fatal. The level of pulmonary embolism risk and DVT treatment depend on the age of the clot (in this paper, we often refer to DVT as blood clot). For an acute thrombus, the patient is at a higher risk of the clot breaking off and becoming an embolus. This patient is treated with heparin followed by oral anticoagulants. Patients with chronic DVT are treated with either oral anticoagulants, coumadin, alone, or no treatment [30]. Because the risk of bleeding is higher with heparin than with coumadin, one would like to avoid the use of heparin if at all possible [31]. Therefore it is clinically important to distinguish between acute and chronic DVT.

Both magnetic resonance imaging (MRI) and duplex ultrasound can tell whether a thrombus is present [32, 33]. The problem is that while these technologies can identify the blood clot in the vein, they cannot determine its age. Studies suggest that elastic properties of clot can be used to determine DVT maturity [22, 34–41]. This is based on the assumption that the Young's modulus of a thrombus changes monotonically with fibrin and collagen concentration. Since both the fibrin and collagen content of a thrombus increase over time, DVT hardens with age. Consequently, remote estimation of the elastic properties of a thrombus can become an important clinical tool to age DVT.

The examination employs real-time B-mode sonography (2D grayscale ultrasound imaging) combined with color flow Doppler imaging and compression ultrasound. During the compression ultrasound, a transverse view of the veins and arteries of the patient's leg is imaged. The operator periodically pushes on the surface of the leg to deform the underlying tissue including vein and artery. If the vein does not

deform while the adjacent artery does, the clot is suspected [33]. Since compression ultrasound already has all of the essential ingredients of elasticity imaging (i.e., external deformation of the object during continuous ultrasound imaging), elasticity imaging is a simple addition to the existing procedure of DVT diagnosis [36].

Animal studies were performed using a rat model of stasis-induced-venous thrombosis [37, 38, 42, 43]. The protocol was approved by the University of Michigan Committee on the use and care of animals and strictly complied with the National Institutes of Health Guide for the care and use of laboratory animals. A group of five rats were used in this study although only four animals developed thrombi. On the first day, all rats underwent surgery to initiate thrombus formation in the inferior vena cava (IVC). As the animals developed thrombi, which changed progressively from acute to chronic stages [42], each rat was imaged on days 3, 4, 5, 6, 7, 8, and 10.

All experiments were performed using a Siemens "Elegra" ultrasound scanner with a linear 12 MHz array transducer (VFX13-5). First, the IVCs were scanned in transverse and longitudinal orientations using color Doppler mode to determine thrombus location and find the best possible probe position on the rat's abdomen. Next, the transducer itself was used to compress the rat's abdominal wall and underlying tissue in a transverse orientation. It was attached to a manual deformation device to achieve continuous compression. The deformation lasted approximately 6 seconds, while phase sensitive ultrasound frames were collected in real time. Consecutive frames were processed offline using a 2D correlation-based phase-sensitive speckle tracking algorithm to derive the strain image of the DVT and surrounding tissue [28]. A kernel size 0.60-mm laterally by 0.17-mm axially was chosen for cross-correlation. The correlation function was filtered by a Hanning filter extending 1.20-mm laterally by 0.85-mm axially. Finally, frame-to-frame displacements were accumulated over a number of frames within the same deformation sequence and axial strains were calculated numerically.

An analysis of the B-scan in the thrombus area (see Figure 5) was the starting point of elasticity reconstruction for each animal. Based on the ultrasound image, the ROIs for elasticity reconstruction and the position of the clot center (x_0, y_0) were chosen. Each ROI was selected such that it included the IVC and a small portion of surrounding tissue (see Figure 6) to minimize elasticity variations of background tissue. The elasticity reconstruction program creates relative Young's modulus images—the stress distribution at the surface in response to surface-applied deformations is required for absolute reconstruction. Therefore, a vessel wall was used as the reference material, that is, Young's modulus of the vessel wall was assigned unity value.

A slight modification of described method was used for DVT elasticity reconstruction. We assume that the external load is applied at an angle α relative to the axial direction of an ultrasound beam. The angle α was added to expression (7) as a parameter of minimization. The details are presented elsewhere [22]. Based on the geometry of the thrombus,

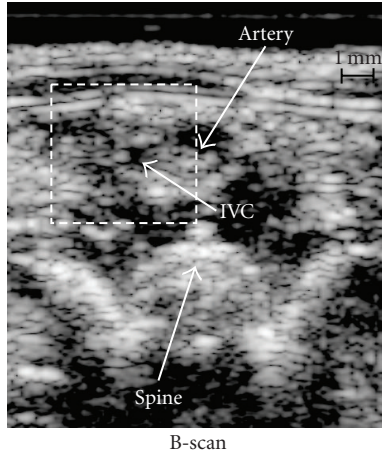


FIGURE 5: Ultrasound B-scan image of rat's abdomen.

vessel, and surrounding tissue (Figure 1), the clot-containing vessel is modeled as a long round cylinder. At the beginning of the reconstruction, a homogeneous cylindrical clot was assumed. The position of the clot center (x_0, y_0) was manually set based on the ultrasound image.

Once the solution for a given number of rings was found, the number of rings required to represent the object was increased. The previous elasticity distribution and load parameters α and ε_0 were used (after interpolation) as the initial point for the next step, where thrombus, vessel wall, and surrounding tissue were approximated using more independent rings of different elasticity. This iterative process was continued until the difference between two successive reconstructions (i.e., Young's modulus reconstructions for a different number of layers) was less than 2%. In the final Young's modulus map, the number of layers ranged from 30 to 40 depending on a particular dataset.

A typical B-scan image of a rat's abdomen with 5-day old thrombus is shown in Figure 5. This image covers 10-mm (axial) by 8.5-mm (lateral) region. Using color-flow imaging, the artery adjacent to the IVC was identified while no flow was detected in the IVC signaling that the thrombus occluded the vessel. On the bottom of the B-scan, the anterior surface of the spine can also be noted. Figure 6 presents the results of model-based elasticity reconstruction for the same rat. The 4.5-mm by 4.5-mm elasticity reconstruction region (Figure 6(a), also outlined rectangular area in Figure 5) was chosen to include the entire IVC, with the clot located in the center, and a small portion of background tissue. The measured axial strain image is presented in Figure 6(b). This image is displayed over a 0 to 18% strain dynamic range, where full white represents no strain, and full black represents a normal axial strain magnitude of 18% and larger (negative strain indicates that vein size was reduced vertically during the deformation).

Once the region of interest was identified, iterative elasticity reconstruction was performed, where the experimentally measured axial strain distribution $\varepsilon_{yy}^{\text{exp}}$ was compared with the theoretically predicted axial strain map $\varepsilon_{yy}^{\text{theory}}$ to

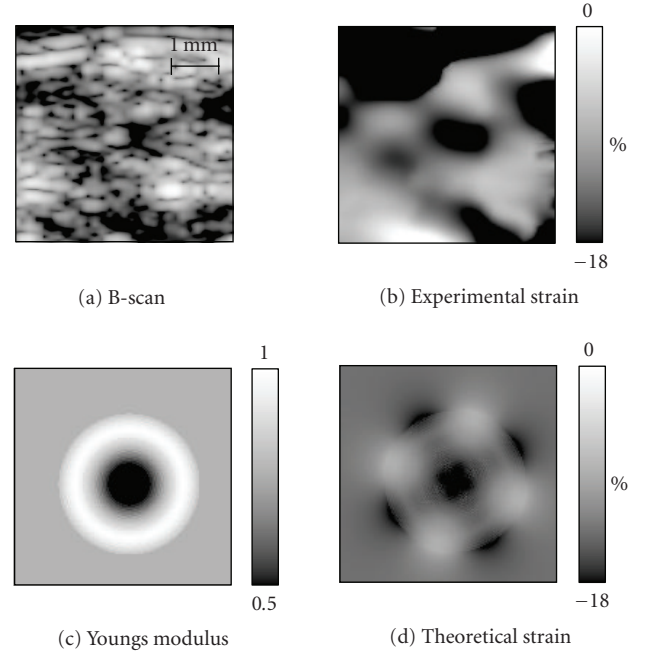


FIGURE 6: Elasticity reconstruction procedure demonstrated for a rat with a 5-day old thrombus. (a) A 4.5-mm by 4.5-mm region of interest (a) was selected for elasticity reconstruction. (b) The measured axial strain image within selected ROI. (c) Reconstructed Young's modulus distribution. (d) Corresponding theoretical axial strain image.

minimize the error function (7). The resultant Young's modulus distribution E_i over a set of rings is presented in Figure 6(c) where a grayscale map is used to display the relative Young's modulus over the 0.5 to 1.0 range. The grayscale map was selected so that full black corresponds to a relative Young's modulus of less than or equal to 0.5, and white areas represent harder tissue. Finally, Figure 6(d) presents the theoretically predicted axial strain distribution corresponding to reconstructed values of Young's modulus in Figure 6(c).

The minimization process is illustrated in Figures 7 and 8. Figure 7 shows changes in relative Young's modulus during iterations. In this example, the number of layers is fixed and equal to 5. The initial elasticity value was taken from the previous step, where the number of layers was equal to 4. During each iteration, the minimization of the error function (7) was performed. Regions of rapid change in elasticity (at iterations 5 and 25) correspond to successful global linear prediction resulting in 5–10 times faster convergence. Figure 8 presents behavior of relative elasticity of thrombus as the number of rings is increased. These results illustrate that 30–40 rings are sufficient to describe the blood clot, vessel wall, and surrounding tissue for this particular experimental dataset since further increase in the number of rings does not change the final result.

Figure 9 contrasts relative Young's modulus profiles along the center of the thrombus for one of the animals at 5, 8, and 10 days after the surgery (the profile for 5-day old thrombus corresponds to results presented in Figures 5–8). Figure 10

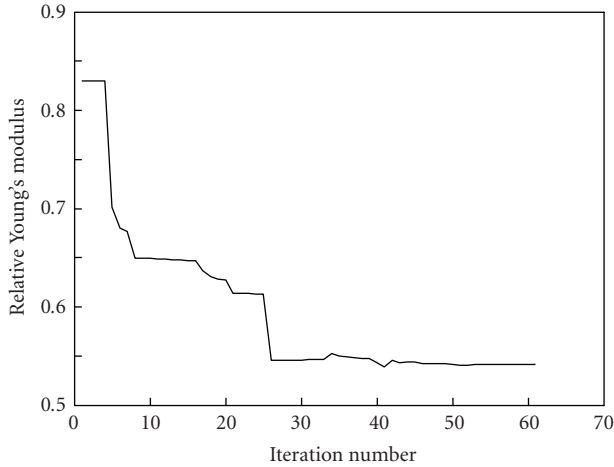


FIGURE 7: Relative Young's modulus versus number of iterations for blood clot approximated using 5 rings or layers. Initial value for iterative process was chosen from previous 4-ring model. These particular results correspond to the data presented in Figures 5 and 6 (an animal with 5-day old thrombus).

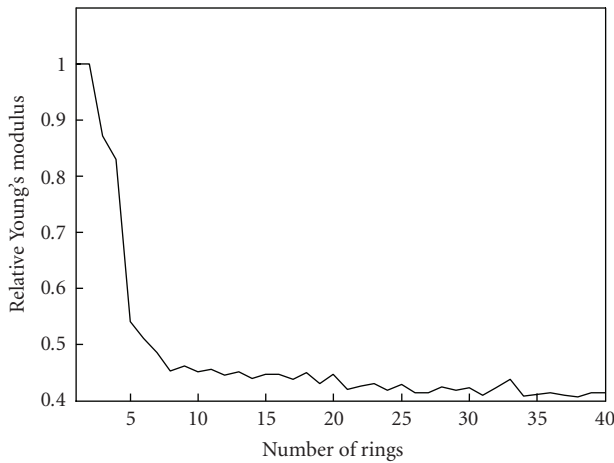


FIGURE 8: Changes in relative Young's modulus with increased number of layers or rings. These particular results correspond to the data presented in Figures 5 and 6 (an animal with 5-day old thrombus).

presents the profiles of relative Young's modulus for another animal with 4-day, 7-day, and 10-day old thrombus. Note here, that position of vessel walls have changed through time because of the vessel shrank in process of clot formation [37, 38].

In this animal model, 3-day to 4-day old thrombus represents an acute DVT, 6-day to 7-day old thrombus represents a subacute DVT, and 10-day old thrombus represents a chronic DVT. The rate of thrombus growth is different in humans, but the process of clot formation has the same stages. As the thrombus develops, its elasticity increases. This is further illustrated in Figure 11, where relative Young's modulus is plotted as function of time after surgery, that is, age of the thrombus. Here, the elasticity values were averaged for the

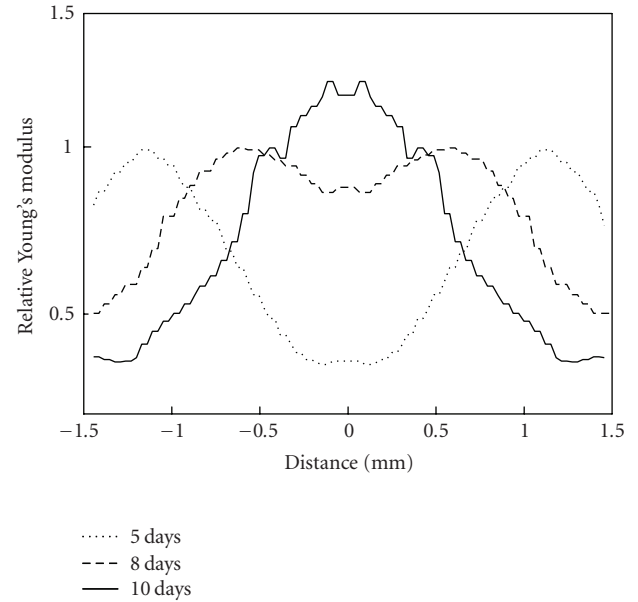


FIGURE 9: Young's modulus profiles for 5-day old (acute), 8-day old (subacute), and 10-day old (chronic) thrombi.

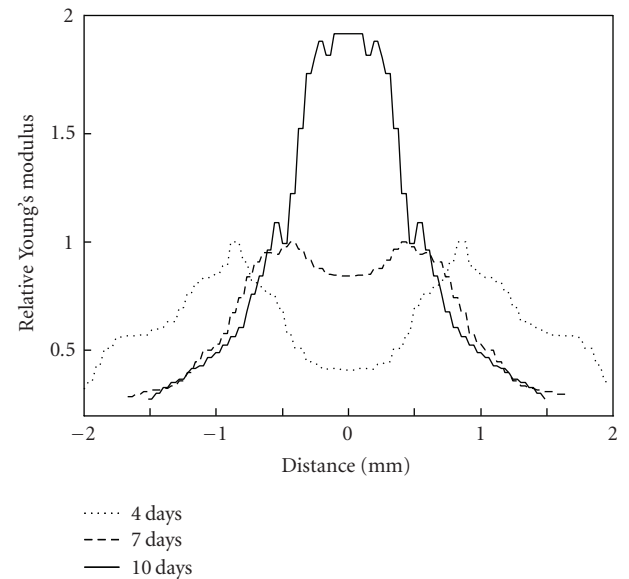


FIGURE 10: Young's modulus profiles for 4-day old (acute), 7-day old (subacute), and 10-day old (chronic) thrombi.

four rats used in our study. Clearly, the relative elasticity of the clot increases with thrombus age suggesting that Young's modulus can be used to age DVT.

The results of in vivo elasticity reconstruction were compared with the results of ex vivo direct elasticity measurements [38]. A total of 59 Sprague-Dawley rats were studied. On days 3, 6, 10, 12, and 14, the group of animals (9–13 animals) was euthanized for the direct measurements of Young's modulus of the blood clots. Thrombi were removed from the dissected IVC and transported immediately to the next room

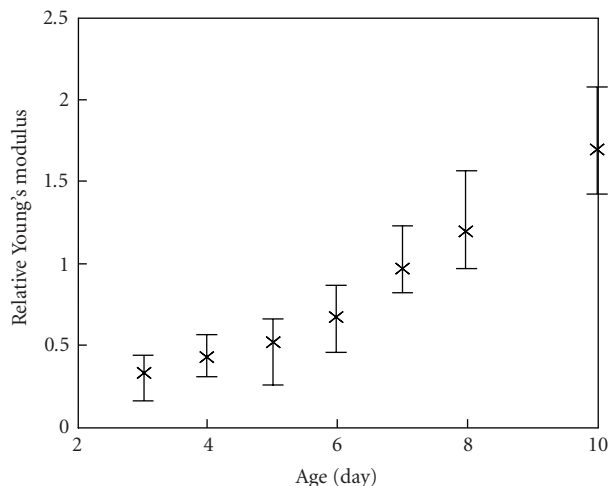


FIGURE 11: The model-based reconstructed values of relative Young's modulus of the blood clot during formation and aging of thrombus.

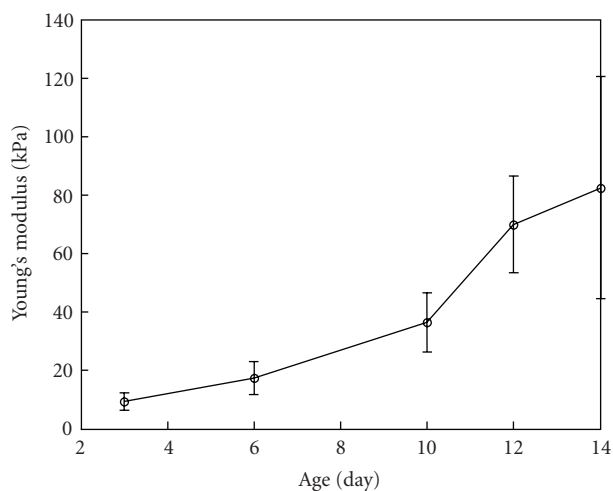


FIGURE 12: The ex vivo direct mechanical measurements of the Young's modulus of the blood clot during formation and aging of thrombus.

for mechanical load-displacement measurements to accurately assess the Young's modulus of the thrombi. Specifically, the displacement versus force was measured while a test sample was subjected to compression. Based on the strain-stress relationship and finite element modeling of the clot deformation, Young's modulus of the test sample was estimated. Initially, the system was tested on rubber cylindrical sample with known elastic properties [38]. The direct ex vivo elasticity measurements were performed using 15–20% strain range. This range approximately corresponds to the strain level used in ultrasound in vivo studies. In Figure 12, the mechanical, ex vivo measurements of Young's modulus are plotted as function of thrombus age.

Figures 11 and 12 demonstrate that the in vivo reconstruction agrees well with the ex vivo mechanical measure-

ment. The results of direct elasticity estimations and remote assessment of the clot elasticity indicate that a thrombus hardens as it matures. Indeed, the Young's modulus of thrombi increases over time, and a 10-day old thrombus is approximately 3–6 times harder than a 3-day old thrombus.

Therefore, the model-based elasticity reconstruction approach is applicable to an animal model of DVT. Indeed, thrombus elasticity (Young's modulus) increases with time and can be accurately assessed and monitored using quantitative model-based reconstructive elasticity imaging.

5. CONCLUSIONS

The model-based elasticity reconstruction method was developed to demonstrate the potential of ultrasound-based reconstructive elasticity imaging. The developed model-based method has several advantages compared to other elasticity reconstruction approaches. The model-based elasticity reconstruction requires only axial component of the strain tensor. The minimization procedure in model-based reconstruction is relatively efficient and stable given the small number of unknown scalar parameters derived from an analytic solution of the forward elastic problem. Finally, the model-based reconstruction is not highly sensitive to the details of external loading. The model-based reconstructive elasticity imaging was applied to differentiate liver hemangioma and to age deep vein thrombosis. The results of our studies indicate that the model-based reconstruction approach is applicable in ultrasound in vivo elasticity imaging and can provide needed information about biomechanical properties of tissues.

ACKNOWLEDGMENTS

This work was supported in part by National Institutes of Health under Grant HL68658 and U.S. Army Medical Research and Materiel Command under Grant DAMD17-02-1-0097.

REFERENCES

- [1] L. Gao, K. J. Parker, R. M. Lerner, and S. F. Levinson, "Imaging of the elastic properties of tissue—a review," *Ultrasound in Medicine and Biology*, vol. 22, no. 8, pp. 959–977, 1996.
- [2] J. Ophir, I. Cespedes, B. Garra, H. Ponnekanti, Y. Huang, and N. Maklad, "Elastography: ultrasonic imaging of tissue strain and elastic modulus in vivo," *European Journal of Ultrasound*, vol. 3, no. 1, pp. 49–70, 1996.
- [3] K. J. Parker, L. Gao, R. M. Lerner, and S. F. Levinson, "Techniques for elastic imaging: a review," *IEEE Engineering in Medicine and Biology Magazine*, vol. 15, no. 6, pp. 52–59, 1996.
- [4] J. Ophir, S. K. Alam, B. S. Garra, et al., "Elastography: imaging the elastic properties of soft tissues with ultrasound," *Journal of Medical Ultrasonics*, vol. 29, no. 4, pp. 155–171, 2002.
- [5] B. M. Shapo, J. R. Crowe, A. R. Skovoroda, M. J. Eberle, N. A. Cohn, and M. O'Donnell, "Displacement and strain imaging of coronary arteries with intraluminal ultrasound," *IEEE Transactions on Ultrasonics, Ferroelectrics, and Frequency Control*, vol. 43, no. 2, pp. 234–246, 1996.

- [6] C. L. de Korte, E. I. Cespedes, A. F. W. van der Steen, G. Pasterkamp, and N. Bom, "Intravascular ultrasound elastography: assessment and imaging of elastic properties of diseased arteries and vulnerable plaque," *European Journal of Ultrasound*, vol. 7, no. 3, pp. 219–224, 1998.
- [7] K. W. Hollman, S. Y. Emelianov, J. H. Neiss, et al., "Strain imaging of corneal tissue with an ultrasound elasticity microscope," *Cornea*, vol. 21, no. 1, pp. 68–73, 2002.
- [8] J. D'Hooge, A. Heimdal, F. Jamal, et al., "Regional strain and strain rate measurements by cardiac ultrasound: principles, implementation and limitations," *European Journal of Echocardiography*, vol. 1, no. 3, pp. 154–170, 2000.
- [9] S. F. Levinson, M. Shinagawa, and T. Sato, "Sonoelastic determination of human skeletal muscle elasticity," *Journal of Biomechanics*, vol. 28, no. 10, pp. 1145–1154, 1995.
- [10] A. R. Skovoroda, S. Y. Emelianov, and M. O'Donnell, "Tissue elasticity reconstruction based on ultrasonic displacement and strain images," *IEEE Transactions on Ultrasonics, Ferroelectrics, and Frequency Control*, vol. 42, no. 4, pp. 747–765, 1995.
- [11] C. Sumi, A. Suzuki, and K. Nakayama, "Estimation of shear modulus distribution in soft tissue from strain distribution," *IEEE Transactions on Biomedical Engineering*, vol. 42, no. 2, pp. 193–202, 1995.
- [12] F. Kallel and M. Bertrand, "Tissue elasticity reconstruction using linear perturbation method," *IEEE Transactions on Medical Imaging*, vol. 15, no. 3, pp. 299–313, 1996.
- [13] C. Sumi and K. Nakayama, "A robust numerical solution to reconstruct a globally relative shear modulus distribution from strain measurements," *IEEE Transactions on Medical Imaging*, vol. 17, no. 3, pp. 419–428, 1998.
- [14] D. B. Plewes, J. Bishop, A. Samani, and J. Sciarretta, "Visualization and quantification of breast cancer biomechanical properties with magnetic resonance elastography," *Physics in Medicine and Biology*, vol. 45, no. 6, pp. 1591–1610, 2000.
- [15] P. E. Barbone and J. C. Bamber, "Quantitative elasticity imaging: what can and cannot be inferred from strain images," *Physics in Medicine and Biology*, vol. 47, no. 12, pp. 2147–2164, 2002.
- [16] M. M. Doyley, S. Srinivasan, S. A. Pendergrass, Z. Wu, and J. Ophir, "Comparative evaluation of strain-based and model-based modulus elastography," *Ultrasound in Medicine and Biology*, vol. 31, no. 6, pp. 787–802, 2005.
- [17] Y. Zhang, L. O. Hall, D. B. Goldgof, and S. Sarkar, "A constrained genetic approach for computing material property of elastic objects," *IEEE Transactions on Evolutionary Computation*, vol. 10, no. 3, pp. 341–357, 2006.
- [18] M. M. Doyley, S. Srinivasan, E. Dimidenko, N. Soni, and J. Ophir, "Enhancing the performance of model-based elastography by incorporating additional *a priori* information in the modulus image reconstruction process," *Physics in Medicine and Biology*, vol. 51, no. 1, pp. 95–112, 2006.
- [19] M. A. Lubinski, S. Y. Emelianov, K. R. Raghavan, A. E. Yagle, A. R. Skovoroda, and M. O'Donnell, "Lateral displacement estimation using tissue incompressibility," *IEEE Transactions on Ultrasonics, Ferroelectrics, and Frequency Control*, vol. 43, no. 2, pp. 247–256, 1996.
- [20] X. Chen, M. J. Zohdy, S. Y. Emelianov, and M. O'Donnell, "Lateral speckle tracking using synthetic lateral phase," *IEEE Transactions on Ultrasonics, Ferroelectrics, and Frequency Control*, vol. 51, no. 5, pp. 540–550, 2004.
- [21] A. P. Sarvazyan, "Low-frequency acoustic characteristics of biological tissues," *Mechanics of Composite Materials*, vol. 11, no. 4, pp. 594–597, 1975.
- [22] S. R. Aglyamov, A. R. Skovoroda, J. M. Rubin, M. O'Donnell, and S. Y. Emelianov, "Model-based reconstructive elasticity imaging of deep venous thrombosis," *IEEE Transactions on Ultrasonics, Ferroelectrics, and Frequency Control*, vol. 51, no. 5, pp. 521–531, 2004.
- [23] S. Timoshenko and J. Goodier, *Theory of Elasticity*, McGraw-Hill, New York, NY, USA, 1951.
- [24] J. N. Goodier, "Concentration of stress around spherical and cylindrical inclusions and flaws," *Journal of Applied Mechanics*, vol. 55, no. 39, pp. 39–44, 1933.
- [25] A. R. Skovoroda, S. Y. Emelianov, M. A. Lubinski, A. P. Sarvazyan, and M. O'Donnell, "Theoretical analysis and verification of ultrasound displacement and strain imaging," *IEEE Transactions on Ultrasonics, Ferroelectrics, and Frequency Control*, vol. 41, no. 3, pp. 302–313, 1994.
- [26] A. R. Skovoroda, M. A. Lubinski, S. Y. Emelianov, and M. O'Donnell, "Reconstructive elasticity imaging for large deformations," *IEEE Transactions on Ultrasonics, Ferroelectrics, and Frequency Control*, vol. 46, no. 3, pp. 523–535, 1999.
- [27] R. S. Cotran, V. Kumar, and S. L. Robbins, *Robbins Pathologic Basis of Disease*, W.B. Saunders, Philadelphia, Pa, USA, 5th edition, 1994.
- [28] M. A. Lubinski, S. Y. Emelianov, and M. O'Donnell, "Speckle tracking methods for ultrasonic elasticity imaging using short-time correlation," *IEEE Transactions on Ultrasonics, Ferroelectrics, and Frequency Control*, vol. 46, no. 1, pp. 82–96, 1999.
- [29] J. Hirsh and J. Hoak, "Management of deep vein thrombosis and pulmonary embolism. A statement for healthcare professionals. Council on Thrombosis (in consultation with the Council on Cardiovascular Radiology). American Heart Association," *Circulation*, vol. 93, no. 12, pp. 2212–2245, 1996.
- [30] T. M. Hyers, G. Agnelli, R. D. Hull, et al., "Antithrombotic therapy for venous thromboembolic disease," *Chest*, vol. 114, no. 5 supplement, pp. 561S–578S, 1998.
- [31] R. D. Hull, G. E. Raskob, D. Rosenbloom, et al., "Heparin for 5 days as compared with 10 days in the initial treatment of proximal venous thrombosis," *The New England Journal of Medicine*, vol. 322, no. 18, pp. 1260–1264, 1990.
- [32] W. A. Erdman, H. T. Jayson, H. C. Redman, G. L. Miller, R. W. Parkey, and R. W. Peshock, "Deep venous thrombosis of extremities: role of MR imaging in the diagnosis," *Radiology*, vol. 174, no. 2, pp. 425–431, 1990.
- [33] B. D. Lewis, "The peripheral veins," in *Diagnostic Ultrasound*, C. M. Rumack, S. R. Wilson, and J. W. Charboneau, Eds., pp. 946–954, Mosby, St. Louis, Mo, USA, 2nd edition, 1998.
- [34] S. Y. Emelianov, J. M. Rubin, X. Chen, A. R. Skovoroda, T. W. Wakefield, and M. O'Donnell, "Ultrasound elasticity imaging of deep venous thrombosis," in *Proceedings of IEEE Ultrasonics Symposium*, vol. 2, pp. 1791–1794, San Juan, Puerto Rico, USA, October 2000.
- [35] J. M. Rubin, H. Xie, K. Kim, et al., "Sonographic elasticity imaging of acute and chronic deep venous thrombosis in humans," *Journal of Ultrasound in Medicine*, vol. 25, no. 9, pp. 1179–1186, 2006.
- [36] S. Y. Emelianov, X. Chen, M. O'Donnell, et al., "Triplex ultrasound: elasticity imaging to age deep venous thrombosis," *Ultrasound in Medicine and Biology*, vol. 28, no. 6, pp. 757–767, 2002.
- [37] H. Xie, K. Kim, S. R. Aglyamov, et al., "Staging deep venous thrombosis using ultrasound elasticity imaging: animal model," *Ultrasound in Medicine and Biology*, vol. 30, no. 10, pp. 1385–1396, 2004.

-
- [38] H. Xie, K. Kim, S. R. Aglyamov, et al., "Correspondence of ultrasound elasticity imaging to direct mechanical measurement in aging DVT in rats," *Ultrasound in Medicine and Biology*, vol. 31, no. 10, pp. 1351–1359, 2005.
- [39] J. M. Rubin, S. R. Aglyamov, T. W. Wakefield, M. O'Donnell, and S. Y. Emelianov, "Clinical application of sonographic elasticity imaging for aging of deep venous thrombosis: preliminary findings," *Journal of Ultrasound in Medicine*, vol. 22, no. 5, pp. 443–448, 2003.
- [40] S. Siebers, B. Geier, D. Muth-Werthmann, et al., "Staging of venous thrombosis using ultrasound elastography," in *Proceedings of IEEE Ultrasonics Symposium*, vol. 2, pp. 1891–1894, Honolulu, Hawaii, USA, October 2003.
- [41] B. Geier, L. Barbera, D. Muth-Werthmann, et al., "Ultrasound elastography for the age determination of venous thrombi. Evaluation in an animal model of venous thrombosis," *Thrombosis and Haemostasis*, vol. 93, no. 2, pp. 368–374, 2005.
- [42] T. W. Wakefield, R. M. Strieter, C. A. Wilke, et al., "Venous thrombosis-associated inflammation and attenuation with neutralizing antibodies to cytokines and adhesion molecules," *Arteriosclerosis, Thrombosis, and Vascular Biology*, vol. 15, no. 2, pp. 258–268, 1995.
- [43] D. Myers, S. K. Wroblewski, P. K. Henke, and T. W. Wakefield, "Coagulation biology," in *Surgical Research*, W. Souba and D. Wilmore, Eds., pp. 989–1000, Academic Press, San Diego, Calif, USA, 2001.